SEARCH FOR THE POPULATION OF THE ^{12}BE SECOND 0^+ STATE IN THE DECAY OF ^{13}BE

By

Xinyi Wang

A DISSERTATION

Submitted to
Michigan State University
in partial fulfillment of the requirements
for the degree of

Physics — Doctor of Philosophy

2025

ABSTRACT

The low-lying structure of the unbound nucleus ^{13}Be remains incompletely understood, particularly regarding whether neutron decays populate the isomeric second 0_2^+ state (2.25 MeV, $\tau = 331$ ns) in ^{12}Be. This thesis presents the first dedicated search for this decay path using invariant mass spectroscopy. Neutron-removal reactions from a 78 MeV/u ^{14}Be beam incident on a ^{9}Be target were measured in coincidence with delayed γ-rays. The ^{12}Be fragments were identified using a novel charged-particle telescope, while neutrons were detected with the MoNA-LISA array and γ-rays with the CAESAR array surrounding the telescope.

No evidence of population and decay of the ^{12}Be 0_2^+ state was observed in either the 2.1 MeV γ-ray or 511 keV positron annihilation signatures. An upper limit of 13% contribution was extracted. Simulations confirmed that the expected γ-ray yield from this decay channel would have been detectable given the measured p-wave resonance strength. Consequently, the previously observed p-wave resonance near 500 keV must decay directly to the ^{12}Be ground state, resolving a key uncertainty in the ^{13}Be level scheme. This result constrains theoretical models of shell evolution near the neutron drip line at $N = 8$.

I dedicate this work to my beloved wife, Zheng Li.

ACKNOWLEDGMENTS

I would like to thank my advisor Paul Gueye for his guidance on not only research but also how to deal with people. He has always been positive and supportive no matter what I did. His passion for science inspired me and many other people around him. Thanks to Michael Thoennessen for his kind and critical help on the data analysis and thesis writing. I also thank my thesis committee members Remco Zegers, Witold Nazarewicz, Kendall Mahn, Marcos Caballero, and Paul DeYoung for their advice and support.

It has been a great experience to work in the MoNA collaboration. Special thanks to Thomas Baumann, Paul DeYoung, Nathan Frank, and Anthony Kuchera for their continuous support on every aspect of the experiment; to Belen Monteagudo Godoy and Thomas Redpath for their great contribution on setting up the experiment and data analysis framework. Also thanks to fellow graduate students Andrew Wantz, Geogia Votta, and Nico Mendez for the valuable experience of discussion and hanging out together.

Special thanks to Alex Brown and Jeffery Tostevin for their theory input that helped me interpret the experimental results.

I also would like to thank my family and friends that supported me throughout my academic pursuit. Thanks to my parents for their unconditional respect and support in the decisions I made and their multiple visits from China to bring "home" to me. Thanks to my wife, Zheng Li, for making my life meaningful and full of surprises, transforming me from a sad boy to a happy man. Thanks to Tianxudong Tang, my best friend, for the great time we study, exercise, sing, dance, and play video games together, and witnessing each other's wedding. Thanks to Kang Yu, the first one I knew in Michigan, who picked me up at the Lansing airport and became a great friend of mine.

Last but not least, I would like to thank the friends I met on the internet through the video games I played. A list of names is shown in Table 1. Their company partly supported my mental health through the hardest times and made me understand that a human being, as well as a Pokemon, has unlimited possibilities, and the possibilities lie in trust and perseverance.

Table 1: Friends on the internet

ID	Title
老匠(Conkedurr/Old craftsman)	米法老公林克(Mipha's husband Link)
花花(Lurantis/Flower)	星尘传说(Stardust legend)
蛇皮好累好想退休(Snakeskin wants to retire)	早(Morning)
宁死不屈铁哑铃(Unyielding Beldum)	邪恶妖鸟(Togekiss)
Ele	雪雪(Snow)
死狼(Lobo Muerto)	受队专家(Expert of defensive team)
Muelsyse	小rara (Little Rara)
小孔不聋(Kong)	学习使我快乐(Studying makes me happy)
老水都了(Lateo/Water city)	水水(Water)
7TS5	75
椰子自闭中(Roku/Coconut)	集集复集集(Unite and Unite again)
湿湿黏黏兽耳娘(Wet sticky furry girl)	小逝妹妹(Little sister Shi)

TABLE OF CONTENTS

LIST OF TABLES

LIST OF FIGURES

Chapter 1. Introduction

1.1 The atomic nucleus

It is known from the 19^{th} century that the matter in the physical world is composed of atoms. The species of atoms are called elements and are arranged in the periodic table. Atoms were believed to be invariable until Antoine Henri Becquerel, Marie Curie and Pierre Curie did their pioneering research work on radioactivity in the late 1890s [4, 5, 6, 7, 8, 9, 10]. In 1911, Ernest Rutherford announced the discovery of the atomic nucleus, based on experiments conducted by his student Ernest Marsden [11]. About 20 years later, in 1932, James Chadwick reported the discovery of the neutron [12]. These groundbreaking findings, along with the development of quantum mechanics, the invention of the cyclotron [13] and the linear accelerator [14] in 1932, laid the foundation for a new scientific field dedicated to understanding the atomic nucleus.

The nucleus is made up of protons and neutrons, which are collectively referred to as nucleons. The species of a nucleus, called a nuclide, is identified by the number of protons and neutrons in it. There are more than 3000 known nuclear species. All of them are arranged in the chart of nuclides, shown in Figure 1.1. A nuclide is usually referred to as ${}^{A}_{Z}X_{N}$, where Z is the number of protons (or the atomic number), N is the number of neutrons, A is the mass number, which is the sum of Z and N, and X is the atomic symbol that also identifies the number of protons. Isotopes are nuclei with the same atomic number (Z) but different neutron numbers (N) and are represented as rows in the chart of nuclides. In contrast, isotones have the same neutron number (N) but different atomic numbers (Z), appearing as columns in the chart. Isobars are nuclei with the same mass number (A) and

are depicted along the diagonal from the top left to the bottom right in the chart of nuclides.

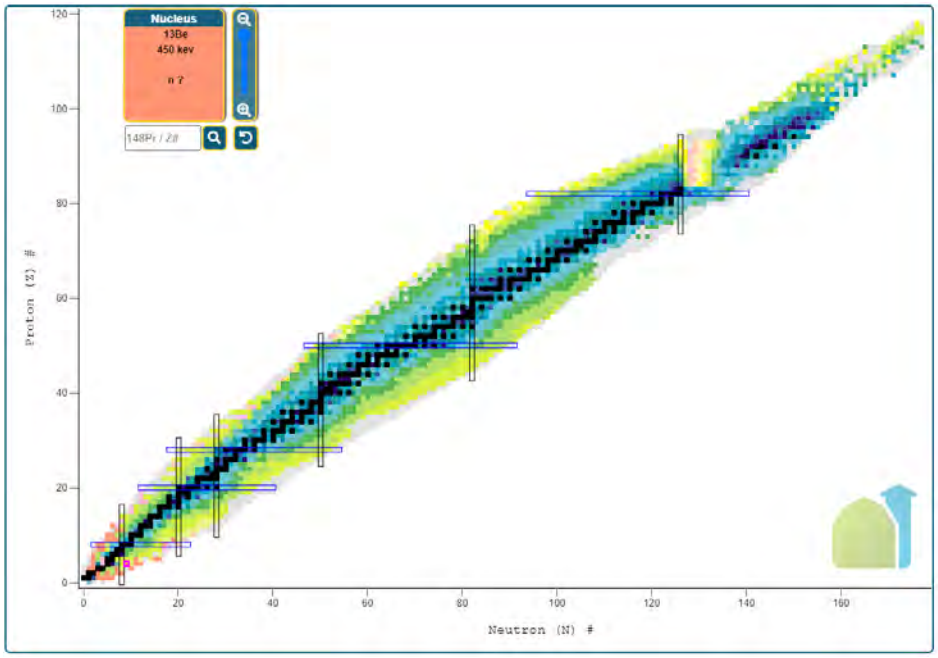

Figure 1.1: The nuclear chart reproduced from NNDC [1].

The colors in the chart represent the half-life of the nuclide. The black squares in the middle are stable isotopes, and the other are radioactive isotopes that will spontaneously decay by emitting various particles like electrons (β^-), positrons (β^+), helium particles (α), protons and neutrons; some of them can even capture their own electrons or undergo spontaneous fission. The half-lives of the nuclides range from longer than the age of the universe down to $\sim 10^{-22}$ s for particle-unbound nuclei [15].

The stability and decay mechanisms of a nucleus depend on the interactions among its nucleons. The strong force binds quarks together to form nucleons, and its residue binds protons and neutrons to form the nucleus. The weak nuclear force is related to β decay where a neutron (or proton) transforms into a proton (or neutron). The electromagnetic force also plays its part, since the proton has a positive charge. Gravity is totally negligible within nuclei, but becomes dominant in neutron stars, which are essentially extremely huge

nuclei [16].

The stability of a nucleus can be measured by its binding energy (BE), which is the energy required to break the nucleus into its proton and neutron constituents. If a nucleon is added to a nucleus and the binding energy increases, then a new nucleus is created. Oppositely, it takes the same energy to remove that nucleon. That amount of energy is called the proton separation energy (S_p) or neutron separation energy (S_n).

$$S_n(N, Z) = BE(N, Z) - BE(N - 1, Z) \tag{1.1}$$

$$S_p(N, Z) = BE(N, Z) - BE(N, Z - 1) \tag{1.2}$$

The boundary between positive and negative values of S is known as the drip line [17]. Nuclei within the drip lines are stable against the spontaneous emission of nucleons, whereas those outside the drip line can spontaneously decay by emitting one or more nucleons. The neutron drip line marks a distinct boundary: nuclei just inside the drip line undergo β^--decay with lifetimes on the order of milliseconds, whereas those outside the drip line have lifetimes around 10^{-20} seconds or less due to the strong interaction decay widths measured in MeV. For heavy nuclei, the Coulomb barrier significantly impedes proton decay, resulting in lifetimes for the one- or two-proton decay of nuclei just outside the proton drip line that can be comparable to or even longer than those for beta decay.

1.2 Nuclear structure theories

The study of nuclear structure is to understand the building blocks of atomic nuclei and how they combine and interact to make the variety of isotopes along with describing their

properties observed in experiments. At different spatial scales or energy levels, different degrees of freedom are dominant as shown in Figure 1.2, therefore, different theoretical models are used to explain this evolution.

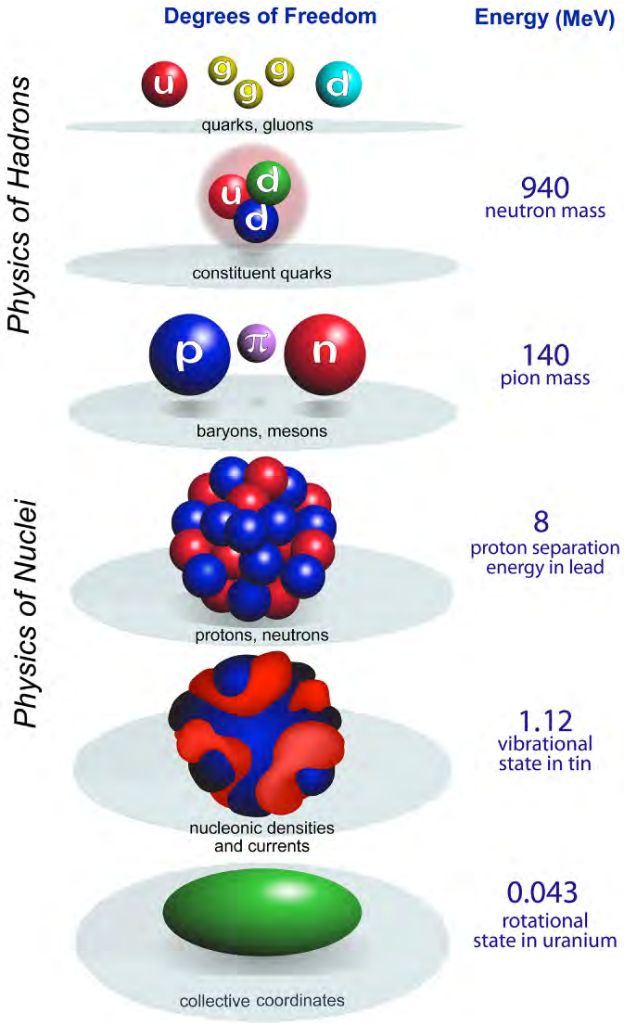

Figure 1.2: Degrees of freedom in nuclear physics reproduced from [2].

Ab initio models start from the basic building blocks, quarks and gluons, which can be described using quantum chromodynamics (QCD). The interactions between nucleons are calculated on the basis of the results of QCD and lattice QCD. Ab initio models are predictive but computationally expensive, so they are limited to light nuclei [18].

Configuration interaction (CI) models shrink the model space to the configuration of

only a part of the nucleons inside a nucleus, so they can be applied to nuclei of up to 100 nucleons [2]. CI models are mostly based on the nuclear shell model and modified according to experimental results. Each model can only predict the physics properties of nuclei for a certain area on the nuclear chart.

For superheavy nuclei, configuration interaction models are also limited by computational power. Density functional theory (DFT) based models, which are widely used in atomic and condensed matter physics, use continuous densities and currents rather than individual particles to deal with collective motions such as rotational and vibrational degrees of freedom [19, 20].

Although nuclear properties can be largely explained using approaches tailored to specific mass regimes, a unified method with predictive power that extends across a wider range (the entire nuclear chart) has always been the pursuit of theories. New experimental findings play a crucial role in challenging and benchmarking these theoretical approaches so that the theory models used to describe the nuclear properties can become more precise and extensive.

1.3 The nuclear shell model

The origin of the nuclear shell model is the observation that the outstanding stability of the nuclei with either proton or neutron number equals certain "magic" numbers (2, 8, 20, 28, 50, 82, and 126) [21, 22], indicating a model similar to the atomic electron shell model.

The nuclear shell model simplifies the strong nuclear force by considering a nucleon as a single particle within the mean field potential created by other nucleons. A Hamiltonian is constructed with matrix elements determined by an empirically chosen potential suitable for the specific mass regime. The eigenvalues and eigenstates, characterized by quantum

numbers (n, l, j, and energy E), are used to predict the properties of the nuclear structure. The potential $V(r)$ used to describe the nucleon interaction is defined in three key areas of the nucleus: interior, surface, and exterior.

In practice, the harmonic oscillator (HO) potential was used initially due to its simplicity and analytical nature, and has been able to reproduce the magic number of 2, 8 and 20. However, the Woods-Saxon potential more accurately reflects empirically obtained nuclear density shapes. This nuclear potential $V(r)$ is employed to generate a spectrum of energy levels available to the nucleons.

For a bound nucleus, the potential should be attractive ($V(r) < 0$) and approximately constant in the interior, assuming a short-range nucleon-nucleon interaction and constant nuclear density. Near the nucleus surface, $V(r)$ decreases to reflect the reduced number of interactions for the outer nucleons. Beyond the interaction range, $V(r)$ approaches zero. For heavy nuclei, the density distribution can be described using a Fermi distribution. The fit to this density distribution gives the Woods-Saxon potential which is defined as

$$V_{WS}(r) = \frac{V_0}{1 + e^{(r-R_0)/a_0}} \tag{1.3}$$

where $R_0 = 1.21$ fm and $V_0 \simeq -30$ MeV. $V_{WS}(r)$ represents the central potential. After including the spin-orbit term, $V(r) = V_{WS}(r) + V_{ls}(r)\frac{\langle ls \rangle}{\hbar}$, the model is able to reproduce all the observed magic numbers [23, 24, 25], as shown in Figure 1.3.

1.4 Shell evolution in beryllium isotopes

Beryllium is the element that has 4 protons, and the particle-bound isotopes range from ^{7}Be to ^{14}Be [26]. The structure of beryllium isotopes has a variety of interesting features

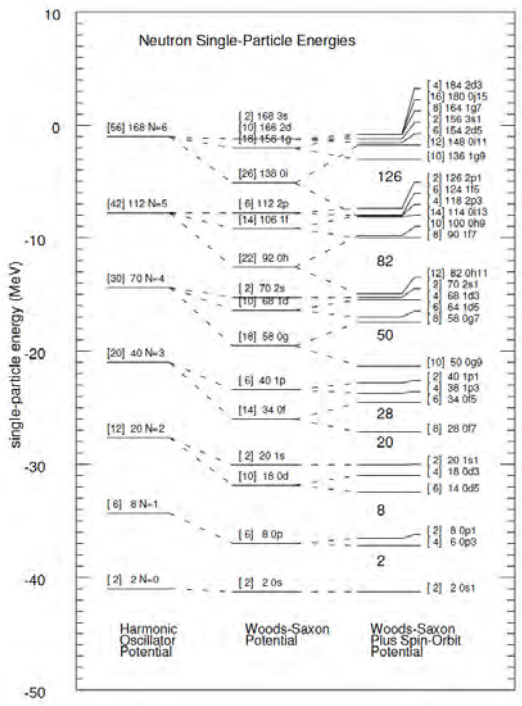

Figure 1.3: Single particle states. Figure reproduced from [2].

despite its small number of nucleons. Although ^{7}Be is the lightest bound beryllium isotope, ^{8}Be can be viewed as a system of 2α particles unbound by only 5.57 eV [27] while ^{9}Be is the only stable beryllium isotope also considered to be a $\alpha - \alpha - n$ Borromean system. The ^{9}Be stability is due to its molecular structure [28, 29, 30] and core excitation [31]. The next isotope of beryllium, ^{10}Be, was experimentally observed to have a weakened cluster structure, an evidence of the reduced size of its charge radius [32, 33]. The $2\alpha + 2n$ cluster structure seen in this latter isotope starts to appear when the excitation energy is close to the neutron and α separation energies.

On the other hand, ^{11}Be was found to be a one-neutron halo nucleus, with 16% of its core-excited component in the ground state observed through the ^{11}Be(p,d)^{10}Be reaction [34]. The ground state of ^{11}Be is $1/2^{+}$ instead of $1/2^{-}$, implying that the last neutron is in the

sd-shell instead of the *p*-shell. The ground state and the lowest 0^+ excited state of ^{12}Be are both mixtures of *p*-shell and *sd*-shell [35]. The parity inversion in ^{11}Be and the observed configuration mixing in ^{12}Be suggest the breakdown of the N = 8 shell closure [36].

The next isotope, ^{13}Be, plays a very unique role in the isotopic chain: it is unbound, right beyond the neutron drip line and belongs to the N = 8 (vanishing) closed shell. The low-lying structure of this isotope would largely inform theoretical models of nuclear structure and shell evolution around N = 8.

The last and heaviest particle-bound isotope of beryllium, ^{14}Be, features a 2-neutron halo and is classified as a Borromean nucleus [37, 38]. According to the simple model of $^{12}\mathrm{Be} + n + n$, the ground state wave function of ^{14}Be would be expected to be dominated by the $d_{5/2}$ orbital. However, due to the level inversion observed in other neutron-rich beryllium isotopes, contribution from some low-lying $s_{1/2}$ strength is expected [39].

Beyond the neutron drip line, ^{15}Be has been observed to decay into ^{12}Be through unbound states in ^{14}Be [40]. The last beryllium isotope observed is ^{16}Be, which is bound with respect to the emission of one neutron but is unbound when it comes to the emission of two neutrons [41].

1.5 Previous experimental results and motivation

1.5.1 Invariant mass spectroscopy

As mentioned above, ^{13}Be is a neutron-unbound nucleus, which means its ground state is above the neutron separation energy. Unbound neutron states cannot be experimentally measured directly because their neutron decay occurs immediately (on the order of 10^{-21} s).

One appraoch to study such short-lived systems is to reconstruct their decay energy, i.e. the amount of energy released in the decay in the center-of-mass frame, using the invariant mass spectroscopy method. A mass is invariant in any inertial frame.

The invariant mass of a single particle or a mass point is just its rest mass m, and satisfies

$$m^2 = \mathbf{P}^2 = E^2 - \mathbf{p} \cdot \mathbf{p} \tag{1.4}$$

where $\mathbf{P} = (E, p_x, p_y, p_z)$ is the four-momentum using $c = \hbar = 1$ as a convention. If the particle decays into multiple new particles, the four-momentum of the whole system is conserved

$$\mathbf{P} = \sum_i \mathbf{P}_i \tag{1.5}$$

In the center-of-mass frame, Equation 1.5 becomes

$$m = \sum_i m_i + E_{decay} \tag{1.6}$$

For a system of multiple particles, the invariant mass M is defined to satisfy

$$\begin{aligned} M^2 &= \left(\sum_i \mathbf{P}_i \right)^2 \\ &= \left(\sum_i E_i \right)^2 - \left(\sum_i \mathbf{p}_i \right) \cdot \left(\sum_i \mathbf{p}_i \right) \end{aligned} \tag{1.7}$$

It is easy to notice that the invariant mass M of the multi-particle system after the decay is exactly the rest mass m of the one particle before the decay.

$$M = m \tag{1.8}$$

The "invariance" across the decay process is a deduction of the conservation of energy and momentum. The decay energy can be expressed as

$$\begin{aligned} E_{decay} &= M - \sum_i m_i \\ &= \sqrt{\left(\sum_i \mathbf{P}_i\right)^2} - \sum_i m_i \\ &= \sqrt{\left(\sum_i E_i\right)^2 - \left(\sum_i \mathbf{p}_i\right)^2} - \sum_i m_i \end{aligned} \tag{1.9}$$

using the energy and momentum vectors of all decay products. Since the rest masses of all the decay products are also known, the quantities to be measured in an experiment are the momentum vectors of every decay product.

1.5.2 Summary of previous experiments

Many experiments on ^{13}Be have been performed over the last 40 years with about half of them using nucleon exchange reactions or the missing mass method to probe the resonance states, and the other half using knockout, breakup, or Coulomb dissociation reactions and the invariant mass technique. Table 1.1 provides a summary of the processes used for each of these experiments.

Experimental data suggest that there are three low-lying states within 2.5 MeV above the threshold as depicted in Figure 1.4: a $1/2^-$ around 0.4 MeV, a $1/2^+$ around 0.8 MeV, and a $5/2^+$ around 2.3 MeV. The $5/2^+$ state is well established, but the assignments of the lower-lying $1/2^\pm$ states still have disagreements between existing measurements. Furthermore, the $1/2^+$ state was claimed to be a resonance state according to some measurements, while it was claimed to be a virtual state by others.

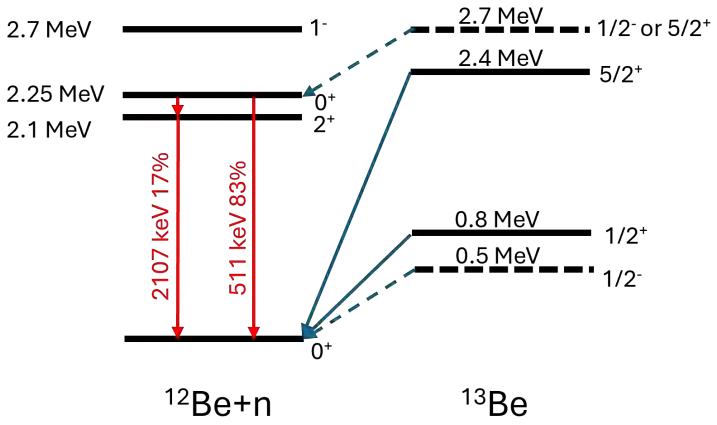

Figure 1.4: Possible level scheme of ^{13}Be and ^{12}Be from a one-neutron emission. The solid lines are measured neutron and γ emissions while the dashed lines indicate the still unresolved population from ^{13}Be to ^{12}Be.

1.5.3 Thesis experiment motivation

A $1/2^-$ state was assigned to the p-wave resonance around 0.4 MeV: this p-wave character was determined from the transverse momentum distribution of ^{13}Be after the one-neutron knockout and subsequent neutron decay into ^{12}Be with no coincident γ-ray measured, thus indicating that the final state of this decay is likely to be the ground state of ^{12}Be. However, the final state could also be the 0^+ isomeric state of ^{12}Be at 2.25 MeV that has a mean life time of 331 ns [42, 43] and emits a delayed γ-ray. Prior experiments using in-flight γ-ray detection were not sensitive to the emission of delayed γ-rays, and therefore no level assignment can be inferred for this 0^+ state: **the location of the $1/2^-$ state is yet to be determined.**

Some theoretical calculations [44] predict that the decay from the $1/2^-$ state in ^{13}Be to the 0^+ state in ^{12}Be is prohibited, but another calculation argues that if there is a second $5/2^+$ state above 2.6 MeV, it can decay to the 0^+ state in ^{12}Be by emitting a d-wave neutron [45]. **Whether p-wave or d-wave, a measurement that is sensitive to the**

one-neutron decay into the 0^+ isomeric state is needed to solve the puzzle of the low-lying structure of ^{13}Be.

This thesis discussed an experiment that was conducted by the MoNA Collaboration [46] at the then National Superconducting Cyclotron Laboratory (precursor of FRIB) [47] of Michigan State University to study the decay of ^{13}Be by one neutron emission into the 0^+(2.25 MeV) isomeric state in ^{12}Be. This experiment also consisted of the first usage of a dedicated new telescope made of a stack of five silicon detectors and a CsI stopping detector to identify the ^{12}Be fragment. The telescope was complemented by 96 modules of the MoNA-LISA neutron array [48] and the gamma ray CAESAR detector [49]. The former was placed about 5 m behind the target while the latter surrounded the telescope to detect the decay of the expected isomeric state into its daughter nucleus. This experiment departed from the usual setup of the MoNA Collaboration that includes a 4 T large gap sweeper magnet thus also tested the possibility for sweeperless experiments for the MoNA Collaboration.

Table 1.1: Summary of previous experiments studying the level scheme of ^{13}Be. The energy above threshold are provided in MeV or, when available, the interaction length a_s in fm^{-1}. The spin-parity assigned to the measured state (J^π) are also indicated.

Author (year)	Reference	Reaction	1/2 state (0.5 MeV)	1/2 state (0.8 MeV)	$5/2^+$ state (2.1 MeV)
Aleksandrov et al. (1983)	[50]	^{14}C + ^{7}Li	-	-	1.8
Ostrowski et al. (1992)	[51]	^{13}C+^{14}C	-	-	2.01 ($5/2^+$ or $1/2^-$)
Korsheninnikov et al. (1995)	[52]	^{12}Be+d	-	-	2.0
von Oertzen et al. (1995)	[53]	^{13}C + ^{14}C	-	-	2.01 ($5/2^+$)
Belozyorov et al. (1998)	[54]	^{14}C + ^{11}B	-	0.80	2.02
Thoennessen et al. (2000)	[55]	^{9}Be + ^{18}O	0.20 ($1/2^+$)	0.80 (1/2)	2.02 ($5/2^+$)
Lecouey (2004)	[56]	^{14}B + C		0.7 ($1/2^+$)	2.4 ($5/2^+$)
Simon et al. (2007)	[57]	^{14}Be + C	-	(-3.2 fm^{-1}) ($1/2^+$)	2.00 ($5/2^+$)
Kondo et al. (2010)	[44]	^{14}Be + p	0.51 ($1/2^-$)	(-3.2 fm^{-1}) ($1/2^+$)	2.39 ($5/2^+$)
Aksyutina et al. (2013)	[58]	^{14}Be + p	0.44 ($1/2^-$)	0.81 ($1/2^+$)	1.95 ($5/2^+$)
Randisi et al. (2014)	[59]	^{14,15}Be + ^{nat}C	0.40 ($1/2^+$)	0.85 ($5/2^+$)	2.35 ($5/2^+$)
Marks et al. (2015)	[60]	^{13}B + ^{9}Be	-	0.73 ($1/2^+$)	2.56 ($5/2^+$)
Ribeiro et al. (2018)	[61]	^{14}Be +CH_2	0.44 ($1/2^-$)	0.86 ($1/2^+$)	2.11 ($5/2^+$)
Corsi et al. (2019)	[62]	^{14}Be + p	0.48 ($1/2^-$)	(-9.2 fm^{-1}) ($1/2^+$)	2.30 ($5/2^+$)
Kovoor et al. (2023)	[63]	^{12}Be+^{solid}D	0.55 ($1/2^-$)	-	2.22($5/2^+$)
Hunt et al. (2023)	[64]	^{12}Be + p	-	0.6 ($1/2^+$)	2.34($5/2^+$)

1.6 Layout of the thesis

This thesis is introduced in Chapter 1 where we also summarize the current state and motivations for studying the ^{12}Be isomeric state. The theoretical background describing the level scheme and the special case of the two $1/2^-$ states of ^{13}Be are detailed in Chapter 2. Chapter 3 describes the various components of our experimental setup and Chapter 4 the various steps followed in our data analysis. The results of this work are found in Chapter 5 and the discussion and conclusion are in Chapter 6.

Chapter 2. Theoretical Background

The theory calculations used in this thesis can be divided into two parts: nuclear structure theories (Section 2.1) and nuclear reaction theories (Section 2.2). NuShellX, a shell model calculation code, is used for nuclear structure theory calculation to obtain nuclear states and their overlaps. And the reaction theories includes the eikonal model that calculates the theoretical cross-section of the one-neutron knock-out reaction of ^{14}Be (Subsection 2.2.1), and the Breit-Wigner line shape that describes the one-neutron decay reaction of ^{13}Be (Subsection 2.2.2).

2.1 Shell model calculations

A shell model calculation begins with selecting a complete basis, determining the matrix elements of the Hamiltonian within this basis, and then obtaining the corresponding eigenvalues and eigenvectors. In this study, the shell model is applied using the formalism described in reference [65]. Wrapper codes are used to incorporate a specific Hamiltonian, allowing NuShellX to compute the overlaps for the second quantization creation operator a^+. These overlaps are subsequently converted into spectroscopic factors (C^2S) and two-nucleon transfer amplitudes. A spectroscopic factor represents the "probability" that the overlap between the initial and final states aligns with the single-particle assumption made in the calculation. The one nucleon transfer amplitudes are used to calculate the one nucleon removal cross sections.

The Hamiltonian used by NuShellX is written as the sum of three terms

$$H = H_{nn} + H_{pp} + H_{pn} \tag{2.1}$$

where H_{nn} is the interactions between valence neutrons, H_{nn} is the interactions between valence protons, and H_{pn} is the proton-neutron interactions.

The NuShellX uses a proton-neutron coupled basis

$$|B, J\rangle = |[(J_p, \alpha_p) \otimes (J_n, \alpha_n)]^J\rangle \tag{2.2}$$

where J_p, J_n are angular momenta of proton/neutron subspaces, and α_p, α_n are additional quantum numbers. And B represents the set of quantum numbers (J_p, p, J_n, n).

NuShellX uses Lanczos iterations to diagonalize the Hamiltonian and find low-lying eigenvalues/eigenvectors without full matrix storage. The initial and final eigenvectors are

$$|\Psi_i; J_i\rangle = \sum_{B_i} A_i(B_i) \, |B_i; J_i\rangle \tag{2.3}$$

$$\left|\Psi_f; J_f\right\rangle = \sum_{B_f} A_f(B_f) \left|B_f; J_f\right\rangle \tag{2.4}$$

where A_i and A_f are eigenvector coefficients.

The spectroscopic factor for nucleon removal is

$$C^2S = \frac{1}{2j+1} \left|\langle \Psi_f; J_f \| a_j \| \Psi_i; J_i \rangle\right|^2 \tag{2.5}$$

where $\langle \Psi_{A+1}; J_f \| a_j \| \Psi_A; J_i \rangle$ is the reduced matrix element, $|\Psi_A; J_i\rangle$ is the initial state

wavefunction (mass A, spin J_i), $|\Psi_{A+1}; J_f\rangle$ is the final state wavefunction (mass $A+1$, spin J_f), a_j is the annihilation operator for orbital j, and $2j+1$ is the degeneracy factor.

In this study, the spectroscopic factors for both the one-neutron knockout cross sections populating the states of ^{13}Be and the subsequent one-neutron decay of the neutron-unbound ^{13}Be are examined through

$$^{14}\mathrm{Be} \rightarrow {}^{13}\mathrm{Be}^{*} + n \tag{2.6}$$

$$^{13}\mathrm{Be}^{*} \rightarrow {}^{12}\mathrm{Be}^{*} + n \tag{2.7}$$

The spectroscopic factors are necessary for cross-section calculations.

The Hamiltonian chosen for the present work is *psdmod*, which was modified from the *psdwbt* effective interaction within the full *p-sd* model space [66]: The *p-sd* shell gap was reduced by approximately 3 MeV to explain the multiparticle-multihole states at N=Z=8 like the 0_2^+ state in ^{16}O. The *p-sd* shell gap was increased again by 1 MeV to coincide with a measurement of the configuration mixing of the ground state and the 0_2^+ isomeric state of ^{12}Be [67]. Therefore, the above Hamiltonian is suitable for this work.

The shell model calculation will give the spectroscopic factors of possible reaction channels, so that the reaction properties like the cross-section and momentum distributions can be calculated with reaction theory models as detailed in the next section.

2.2 Reaction theory calculations

2.2.1 One-neutron knockout reaction of ^{14}Be

The one-neutron knockout reaction of ^{14}Be was calculated using the eikonal model, as detailed in [68, 69, 70]. This model assumes sudden (fast collisions) and eikonal (forward-scattering) interactions of a projectile of mass A with a target, which are relevant to the single-nucleon removal channel as studied in our experiment. In this context, the state α of the reaction residue of mass (A - 1) acts as a spectator. Consequently, the yield of residues in a specific final state α reflects the contribution (or parentage) of this configuration to the ground-state wave function of the projectile. The partial cross section for nucleon removal from a single-particle configuration j^π, which populates the residue final state α with excitation energy E^*_α, is given by:

$$\sigma_{th}(\alpha) = \left(\frac{A}{A-1}\right)^N C^2S(\alpha, j^\pi)\sigma_{sp}(j, S^*_\alpha) \tag{2.8}$$

where $S^*_\alpha = S_{n,p} + E^*_\alpha$ represents the effective separation energy for the final state α, and $S_{n,p}$ is the nucleon separation energy from ground-state to ground-state. The factor N, which appears in the A-dependent center-of-mass correction that multiplies the shell model spectroscopic factors $C^2S(\alpha, j^\pi)$, corresponds to the number of oscillator quanta associated with the major shell of the removed particle [71]. The single-particle cross section, σ_{sp}, is the sum of the elastic and inelastic breakup contributions to the reaction, $\sigma_{sp} = \sigma^{elas}_{sp} + \sigma^{inel}_{sp}$, and is calculated assuming that the removed nucleon's single-particle wave function (or overlap) is normalized.

The calculation of σ_{th} for each projectile requires several key inputs: (i) realistic spectra and C^2S values, (ii) accurate residue and nucleon-target optical potentials, along with their derived scattering S-matrices used in the eikonal model's impact parameter integrals for σ_{sp}^{elas} and σ_{sp}^{inel}, spatially localizing the reactions, and (iii) realistic geometries for the radial wave functions (overlap functions) corresponding to the initial bound states of the removed nucleons in the projectile's ground state. For exotic nuclei, many of these parameters are not fully constrained by experimental data. The approach taken in the analyses discussed in this dissertation is to utilize the best available shell model calculations for input (i), while the shapes and radial size parameters of the optical potentials and overlaps for inputs (ii) and (iii) are constrained using Hartree-Fock calculations of neutron and proton densities for the residues, as well as the root-mean-square (rms) radii of orbitals in the Hartree-Fock mean field. The detailed procedure applied to all the data sets discussed in this thesis is provided in [72].

2.2.2 Breit-Wigner line shape of the ^{13}Be one-neutron decay

The decay of an unbound resonant state is defined by its central energy (E_{decay}) and width (Γ_l). To extract these values from experimental data, deconvolution is typically needed to correct for resolution and acceptance effects. Alternatively, a decay line shape with specified energy and width can be simulated and then processed through the experimental resolutions and acceptances, enabling a direct fit to the experimental data to determine the energy and width of the decay.

Specifically, individual isolated resonance states can be described by a single-level Breit-Wigner cross-section distribution [73]. The energy-dependent Breit-Wigner line shape used

in our analysis can be expressed as:

$$\sigma(E) \propto \frac{\Gamma_l(E)}{\left[E_{decay} - E\right]^2 + \frac{1}{4}\left[\Gamma_l(E)\right]^2} \tag{2.9}$$

Here, E is the relative energy between the fragment and the neutron, and E_{decay} is the resonance energy of the isolated state $\Delta_l(E_{decay}) = 0$. The phase factor typically included in this expression is not required in this context since only a specific decay channel has been observed in the reaction. The partial width of the state is denoted by $\Gamma_l(E)$. Similarly, since only the outgoing decay channel of the resonance was observed and there is only a single decay channel via a one-neutron emission, the partial width in this case is also the total width (referred to simply as the width):

$$\Gamma_l(E) = 2P_l(E)\gamma^2 \tag{2.10}$$

The width depends on both energy and orbital angular momentum. The factor of 2 represents the reduced width squared, containing the wave function information of the states. $P_l(E)$ is the penetrability function, which is related to the spherical Bessel functions.

The Breit-Wigner line shape for the neutron-unbound decay can be derived using R-matrix theory, following the formalism outlined in reference [74].

Chapter 3. Experimental Setup

The experiment was performed at the National Superconducting Cyclotron Laboratory (NSCL) [47] in September 2020 and conducted in the S2 vault. It was also the last experiment performed by the MoNA Collaboration [46] at NSCL. The Coupled Cyclotron Facility (CCF) and the A1900 Fragment Separator produced a secondary beam of ^{14}Be by fast fragmentation of an ^{18}O primary beam. The experimental setup included a reaction target, a charged particle telescope, the CAESAR γ-array, and a subset of the MoNA-LISA (Modular Neutron Array-Large multi-Institutional Scintillating Array) array. This chapter details the beam production and associated detectors utilized to monitor the beam and reaction products, along with the data acquisition system.

3.1 Beam production

The NSCL coupled cyclotron facility and the A1900 fragment separator are shown in Figure 3.1. An electron-cyclotron resonance (ECR) ion source produced $^{18}O^{3+}$ ions which were extracted and accelerated through the K500 cyclotron to 10.91 MeV/u. The beam was then sent to the K1200 cyclotron where the ions were stripped of their remaining electrons and accelerated to 120 MeV/u. The fully stripped ^{18}O ion beam then impinged on a 2350 mg/cm^2 thick beryllium production target, where a range of predominantly lighter fragments produced in fragmentation reactions are emitted at forward angles.

To isolate the desired secondary beam of ^{14}Be from the rest of the fragments, the A1900 fragment separator was utilized. It was a magnetic separator consisting of 4 main dipoles and 8 quadrupole triplets. The dipole magnetic fields were tuned to the magnetic rigidity ($B\rho = p/q$) of the ^{14}Be fragment of interest (4.63 Tm for segment 1 and 2, 4.56 Tm for segment 3

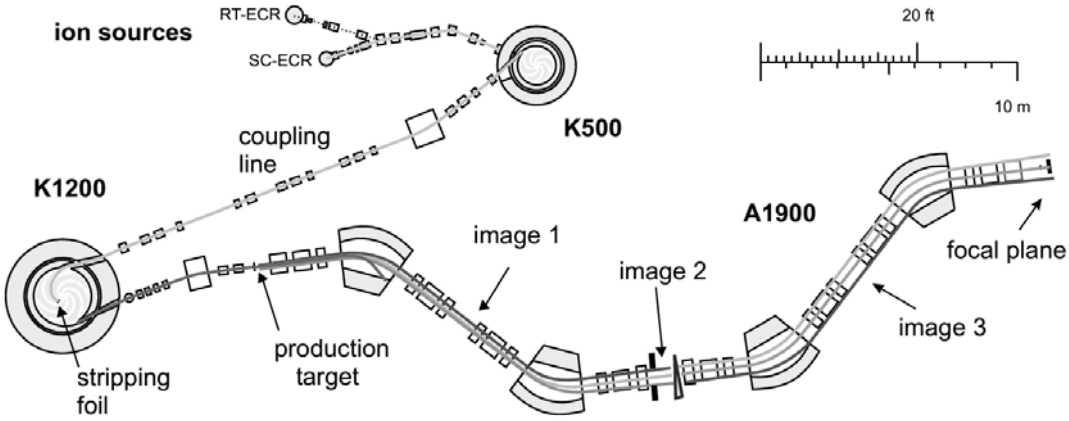

Figure 3.1: A schematic of the NSCL coupled cyclotrons and the A1900 fragment separator utilized in this experiment. Figure reproduced from reference [3].

and 4). The fragments followed different trajectories through the magnets according to their magnetic rigidity, and a set of slits (located at image 1 and image 2 pointed out in Figure 3.1) was used to select a rigidity range corresponding to a momentum acceptance of 1.44% full width. To further tune the separation of the fragments, a 300 mg/cm^2 aluminum wedge was included in the middle of the A1900 fragment separator at image I2: the energy loss through the aluminum wedge is dependent on the atomic number (Z) changing the charged fragments with similar $B\rho$ before the wedge to have lower momenta and thus get separated in the magnets downstream. A second set of slits located at the focal plane (pointed out in Figure 3.1) was used after the wedge to further filter the charged fragments of different Z.

3.2 The S2 experimental vault

After the fragment separator, the ^{14}Be secondary beam was 34% pure with an energy of 78.2 $\pm$ 1.1 MeV/u before passing through the A1900 focal plane timing scintillator. The beam was then transported to the experimental area of the S2 vault where our experiment

was conducted as depicted in Figure 3.2.

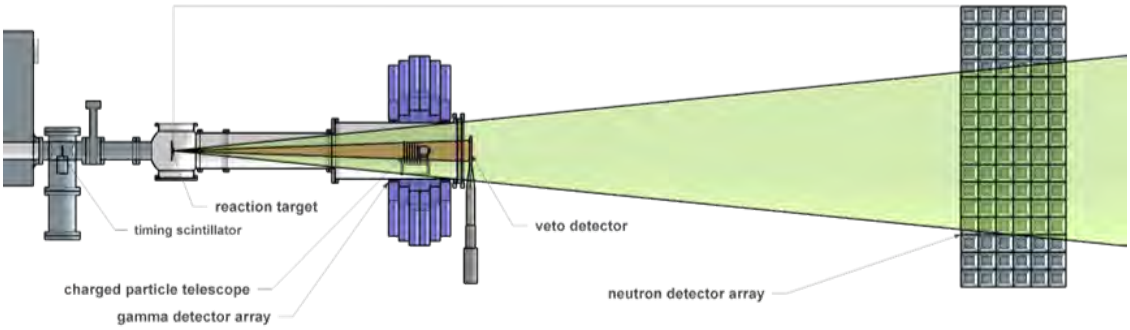

Figure 3.2: Side view of the experimental setup in the S2 vault showing the reaction target, charged particle telescope and neutron array.

3.2.1 Timing scintillators

Two plastic scintillator based timing detectors located upstream of the reaction target were utilized to measure the time-of-flight of the secondary beam. The first one (start detector) was the extended focal-plane (XFP) scintillator located 31.6 m upstream from the reaction target, made of a 1000 μm thick BC404 material and coupled to a Hamamatsu R329-02 photo-multiplier tube (PMT). The second one was the target scintillator located 63 cm upstream of the reaction target, made of a 420 μm thick BC404 material and also coupled to a Hamamatsu R329-02 PMT. The measured time-of-flight between the two scintillators had a resolution of 2 ns and was used to further isolate the ^{14}Be secondary beam. The target scintillator was also the timing reference for all detectors used in our setup.

3.2.2 Reaction target

The reaction target consisted of a 486 mg/cm^2 thick beryllium. The beam energy in front of the target was 76.5 ± 1.1 MeV/u, taking into account the loss through two parallel plate

avalanche counters (PPACs) beam position monitors and the target scintillator, all positioned upstream of the reaction target. Unfortunately, the signals from the PPACs were too noisy and thus not used in the analysis described in this dissertation.

3.3 Charged particle telescope

A dedicated charged particle telescope was developed and used in the experiment (see Figure 3.3) to perform the particle identification (PID) of the various charged fragments, as well as measure the momentum of the daughter ^{12}Be fragment emitted from the ^{13}Be decay. It

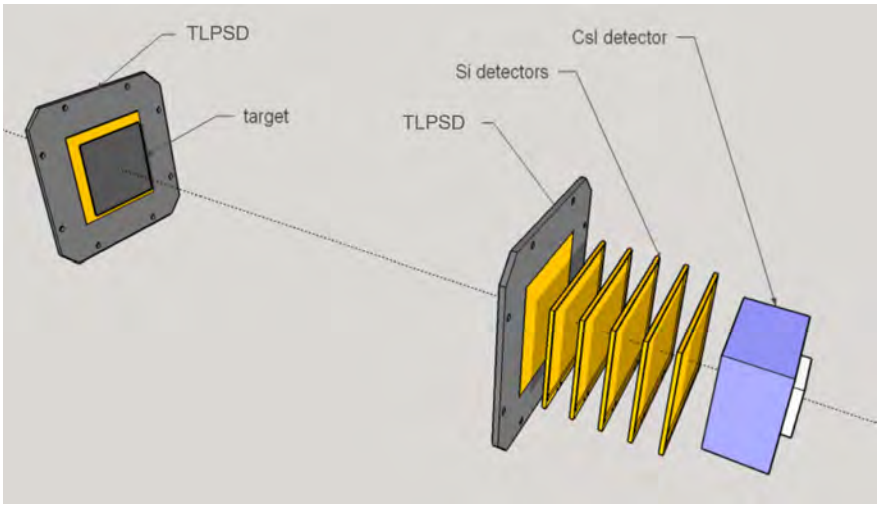

Figure 3.3: A schematic drawing of the charged fragment telescope.

consisted of 2 Tetra-Lateral Position Sensitive Detectors (TLPSDs), 5 silicon PIN detectors, and a CsI(Tl) calorimeter. The specifications of these detectors are listed in Table 3.1.

All the telescope signals were connected to pre-amplifiers (MESYTEC MSI-8) with the ability to adjust all individual voltage settings. The first TLPSD was placed 9 mm upstream of the reaction target. The remaining detectors were grouped together and placed downstream of the reaction target with the front face of the CsI(Tl) detector located at 140 cm.

Table 3.1: Specifications of the telescope detector components.

Detector Name	TLPSD	Silicon PIN	CsI
Detector Type	MSPSD TL63	SI-PIN MSX35-500	CsI(TL)
Manufacturer	Micron	Micron	Scionix
Active Area (cm^2)	6.25×6.25	5×7	5×5
Thickness	140 μm	500 μm	3 cm
Bias (+V)	$> 10 - 12$	> 40	> 35
Energy Resolution	N/A	2.1% FWHM	$< 6\%$ FWHM

The spatial configuration of the second TLPSD, 5 silicon PIN detectors and the CsI(Tl) detector is shown in Figure 3.3, the distance between the front face of the second TLPSD and the first silicon PIN was 14.6 mm, while the neighboring 2 silicon PIN detectors had a 15 mm difference in the z-position. The distance between the front face of the last silicon PIN and the CsI detector was 12.3 mm.

The silicon PIN detectors measured the energy loss and the CsI(Tl) detector stopped the fragments to measure their total kinetic energy at that location. Together, these detectors were used to perform the particle identification (PID). The sum of the energy deposited in all detectors can also be used to get the total kinetic energy of the fragment or the magnitude of its momentum at the reaction vertex within the target. The signals of the TLPSDs were also too noisy and could not be used for position measurements. The fragment momentum, together with the neutron momentum, was utilized to calculate the single neutron decay energy of ^{13}Be.

3.4 Veto detector

A plastic scintillator was placed downstream of the telescope to detect charged particles that were not stopped inside the CsI(Tl) detector, and veto these events. The veto detector

covered only a slightly bigger solid angle as the telescope, so charged particles originating from the target and bypassing the charged particle telescope were not vetoed.

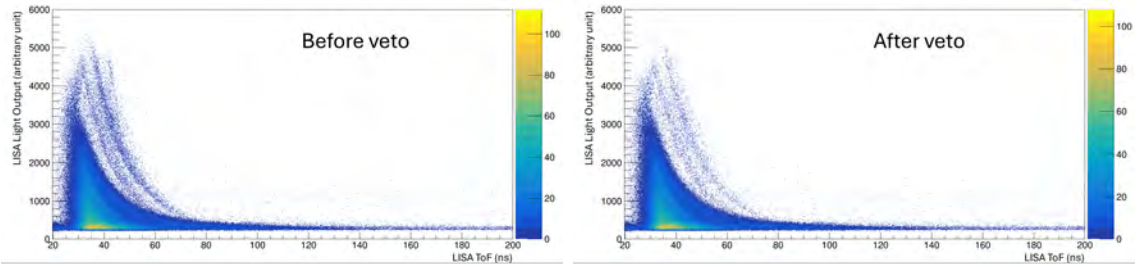

Figure 3.4: Measured light output in the MoNA-LISA array as a function of the time-of-flight without (left) and with (right) requiring a veto signal.

3.5 CAESAR array

The CAESium-iodide scintillator ARray (CAESAR) [49] was placed around the CsI(Tl) calorimeter to measure the delayed γ-rays from the stopped ^{12}Be fragments. CAESAR is a high-efficiency spherical-shaped detector array made of 192 CsI(Na) crystals arranged into 10 rings as shown in Figure 3.5.

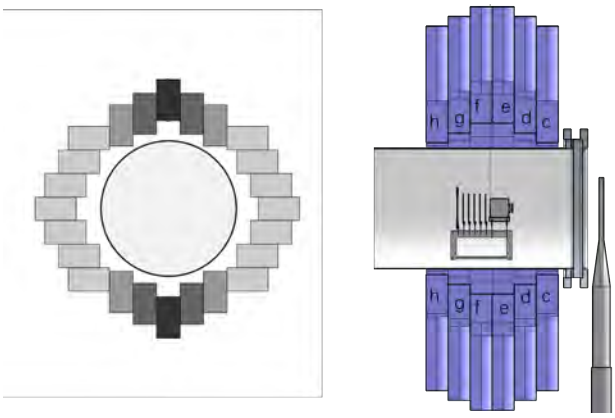

Figure 3.5: A schematic drawing of CAESAR around the charged fragment telescope.

In this experiment, only six center rings (from c to h) were used because the diameter of the beam pipe around the telescope detectors was too large to fit into rings a, b, and

i, j. Each ring from c to h holds 24 detectors of 2.13" × 2.13" × 4". The material of the detectors was chosen to be CsI(Na) because of its 30% higher stopping power than NaI(Tl), with comparable intrinsic energy resolution, timing property and cost. The middle plane of the CAESAR array (between ring f and ring e) aligned with the front face of the CsI detector in the telescope, at 140 cm from the reaction target.

3.6 MoNA-LISA array

In this experiment a subset of the Modular Neutron Array (MoNA) and the Large multi-Institutional Scintillating Array (LISA) [75] was utilized to detect the emitted neutrons and reconstruct their four-momenta from their hit position and time-of-flight.

MoNA and LISA each consists of 144 plastic scintillator detectors with dimensions of 200 cm × 10 cm × 10 cm that are coupled to photo-multiplier tubes (PMTs) at each end through light guides.

The 2 m length of the detector bars extends along the horizontal (x) direction. The standard configuration of the array is built by stacking 9 layers, each made of sixteen detectors along the vertical (y) direction: the MoNA layers are labeled A through I, and the LISA layers are labeled J through R. The stacking is carried out along the beam axis (z) direction and can be arranged in a variety of configurations.

Each of the LISA bars, made from the EJ-200 [75] plastic scintillator material, is individually wrapped with a layer of reflective material and a black plastic on top to reduce light leaks and avoid introducing ambient light. The PMTs coupled to the detectors are Hamamatsu R329-02 [75]. Neutrons interact with the hydrogen and carbon nuclei in the plastic detector volume to generate scintillation photons along the recoils tracks within the

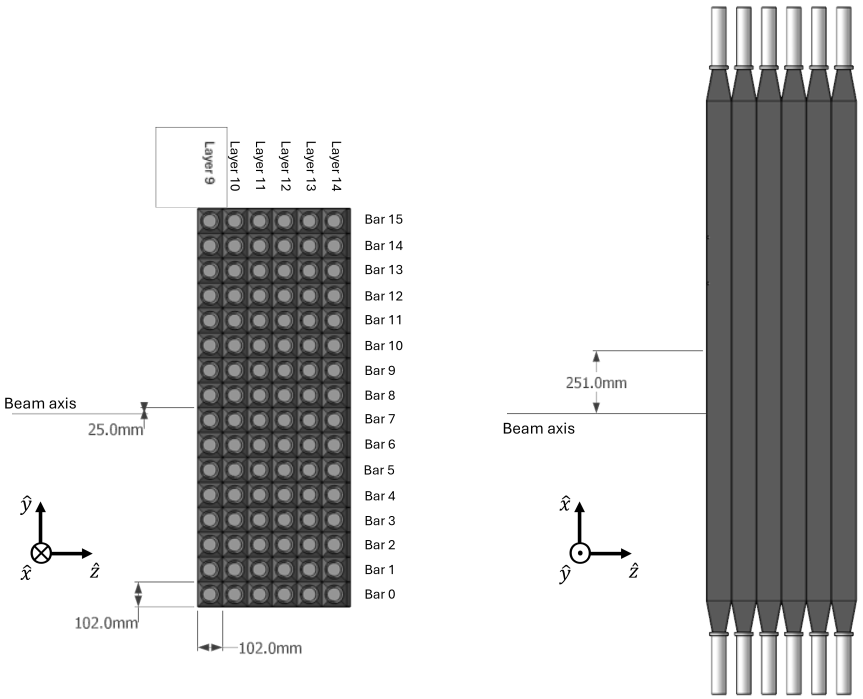

Figure 3.6: LISA experimental setup. The left panel is viewed from the side, and the right panel is viewed from above. Neutrons travel left to right through the array. The center of the array is offset from the beam axis 251 mm in x-direction and 25 mm in y-direction.

bar: since the mass of hydrogen is similar to that of the neutron, the proton recoil energy is larger than the recoil energy of the carbon nuclei, thus generating more scintillation light. The light then propagates to both ends of the bar and is detected by the two PMTs: both the anode signal for timing information and the dynode signal for the charge were collected.

In this experiment, only six layers of LISA from J to O (that will also be referred to as 9 to 14) were used. The six layers were placed next to each other. Layer 9 is the front (upstream) layer and the individual bars were numbered 0 to 15 from bottom to top. The distance from the reaction target to the front (upstream) face was surveyed to be 450 cm. Figure 3.6 shows a picture of the LISA array and the coordinate reference frame that were used for our experiment. Since only detectors of LISA are used, the array will be referred to as LISA instead of MoNA-LISA in the following text.

The time difference between the left and right PMT anode signals was used to determine the horizontal (x) position of a neutron interaction along the bar while the average of the two timing signals was used to determine the time-of-flight from the target position to the neutron interaction. Segmentation along the vertical (y) direction and the beam axis (z) direction allow determination of a 3-dimensional location for the neutron interaction. Under the approximation that the neutrons originate from the center of the reaction target, this provides all the necessary information for the reconstruction of the neutron four-momentum at that location.

The charge collected from the dynode represents the light output from the scintillator, which does not correspond to the kinetic energy of the neutron; however, it can assist in neutron event selection.

3.7 Electronics and Data Acquisition System

The electronics utilized in this experiment were a combination of the VME-based electronics used for the LISA array and the digital data acquisition system (DDAS) used for all other detectors, including the charged particle telescope and the CAESAR γ array. Synchronization between the two systems was critical for the correct event characterization. A schematic of the entire data acquisition system is depicted in Figure 3.7.

The detectors were connected to a logic system which splits into three "levels":

Level 1 that controlled each layer of the LISA array;

Level 2 that controlled the entire LISA array; and

Level 3 that controlled the coincidence between LISA and all other detectors, and is re-

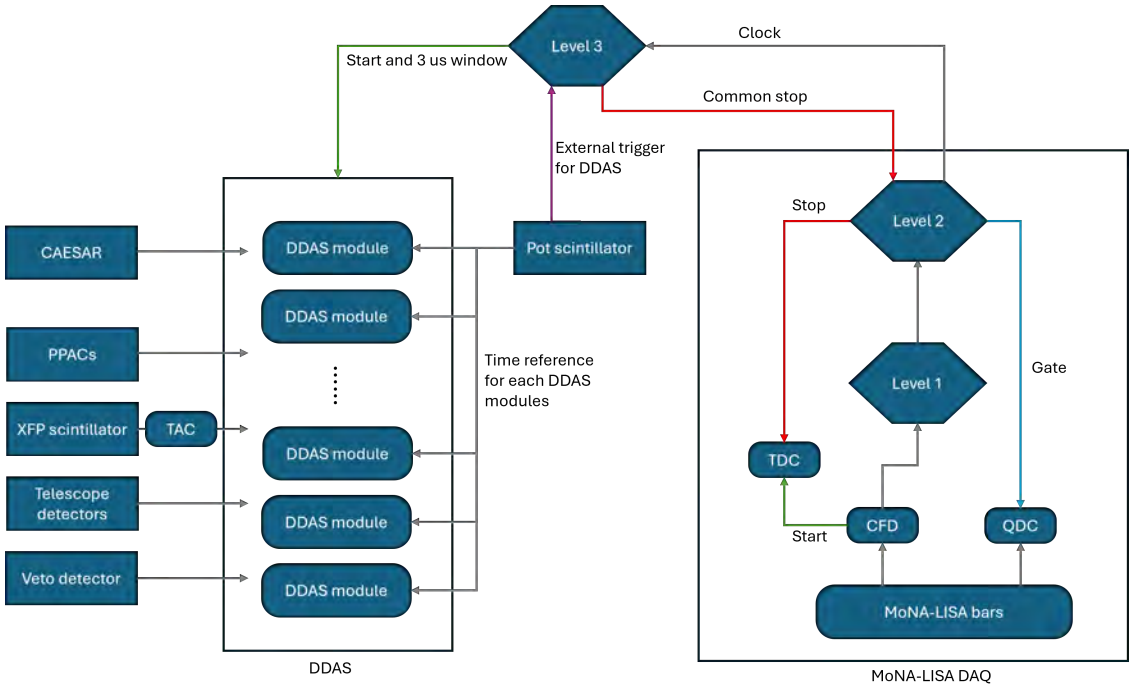

Figure 3.7: A schematic diagram of the DAQ system.

sponsible for generating a system trigger and synchronizing the timestamp between the 2 systems.

The levels 1 and 2 were handled by the Xilinx Logic Modules (XLMs) with field-programmable gate arrays (FPGAs), and the level 3 was realized with the DDAS setup. The system trigger came from the target timing scintillator, and was distributed to both level 2 and DDAS.

3.7.1 LISA electronics

Each of the PMTs for each LISA bar had an anode signal used for timing and a dynode signal used to measure the amount of generated charge. Each PMT anode signal was sent to a constant fraction discriminator (CFD), which output was then sent to both a time-to-digital converter (TDC) and an XLM for the subsystem trigger logic. The CFD provided the start signal for the TDC, and the stop signal was generated from the target (pot) scintillator. Each

PMT dynode signal was sent to a charge-to-digital converter (QDC) module that integrates the charge collected to determine the amount of scintillation light detected. The time (TDC) and charge (QDC) signals were read out by the DAQ computer. The synchronization with DDAS was done through a 10 MHz clock signal generated by the level 2 module and used by both LISA and the DDAS system. The clock ran non-stop and was reset for both systems at the beginning of each run.

3.7.2 Digital Data Acquisition System

The Digital Data Acquisition System (DDAS) utilized in this experiment was a 250 MHz XIA Pixie-16 system. It was set to accept an external trigger that worked as a master trigger for all DDAS channels and an external clock for time stamping. This external trigger was generated by the target scintillator, which was sent through a discriminator and then served as the system trigger for both LISA and DDAS, as well as the timing reference for each DDAS module.

The DDAS had two sets of clocks: internal and external. The former was generated by the DDAS itself, and reset only when the readout software was restarted. It had a frequency of 250 MHz (period is 4 ns), and was used for time-of-flight. The latter was a 10 MHz (period 100 ns) clock provided by the level 2 trigger of LISA, and used only to synchronize time stamps with LISA.

The external clock and external trigger in DDAS were set by specific modules called breakout modules. The connection between a breakout module and a DDAS module was enabled by a harlink cable. There were five harlink connectors that enabled different inputs/outputs in the breakout modules.

3.7.3 Data acquisition software

The data acquisition (DAQ) software used by this experiment was NSCLDAQ version 11.3 running on a dedicated DAQ computer (spdaq09). LISA and DDAS had their own ring buffers, each with a single producer (LISA or DDAS) and multiple consumers (event builder, writing into files, or online data visualization and analysis). More details can be found in the NSCLDAQ documentation [76]. Figure 3.8 shows the data flow of the DAQ software.

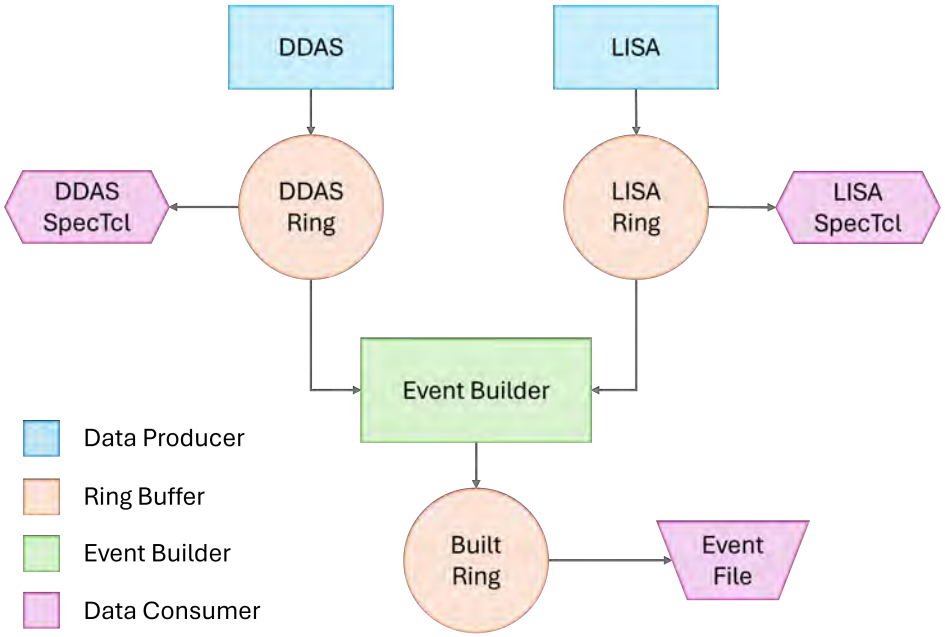

Figure 3.8: Data flow of the DAQ system.

The ring buffers of LISA and DDAS were read by the event builder, and converted through the built data go into the built ring buffer. The outputs were then written into event files. Other consumers for the LISA and DDAS ring buffers were individual SpecTcl scripts [77] used to monitor and analyze the data in real time.

The online event builder used a 10 μs event building time window that was set long enough to record traces of the signals from the telescope detectors. However, this long time window caused issues like observing two beam particles in the same event or one physical

event cut in half. The event building was thus modified in the process of converting the event files to root files with a shorter event building time window of 3 μs.

Chapter 4. Data Analysis

The goal of the data analysis is to extract physical properties from the detected signals and to reconstruct observables from the nuclear reaction. These observables are then compared with simulations in order to test theoretical predictions for the reaction.

The data analysis consists of four steps: calibration, event selection, physics interpretation, and simulations of the reaction. The calibration step converts electrical signals back to the parameters representative of the physical interactions between the particles and detectors, such as the energy deposited, time-of-flight, or position. The event selection step isolates the events that correspond to the reactions of interest which can be identified by their unique signatures from the detector responses. In the physics interpretation, the calibrated and selected data are used to reconstruct the parameters of the reactions. These parameters are then compared to simulations to extract observables related to the structure of the nuclei of interest such as the decay energy and cross-section.

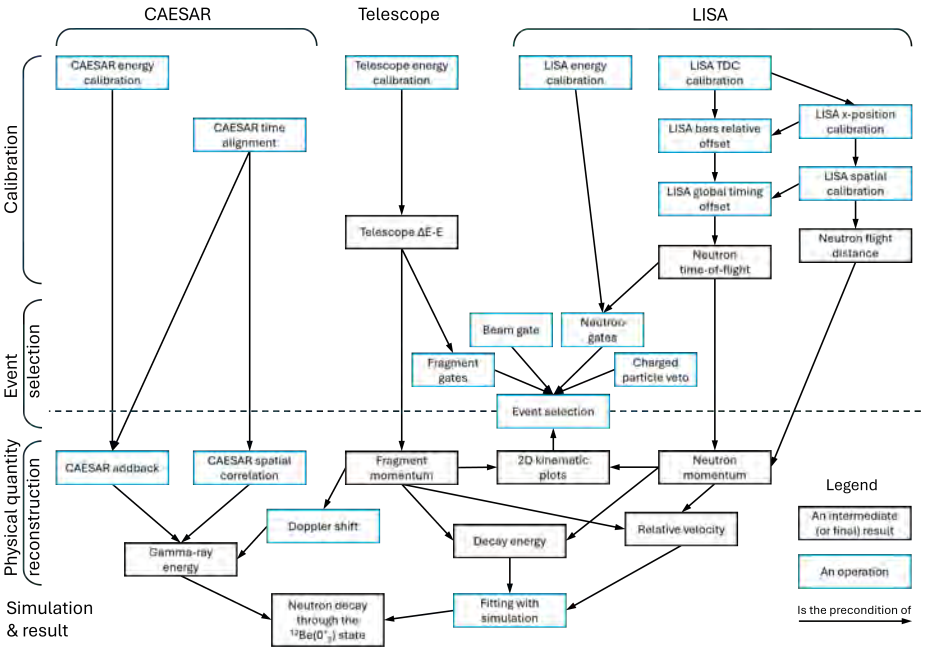

Figure 4.1: Schematic of a typical data analysis procedure.

Figure 4.1 shows a schematic of a typical data analysis procedure. The following sections describe in detail the various steps mentioned above and applied to each of our detectors described in Chapter 3.

4.1 LISA Calibration

4.1.1 LISA TDC calibration

The Time-to-Digital-Conversion (TDC) calibration uses a pulser with a fixed period to convert TDC channels to real time. In addition to the traditional linear fit method, a convolution method was explored.

4.1.1.0.1 Linear fit method Figure 4.2 shows the data for a pulser set at an interval of 10 ns (left panel) and the corresponding plot of the channel number versus the peak number including a linear fit (left panel).

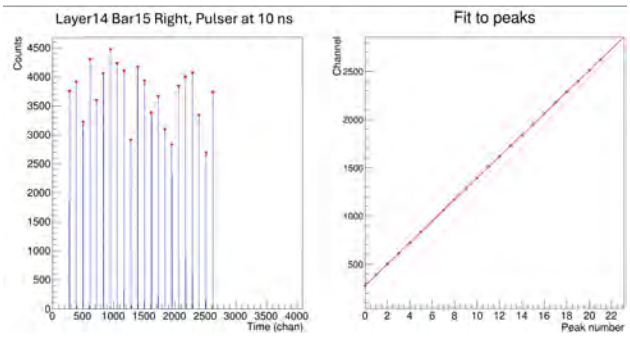

Figure 4.2: Linear fit method. Left panel: TDC data for a sample detector bar (layer 9, bar 0) for a pulser period of 10 ns.; Right panel: Peak channel vs peak number. The red line corresponds to a linear fit.

Since each peak is located at a well-defined time, one can convert the extracted slope to ps/channel. The left and right photo-multiplier tubes (PMTs) for all 96 LISA bars were calibrated using this procedure.

4.1.1.0.2 Convolution method The convolution method consists of a multi-step algorithm, which shifts the one-dimensional TDC spectrum bin-by-bin, multiplying each shifted spectrum with the original one and finally taking the integral of the final distribution: for each shift (e.g., offset), the result (e.g., product integral or convolution) will be close to zero if the spectra do not overlap.

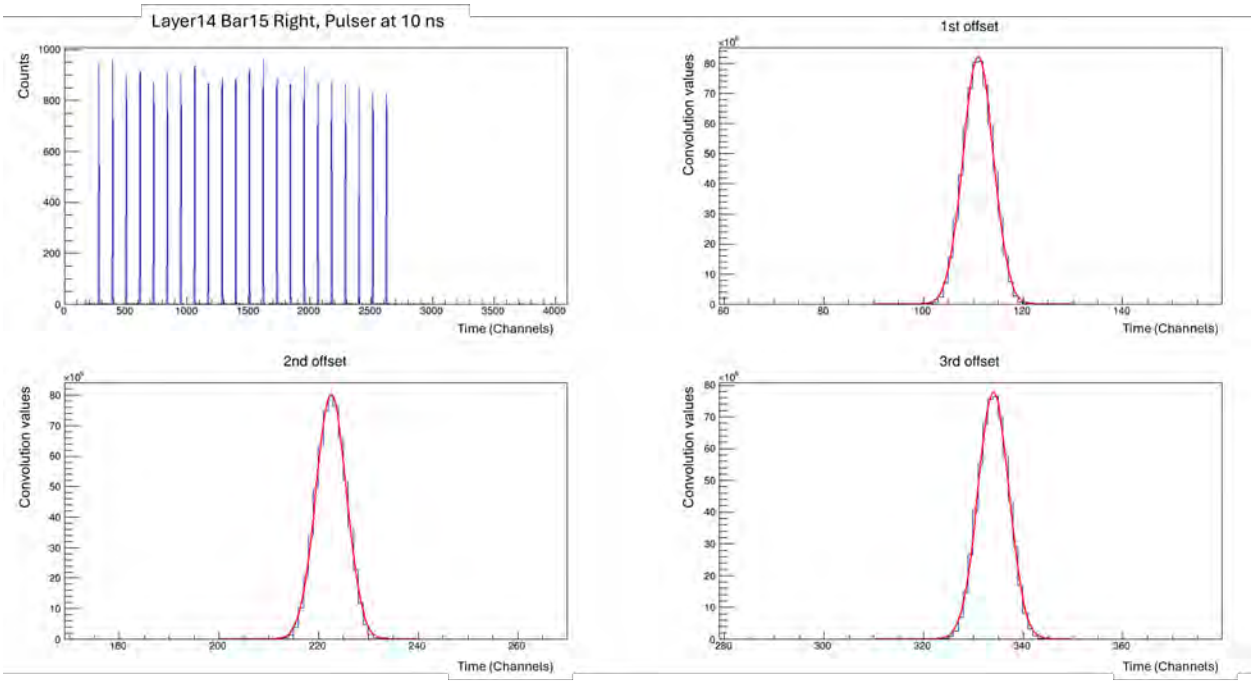

Figure 4.3: Principle of the convolution method: the original spectrum (top-left panel) is shifted until the product integral is non-zero for given multiple integers as depicted in the first (top-right, $\times 1$), second (bottom-left, $\times 2$) and third (bottom-right, $\times 3$) offsets.

The convolution plotted against the offset allows one to identify the integer multiples of the pulser period oscillating between large numbers and very small values (almost zero). The peaks of all offset spectra were then fitted with Gaussian distributions (Figure 4.3). The mean of the fits provides the calibration. The precision of the results was similar to that of the linear fits, so the results of the convolution method were used for calibration.

4.1.2 LISA energy calibration

Prior to the experiment the high voltages of the PMTs were approximately gain-matched to align the cosmic ray peaks. After the experiment the cosmic-rays peaks were used to calibrate the energy deposited in each detector, which is proportional to the light output of the scintillator bar. As shown in Figure 4.4, the cosmic ray peaks in the 96 detector bars are aligned at a certain value. For a few detectors (layer 9 bar 6 and layer 10 bar 2), one of the PMTs was decoupled and these detector bars were removed from the analysis.

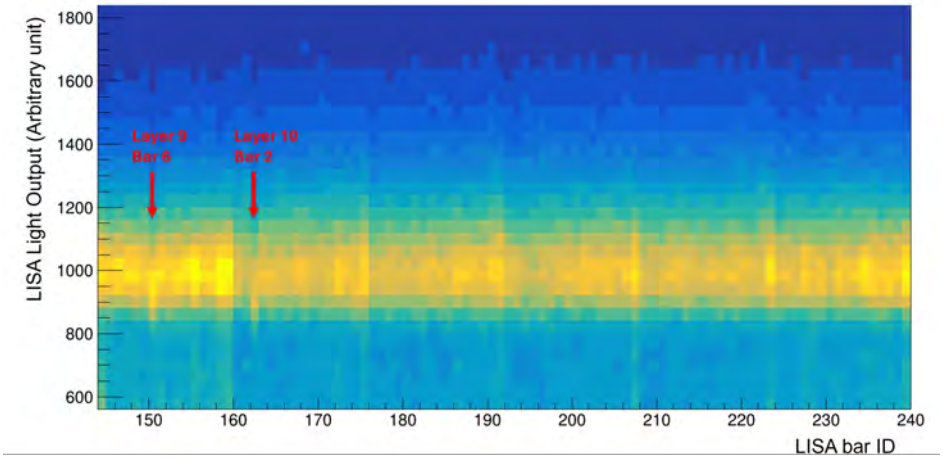

Figure 4.4: LISA light output as a function of the bar ID for a cosmic ray run. The bar IDs of 144 through 159 correspond to the front layer (Layer 9). The cosmic ray peaks are aligned at around 1000 (arbitrary unit). Layer 9 bar 6 and layer 10 bar 2 are the two detectors that one of the PMTs was decoupled, so the cosmic ray peaks of them are lower than other detectors.

4.1.3 LISA horizontal x-position calibration

While the y- and z-position of a hit in the LISA array are determined by which bar the hit was recorded from with a precision of ± 5 cm, the x-position is determined by the time difference between the left and right PMTs. Cosmic rays are used to calibrate the LISA x-position: two Fermi functions were used to fit the left and right edges of the square-shaped

($T_{Left} - T_{Right}$) distributions for each bar. The left and right edges are then placed at -100 cm and 100 cm, respectively, through a linear transformation. Figure 4.5 shows a typical uncalibrated x-position spectrum and the fit.

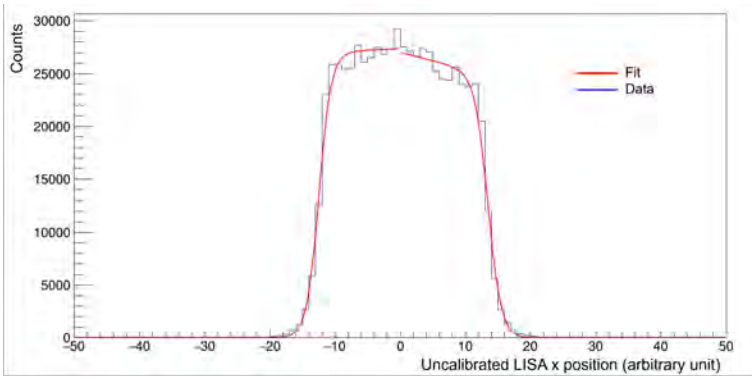

Figure 4.5: A typical measured x-position from LISA. The red lines are the two modified Fermi functions that fit the edges of the distribution which correspond to the left and right end of the detector bar.

Figure 4.6 shows the calibrated LISA x-position as a function of the bar ID. The x-positions of all detectors are aligned between -1 m to 1 m. The two detectors that have issues are also marked in the figure, and they are removed from further analysis.

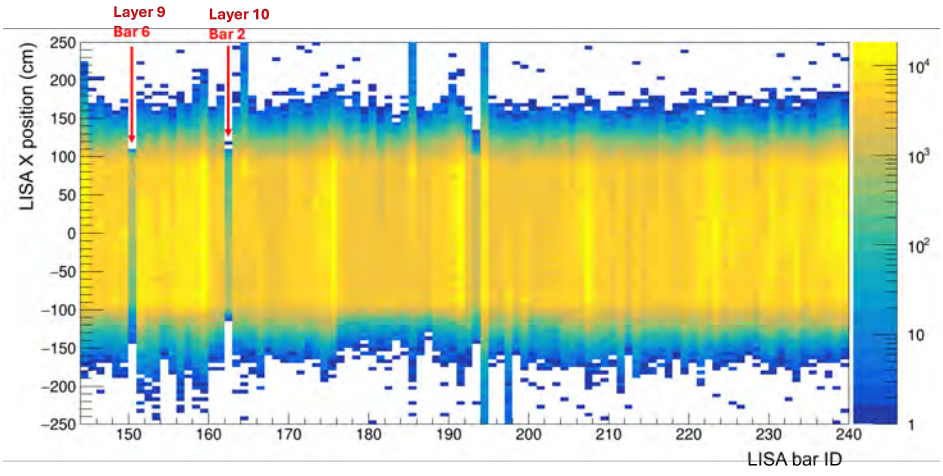

Figure 4.6: LISA x-position as a function of the bar ID for a cosmic ray run. Layer 9 bar 6 and layer 10 bar 2 are the two detectors that one of the PMTs was decoupled. Their x-position distributions are extremely uneven from one side to the other.

4.1.4 LISA T_{mean} offset

The arithmetic average of the left and right LISA PMT times (T_{mean}) represents the timing of a hit in the LISA array. Each bar must be properly calibrated to extract the true mean time.

A cosmic ray run was used to perform this calibration. When a cosmic-ray muon travels through the LISA array and hits multiple bars, the actual time differences between the hits can be calculated from the distances between these hits and the speed of the muon. From this information, the measured time differences in different bars can be corrected by adding different offsets to every bar. The calibration procedure first finds the offset within each layer and then connects them between layers. Because cosmic-ray muons are going downward, bar 15 (top bar) was chosen as the reference for each layer, and layer 9 (front layer) bar 15 was chosen to connect with bar 0 (bottom bar) of each other layers, as depicted in Figure 4.7.

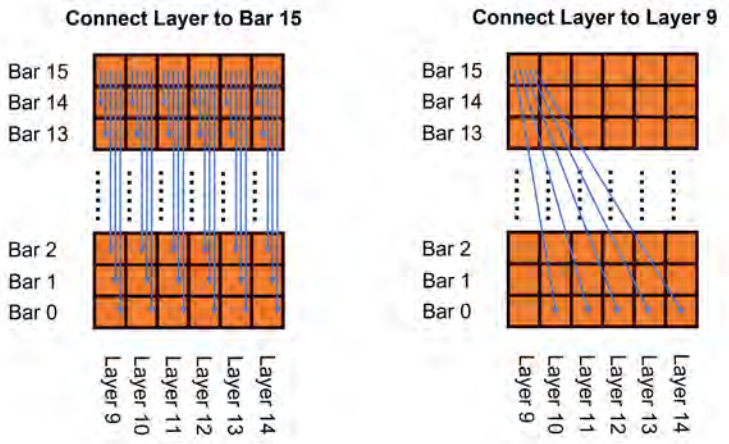

Figure 4.7: A schematic of the T_{mean} offset calibration. The blue arrows mark the steps of matching T_{mean} between the two bars with cosmic ray time-of-flight.

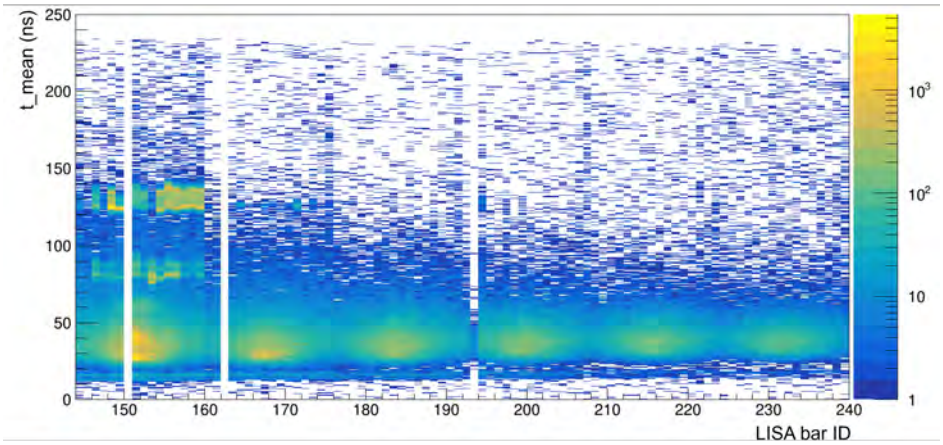

Figure 4.8: LISA calibrated T_{mean} as a function of the bar ID for data from the experiment. The bar IDs of 144 through 159 correspond to the front layer (Layer 9).

A plot of T_{mean} as a function of the bar ID is shown on Figure 4.8 for data from the experiment. The intense peak resulting from neutrons hitting the center of each layer is visible around 30-40 ns. The narrow line at ∼20 ns corresponds to γ-rays. Beam-velocity charged particles emitted from the target are visible in the front layer.

4.1.5 LISA hits spatial calibration

This calibration allows to extract the (x, y, z) coordinate of each LISA event into the beam frame where the target is at the origin (0,0,0), and the z-axis is the beam propagation axis measured from the target to the front face of the stack. The position is also corrected with the survey and geometry of the experimental setup. The center of the front face of the LISA array was found to be at $(x, y, z) = (25.1, 2.5, 449.6)$ cm. The 2D position distributions (y vs. x, z vs. x, and y vs. z) are shown in Figure 4.9.

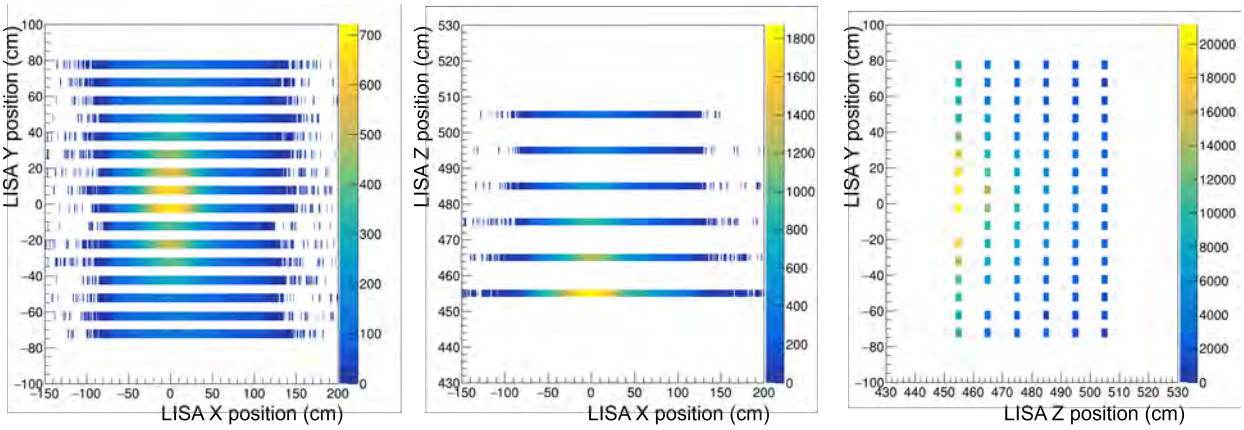

Figure 4.9: 2D position distributions in LISA: y vs. x (left panel), z vs. x (middle panel) and y vs. z (right panel).

4.1.6 LISA global timing offset

The global offset is a value added to (or subtracted from) the time of every LISA hit to set the time to zero when the beam hits the reaction target, so that the time of a LISA hit is the time-of-flight from the target. This calibration is done using the time-of-flight of the prompt γ rays originating from the reaction inside the target.

The prerequisites for the LISA global offset are correct position calibration of the array with respect to the beam axis, and correct TDC calibration and relative offsets between bars and layers. Using a subset of the experimental data with the above calibrations, for the first hit of each event, the distance d from the target to the position of the hit can easily be calculated by $d = \sqrt{x^2 + y^2 + z^2}$.

The time-of-flight for the γ-rays is $t_\gamma = \frac{d}{c}$. A shift in the time of the LISA hit by $-t_\gamma$ is applied to obtain the shifted LISA time $t_{shifted} = t - t_\gamma$. The peak of the γ ray in the $t_{shifted}$ histogram is aligned at the time that the beam hit the target. One can then fit the peak and get its mean value, which is the global offset of the LISA array. This offset (33.24 ns) needs to be subtract from every time measurement of LISA. Figure 4.10 shows

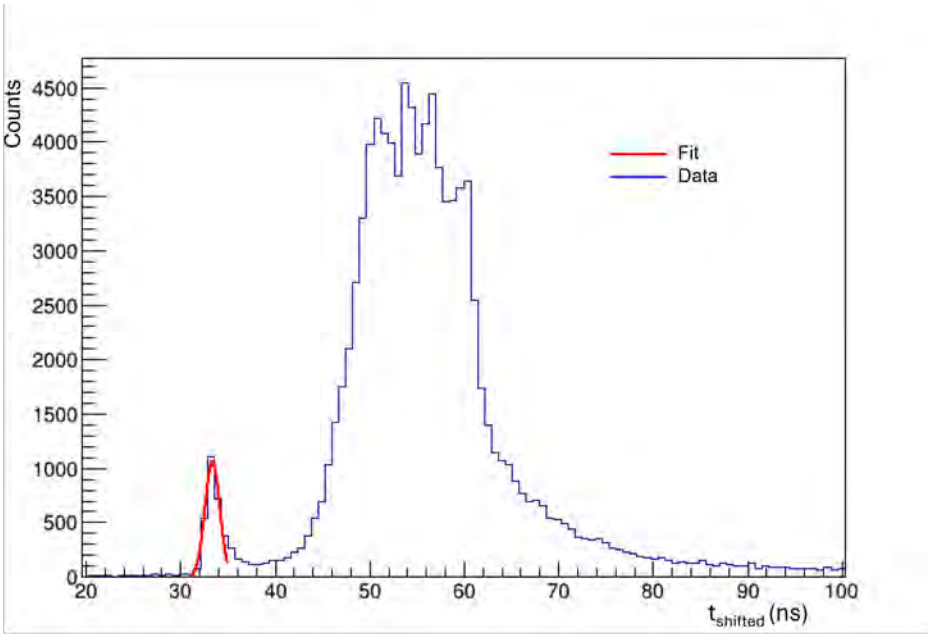

Figure 4.10: The LISA global offset fit: a Gaussian fit (red line) of the aligned gamma-ray peak is used to extract the global timing offset of the LISA array.

the histogram of $t_{shifted}$ and the fit.

4.2 Telescope calibration

The telescope, composed of 5 silicon PIN detectors and a CsI detector, provides $\Delta E - E$ particle identification (PID), that was calibrated by comparing this distribution to the calculated $\Delta E - E$ data from LISE++ [78]. The trace fitting method was utilized in the telescope calibration to improve resolution and reduce noise.

4.2.1 Particle identification (PID)

Identifying different nuclear species (i.e., A and Z) is crucial in nuclear experiments. There are multiple types of measurement related to particle identification: (1) total kinetic energy E in a stopping detector, (2) energy loss ΔE in a thin in-flight detector, (3) time-of-flight

at a certain distance, and (4) rigidity $B\rho$ in a bending magnet [79].

The secondary beam exiting the A1900 fragment separator has a certain rigidity $B\rho$ (see details in Section 3.1). The timing scintillators upstream of the reaction target measure the time-of-flight to identify secondary beam particles by velocity (see details in Section4.4.1). The ΔE and E measurements of the silicon PIN detectors and the CsI detector can further identify all different nuclides.

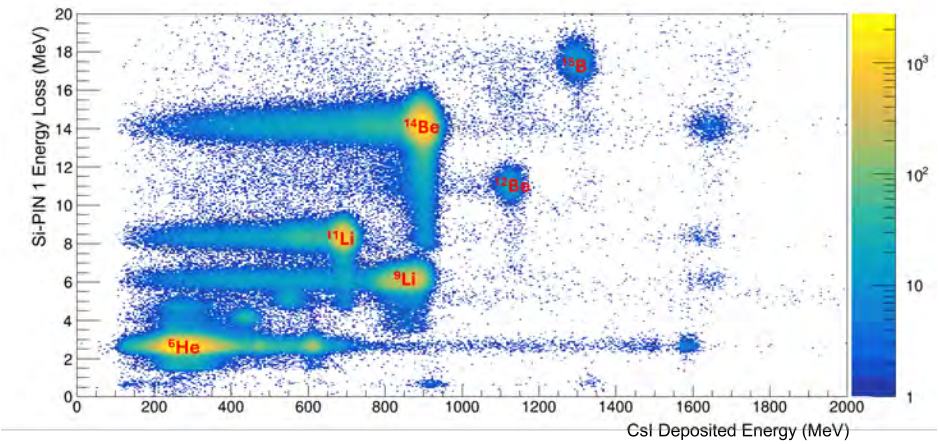

Figure 4.11: 2D plot of silicon PIN 1 energy loss versus CsI deposited energy. Identified secondary beam particles are labled on the peaks.

According to the simplified Bethe-Bloch equation [80], under non-relativistic condition ($E = mv^2/2$), in-flight energy loss rate in a thin detector can be approximately expressed as

$$\frac{dE}{dx} \propto \frac{Z^2}{v^2}. \tag{4.1}$$

At constant rigidity ($B\rho = p/q \propto Av/Z = Constant$),

$$\begin{aligned} \Delta E &\propto \frac{Z^2}{v^2} \propto A^2, \\ E &\propto Av^2 \propto \frac{Z^2}{A}. \end{aligned} \tag{4.2}$$

Therefore, different nuclides are separated in the 2-D $\Delta E - E$ plot. Figure 4.11 shows the $\Delta E - E$ PID plot obtained from the charged particle telescope.

4.2.2 Trace fitting method

The trace fitting method was utilized in the calibration of the detectors in the telescope to improve resolution and reduce noise.

The Digital Data Analysis System (DDAS) has the feature of recording the trace (pulse shape) of every signal, just like an oscilloscope does, which makes it possible to handle the signals more carefully after the experiment. A trace can be fitted to determine its start time, amplitude, whether it is valid, etc., which provides more information than the traditional amplitudes and times.

The fitting function for the traces of the silicon PIN detectors is

$$\frac{A}{1 + e^{-k_1(x-x_0)}} \cdot e^{-k_2(x-x_0)} \tag{4.3}$$

Where A is the amplitude, x is the peak position, k_1 is the rise time and k_2 is the decay time.

The CsI traces use only the logistic function part and do not have the decay time because its dacay time is far longer than the time length of the trace. The fitting function is therefore

$$\frac{A}{1 + e^{-k_1(x-x_0)}}. \tag{4.4}$$

Examples of trace fittings of the silicon PIN detectors and the CsI detector are shown in Figures 4.12 and 4.13.

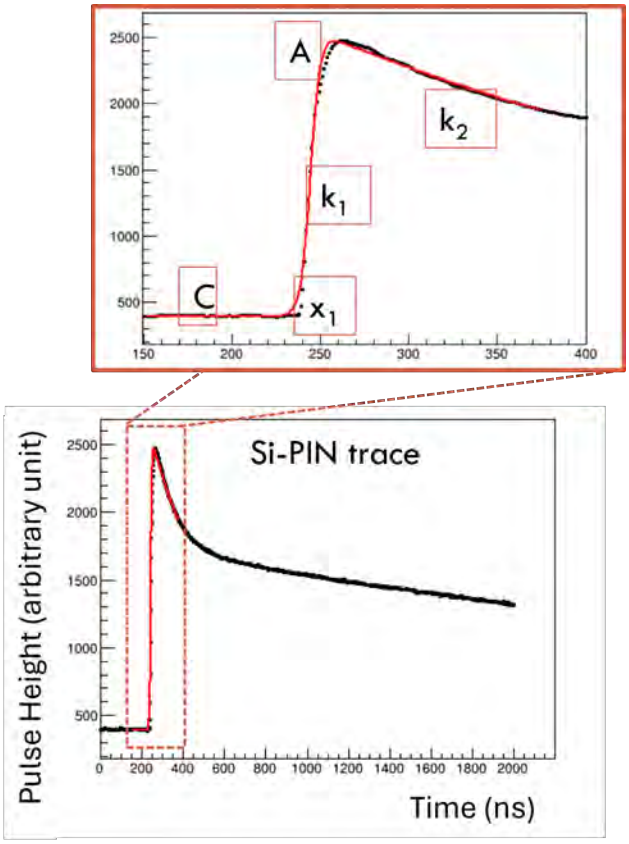

Figure 4.12: An example of the silicon PIN trace fit. The top panel is a zoom-in of the rising edge of the trace. The amplitude (A), peak position (x), rise time (k_1), and decay time (k_2) are marked in the plot.

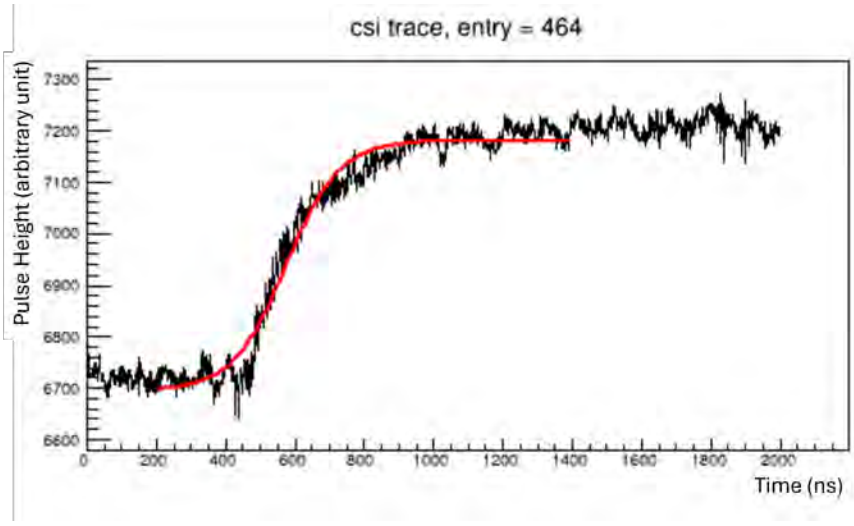

Figure 4.13: An example of the CsI trace fit.

As shown in Figure 4.14, the PID plot gets cleaner after the trace fitting. In the CsI energy deposit plot, the noise at higher energy is significantly reduced and the ^{12} Be peak appears even without requiring neutron multiplicity > 0. Gaussian fit of the ^{14}Be unreacted beam peak shows that the resolution of the CsI is 2.5% σ without the trace fitting, and improves to 2.1% σ when the trace fitting is applied.

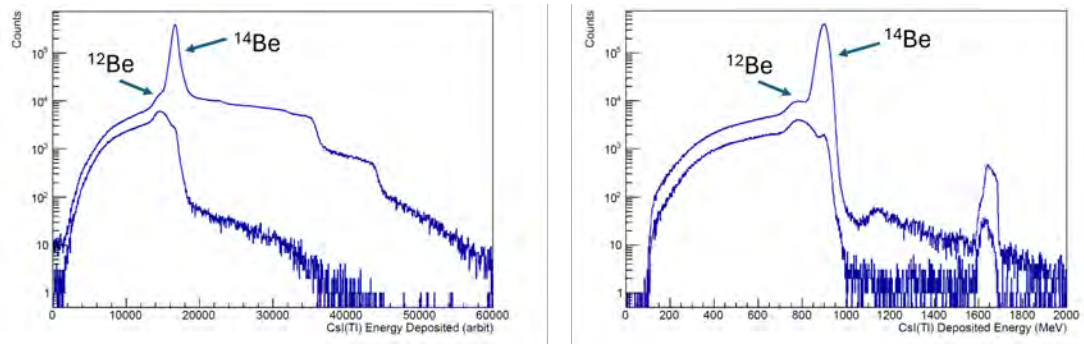

Figure 4.14: Fragment energy plots before (left) and after (right) applying the trace fitting feature: the noise (big tail on the right side of the ^{14}Be peak) is reduced, and the ^{12}Be peak can be clearly seen.

4.3 CAESAR calibration

4.3.1 Energy Calibration

Data for the energy calibration of the individual CAESAR detectors were taken with sources before and after the production runs. An ^{88}Y source was taped to the inner wall of the vacuum chamber at four different locations (top, bottom, left, and right, as depicted in Figure 4.15). Each of these runs was then analyzed to perform the calibration of all individual CEASAR detectors.

The 898 keV and 1836 keV peaks from the ^{88}Y decay as well as the 1460 keV background peak from ^{40}K are used for the CAESAR calibration. The mean value of each peak is

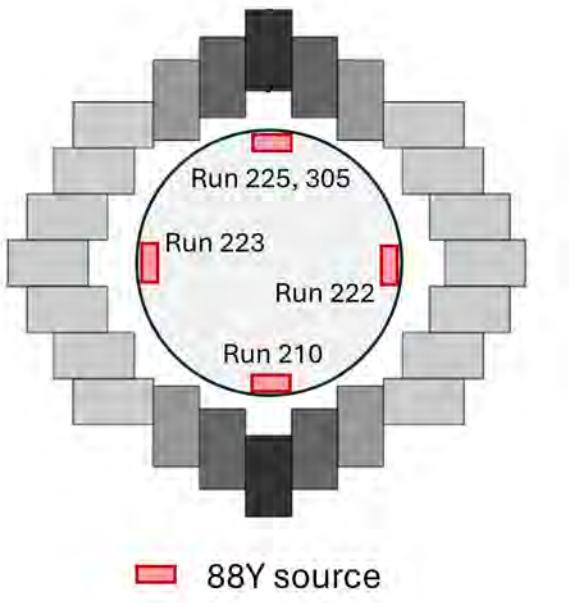

Figure 4.15: Schematic of the CAESAR calibration setup showing the four locations of the ^{88}Y source. See text for details.

extracted from a Gaussian fit and a slope and offset were extracted from a linear fit of the peak position (ADC channel) vs. γ ray energy.

CAESAR detectors at different locations were calibrated with different source runs according to the location of the source. Due to the possible gain shift over time, the 5 groups of CAESAR detector calibrated with the 5 source runs have slightly different peak positions in the γ ray energy spectra. A further correction was applied on the calibrated CAESAR data based on the 511 keV positron annihilation peak and the 1460 keV ^{40}K background peak. Figure 4.16 shows the γ ray energy spectra for the five groups of CAESAR detector before and after correction.

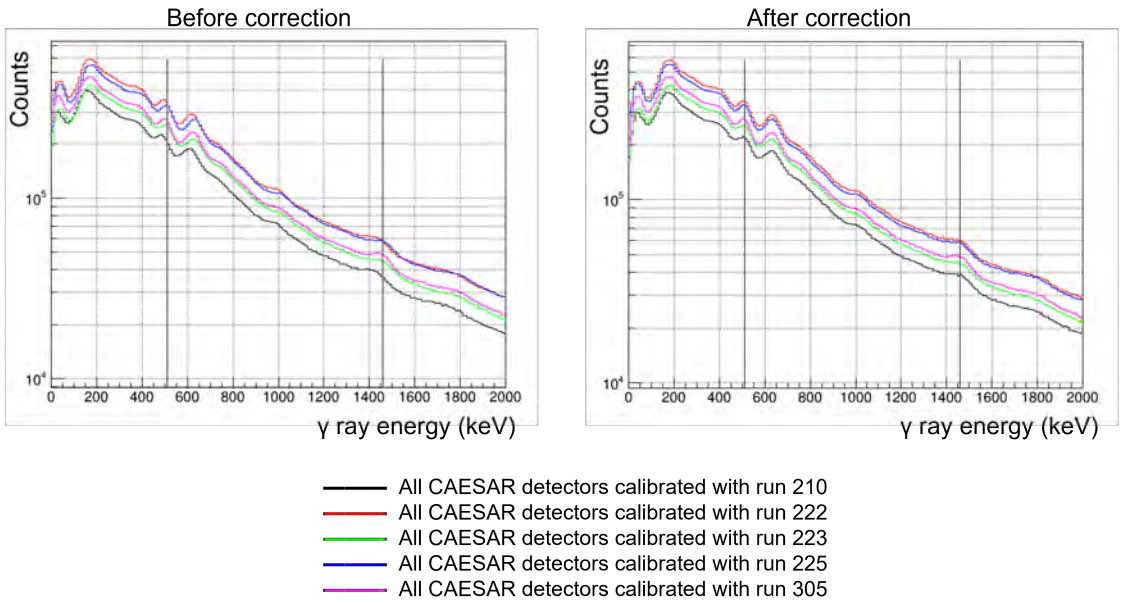

Figure 4.16: γ ray energy spectra for the five groups of CAESAR detector calibrated with different ^{88}Y source runs, before (left) and after (right) correction.

4.3.2 CAESAR time alignment

The CAESAR time represents the relative time of a CAESAR hit to the start of the event. Thirteen (13) out of the 144 CAESAR detectors had a shift in the CAESAR time over the experiment runtime. Figure 4.17 shows the CAESAR time versus experiment runtime of a typical good CAESAR detector and a CAESAR detector with a shift over time.

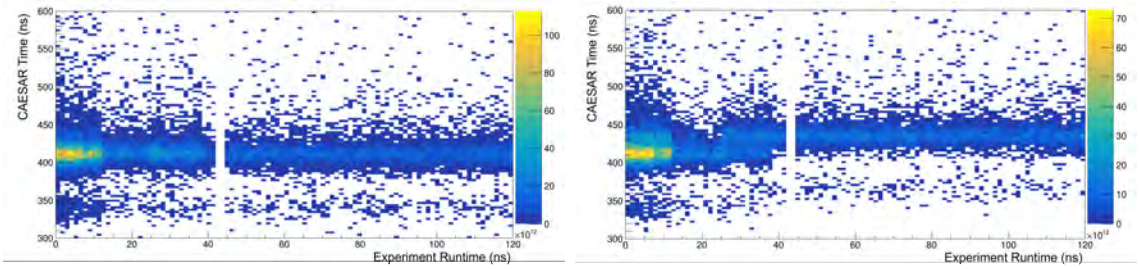

Figure 4.17: CAESAR time as a function of experiment runtime for a typical good CAESAR detector (left panel) and a CAESAR detector that have shift over time (right panel).

The 13 CAESAR detectors that shifted over time were removed from the dataset, and the CAESAR time of the other detectors was aligned by adding a different offset for each

detector. Figure 4.18 shows the CAESAR time distribution before and after alignment.

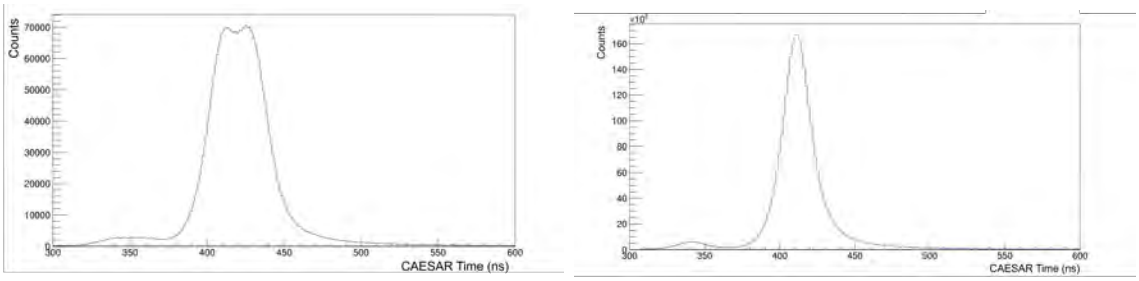

Figure 4.18: CAESAR time distribution of the whole CAESAR array before (left panel) and after (right panel) alignment.

4.3.3 Performance of the CAESAR array

The efficiency and resolution of the CAESAR detector is determined by a standalone GEANT4 simulation of the CAESAR array. The simulation includes the subset of CAESAR array used in this experiment and a CsI cuboid placed at the center of the CAESAR array to simulate the CsI detector in the telescope. A point-like, single-energy γ source is placed inside the CsI cuboid to simulate the 511 keV and 2107 keV signatures.

According to the simulation, the 2107 keV gamma ray has a full energy peak efficiency of 9.6% with a resolution of 42 keV *sigma*, and the 511 keV gamma ray has a full energy

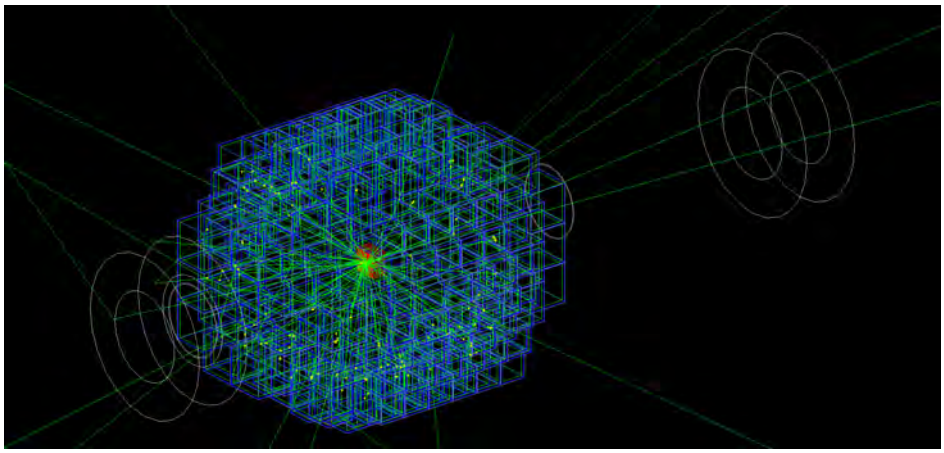

Figure 4.19: Visualization of the standalone CAESAR simulation.

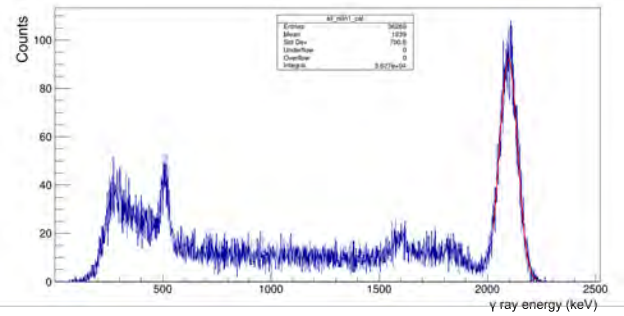

Figure 4.20: CAESAR simulation for 2100 keV γ ray.

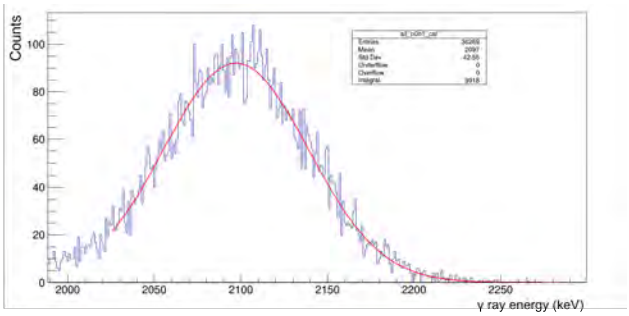

Figure 4.21: CAESAR simulation for 2100 keV γ ray, zoomed in to the full energy peak

peak efficiency of 14.4% with a resolution of 19 keV sigma. The geometric efficiency of the CAESAR array is 53% (taking account the missing and removed detectors). Thus, the efficiency to detect both 511 keV γ rays of the pair emission is $14.4\% \cdot \frac{14.4\%}{53\%} = 3.9\%$.

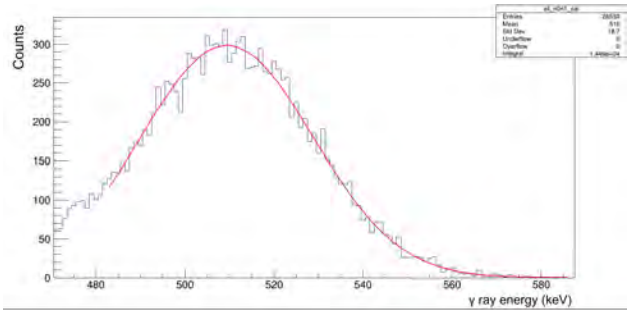

Figure 4.22: CAESAR simulation for 511 keV γ ray, zoomed in to the full energy peak

4.4 Event Selection

This section discusses the event selection methods that rule out backgrounds and keep the events of interest. Certain conditions (also called gates) are applied to the signals of the detectors to achieve that goal. Subsections 4.4.1, 4.4.2 and 4.4.3 talk about ^{14}Be beam gate, neutron gates, and fragment gates respectively.

4.4.1 ^{14}Be beam gate

The secondary beam impinging on our target contains the ^{14}Be along with other nuclides like ^{11}Li and ^{15}B. In order to select the ^{14}Be secondary beam for our experiment, a beam gate is applied on the A1900 extended focal-plane timing scintillator (ToF_xf_scint) as shown in Figure 4.23.

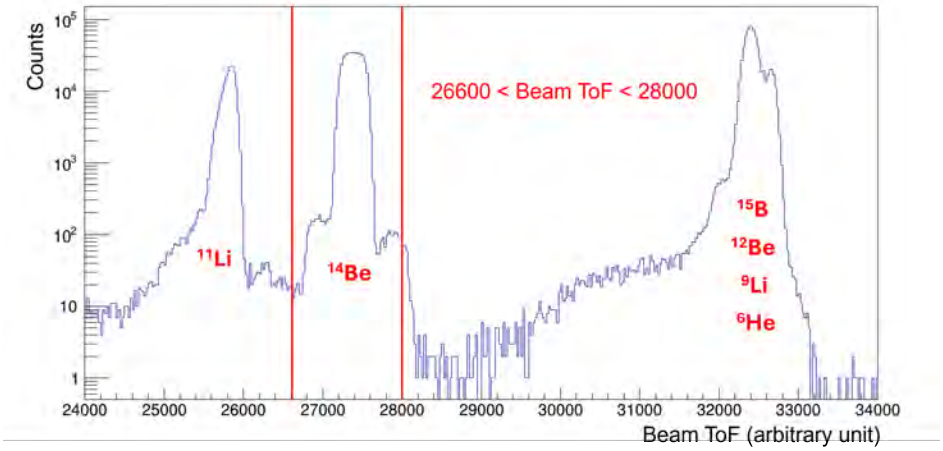

Figure 4.23: The A1900 timing scintillator gate used to select the ^{14}Be isotopes.

4.4.2 Neutron gates

Figure 4.24 shows a typical 2-D plot of the LISA light output as a function of the normalized time-of-flight (t_{norm}, see below) that corresponds to the first LISA hit. For each event, the distance (d) and time-of-flight (t) is known (see section 4.1). One can then reconstruct the

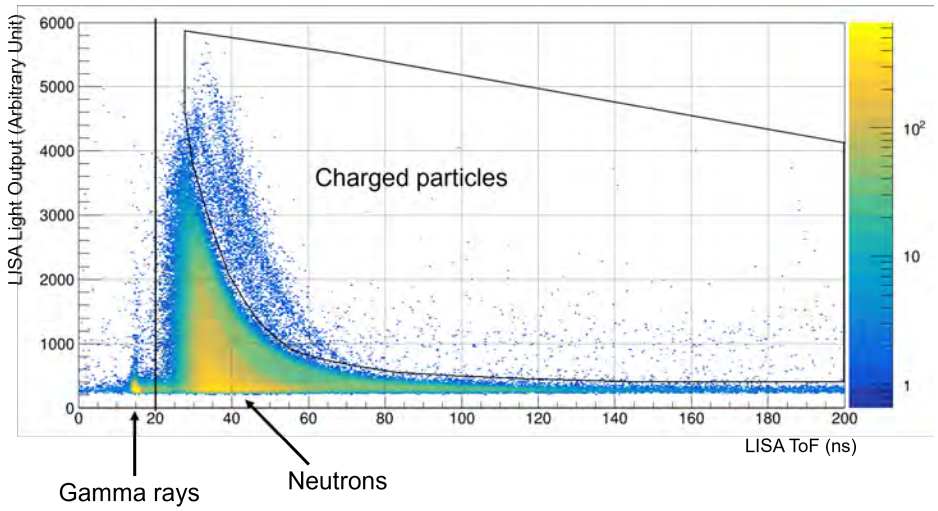

Figure 4.24: The LISA light output as a function of neutron time-of-flight. Events below 20 ns and in the charged particle region are excluded for further analysis.

corresponding velocity ($v = d/t$) of those hits. Since the distance from the target to the center of the front face of the LISA array is known ($d_0 = 454.7$ cm), we can normalize the time-of-flight of each neutron to that location as

$$t_{\text{norm}} = \frac{d_0}{d}t = \frac{d_0}{v} \tag{4.5}$$

In Figure 4.24, the prompt gamma-ray peak distribution is centered at $d_0/c = 15.2$ ns as expected. Although most of the charged particles have been ruled out by the veto detector, some of them will still reach the LISA array. The charged particles are distributed in curved bands above the neutron distribution because their mass is equal to or greater than the

neutron, and they lose all their kinetic energy in materials, while neutrons usually lose only a part of their energy when interacting with materials. So, at the same velocity, certain species of charged particles will deposit the same amount of energy in the scintillator bars, and that amount of energy is greater than the energy deposited by neutrons at the same velocity. The applied neutron gate selects events over 20 ns and not in the charged particle region.

Only the first hit in each event is analyzed, as the isotope of interest (^{13}Be) decays by emitting only one neutron. No gate on the LISA multiplicity is applied in the analysis as the detected neutron can scatter within the array multiple times, generating multiple hits. The neutron removed from the ^{14}Be beam is unlikely to reach LISA as it is transferred to the target or emitted at much lower energies with a much broader angular distribution.

4.4.3 Fragment gates

In order to select the events of interest, the ^{14}Be beam gate and the neutron gate are applied. The remaining events detected in the charged particle telescope then correspond to ^{12}Be as shown in the 2-D plot $\Delta E - E$ of the first silicon PIN detector and the CsI detector (Figure 4.25). The measured peak at silicon PIN energies of around 14 MeV and CsI energies around 800 MeV is located at the expected position (see the PID plot in 4.2.1).

^{12}Be fragments are selected by the graphical cut shown in Figure 4.25. An additional gate can be applied in a two-dimensional plot of the neutron velocity versus the CsI energy shown in Figure 4.26. The ^{12}Be events show a negative correlation, that is, the faster the fragment, the slower the neutron is. This implies energy conservation in the neutron decay and is strong evidence that the neutrons were emitted from ^{13}Be fragments or excited ^{14}Be. The vertical distribution around 940 MeV CsI energy corresponds to the unreacted

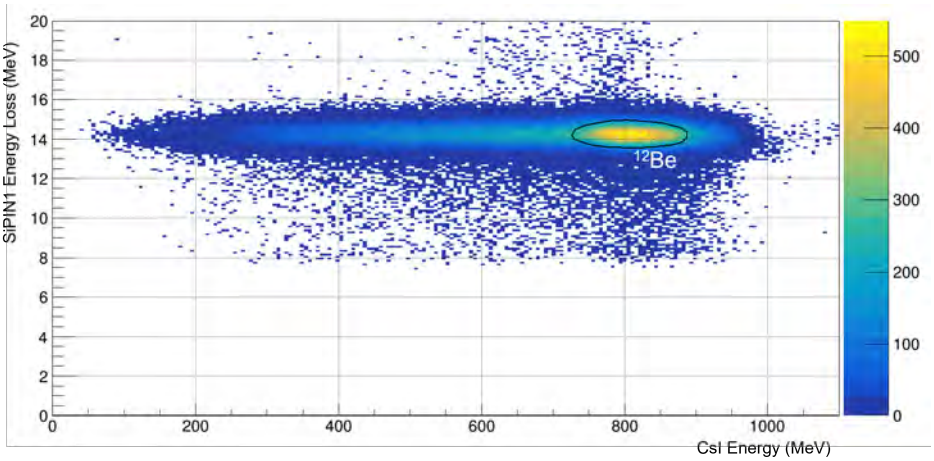

Figure 4.25: Energy Loss in Silicon PIN 1 vs CsI Energy. The black circle indicates the applied ^{12}Be gate.

beam detected in the telescope by random coincidence with backgrounds in the LISA array. The broad distribution on the left of the ^{12}Be peak corresponds to lighter Be fragments or incomplete energy deposition in CsI.

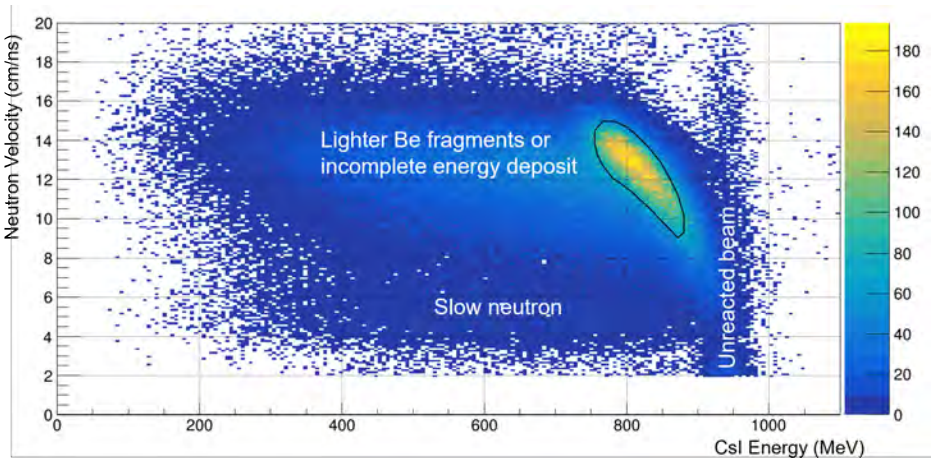

Figure 4.26: Neutron velocity versus CsI energy. The black circle indicates the applied ^{12}Be gate.

All silicon PIN detectors can be used to select valid beryllium isotopes. Two-dimensional gates were applied to silicon PIN 1 versus silicon PIN 2 (shown in Figure 4.27) and silicon PIN 4 versus silicon PIN 5 and a one-dimensional gate was applied to silicon PIN 3.

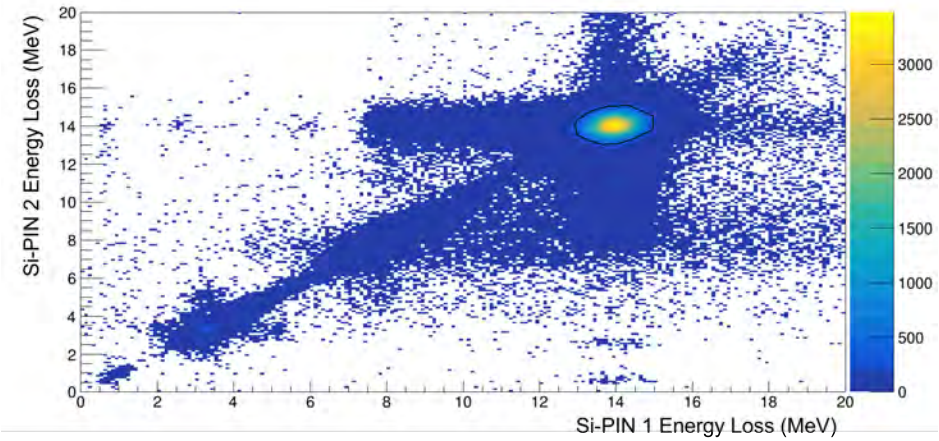

Figure 4.27: Energy loss in silicon PIN 1 vs silicon PIN 2. The black circle indicates the applied ^{12}Be gate.

4.5 Decay energy reconstruction

4.5.1 Reactions in the target

The experiment was designed to observe the reactions that occur in the target. However, reactions can also occur in the charged particle telescope. The energy reconstructions for these events will be described in the next section.

According to Section 1.5.1, the decay energy of the ^{13}Be single neutron decay can be reconstructed from the momentum vectors of the ^{12}Be fragment and the neutron.

The neutron time-of-flight and the displacement vector from the target to the LISA array are measured event-by-event for which the neutron velocity vector can be calculated as

$$\mathbf{v}_{neut} = \frac{\mathbf{d}_{target,LISA}}{t_{target,LISA}} \tag{4.6}$$

The fragment kinetic energy has to be calculated from the energy deposited along its way in any material it passes through: the target, the TLPSD and silicon PIN detectors, and the

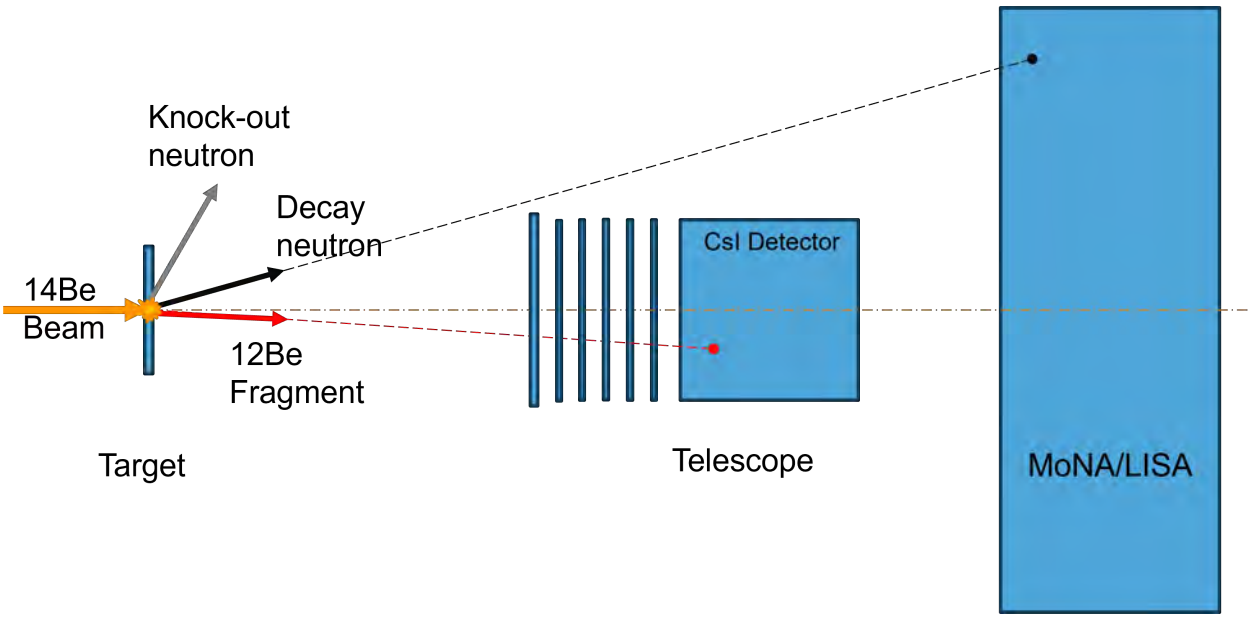

Figure 4.28: Schematics for the reconstruction of reactions in the target

CsI detector. While the energies in silicon PIN detectors and the CsI detector are measured, the energy in the TLPSD (which did not function properly) and the target are calculated with LISE++. The position of the reaction in the target is not known and is assumed to be in the middle of the target. The kinetic energy of the fragment is the sum of all these energies:

$$E_{kin,frag} = E_{target} + E_{TLPSD} + E_{siPINs} + E_{CsI} \tag{4.7}$$

The momentum vector of the fragment was supposed to be derived from the positions measurements of the 2 TLPSDs right in front of the target and the silicon PIN detectors. However, the TLPSDs did not work during the experiment (see details in 3.3). This will make the resolution of the decay energy slightly worse, but will not severely affect the validity of the decay energy reconstruction, because the angle of the fragment is much smaller than the neutron angle because of the mass ratio of the neutron and the fragment.

4.5.1.1 Transverse momentum correction

Even though it was not possible to measure the transverse momentum with the TLPSDs, an approximation was implemented.

First, it was assumed that the transverse momentum introduced by the removal of the neutron in the initial reaction ^{14}Be $\rightarrow ^{13}$Be + n is small and set to zero:

$$\begin{aligned} p_{frag,x} &= 0 \\ p_{frag,y} &= 0 \\ p_{frag,z} &= p_{frag} \end{aligned} \tag{4.8}$$

where

$$p_{frag} = \sqrt{(E_{kin,frag} + m_{frag})^2 - m_{frag}^2} \tag{4.9}$$

Then, the transverse momentum of the fragment from the decay of ^{13}Be to ^{12}Be and a neutron was set to be equal and opposite of the neutron (see figure 4.29):

$$\begin{aligned} p_{frag,x} &= -p_{neut,x} \\ p_{frag,y} &= -p_{neut,y} \\ p_{frag,z} &= \sqrt{p_{frag}^2 - p_{neut,x}^2 - p_{neut,y}^2} \end{aligned} \tag{4.10}$$

The effect of this approximation is demonstrated by simulations of the decay energy shown in Figure 4.30. The simulated data including transverse momentum distributions are shown in green. When the fragment transverse momentum is set to zero (blue) in the reconstruction, the decay energy spectrum is broadened and shifted to the left. The correct decay energy−although still broadened− is recovered (red) when the transverse momentum

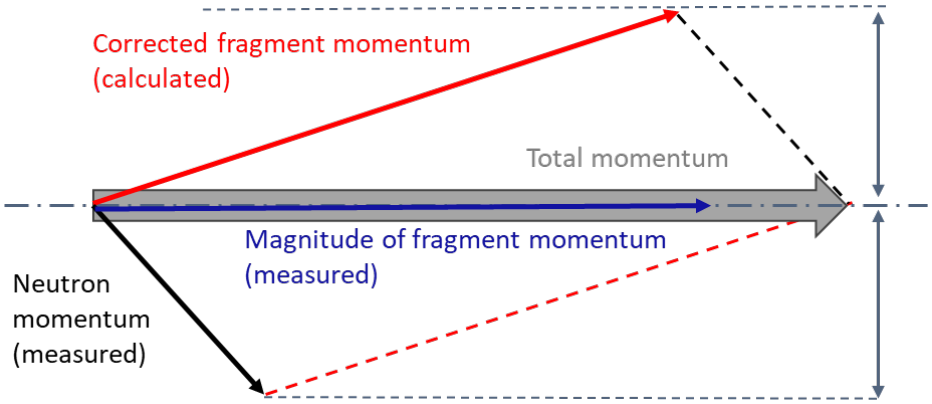

Figure 4.29: Transverse momentum schematic

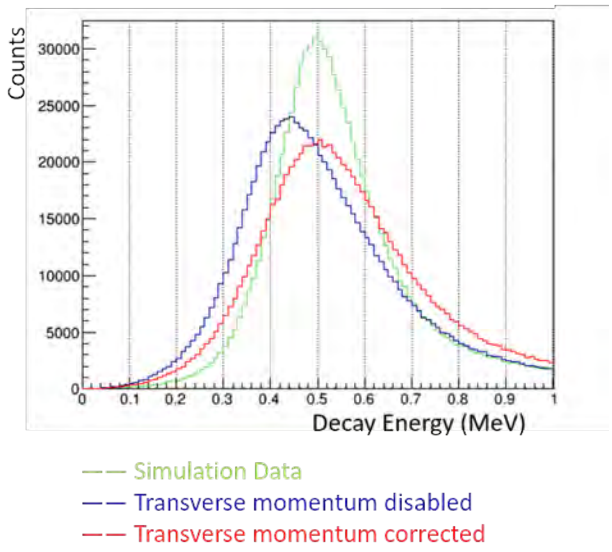

Figure 4.30: Simulation of the decay energy demonstrating the effect of transverse momentum correction.

of the fragment is calculated from the transverse momentum of the neutron as described above.

The transverse momentum correction does not always restore the true fragment transverse momentum but shifts the decay energy peak to the correct place without losing any resolution.

4.5.1.2 Relative velocity alignment

The relative velocity v_{rel} discussed in this work is defined as the difference in magnitude of the fragment ^{12}Be and the neutron velocity, instead of the vector difference.

$$v_{rel} = |v_{fragment}| - |v_{neutron}|, \tag{4.11}$$

$v_{rel} > 0$ means the decay neutron is emitted backwards, $v_{rel} < 0$ means the decay is forwards, and the distribution should be centered at 0.

The relative velocity alignment is used to add a time shift to the neutron time-of-flight so that the relative velocity peak is centered at 0.

4.5.1.3 Decay energy simulation

Due to the energy conservation in the decay from ^{13}Be to ^{12}Be and a neutron, the neutron energy and the fragment energy should add up to a constant value. The left panel of Figure 4.31 shows the results of a simulation for a 500 keV decay of ^{13}Be to ^{12}Be and a neutron following a one-neutron removal from ^{14}Be in the target, plotted as the neutron kinetic energy versus the sum of the neutron kinetic energy and the energy deposited in the CsI detector. The distribution of a vertical line shows that the total kinetic energy of the ^{12}Be + n system is a constant.

However, the data (right panel) do not agree with the simulations and show a completely different pattern. Instead of a vertical line, the experimental data still show a negative correlation between the neutron energy and the sum of the CsI and neutron energies. In addition, it has a wider range of neutron kinetic energy, from 100 MeV all the way to 0, while the simulation ranges only from 60 and 90 MeV. The observation of slower neutrons in

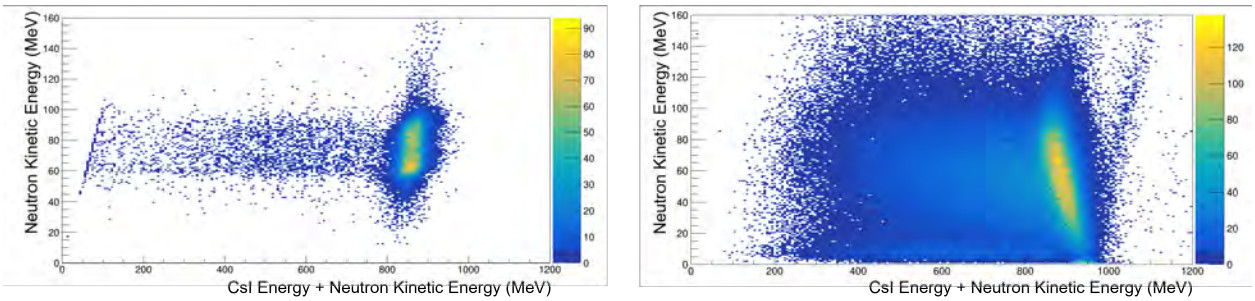

Simulation, reaction in target

Experiment

Figure 4.31: Neutron kinetic energy versus the sum of the CsI and neutron energy from simulation (left) and data (right).

the data indicates reactions of beam particles in the charged particle telescope as they are slowing down and stopped in the CsI detector.

4.5.2 Determination of Reaction Location

As mentioned earlier, the reaction of interest is a two-step process: a one-neutron removal from ^{14}Be followed by one-neutron decay of ^{13}Be.

The neutron removal of ^{14}Be can be considered as a peripheral reaction where the ^{13}Be pre-fragment continues at approximately the same velocity as the ^{14}Be beam. Therefore, the total kinetic energy is reduced by the kinetic energy of a neutron with the velocity of the beam.

The subsequent neutron decay of ^{13}Be occurs essentially immediately within the target (10^{-21} s) so that the ^{12}Be + n system has the same center-of-mass velocity before and after decay.

According to the assumptions above, the velocity of the ^{12}Be fragment is the same as the beam particle at the reaction point, as well as the decay neutron. However, any state in ^{13}Be is above the neutron emission threshold. So, the available decay energy is shared between

the ^{12}Be fragment and the neutron increasing or decreasing the velocities depending on the emission angle.

It should be mentioned that other reactions can also occur, for example, two-neutron removal, two-neutron decay after Coulomb excitation, and even dineutron emission.

The differences between reactions in the target and in the charged particle telescope are demonstrated in Figures 4.32 and 4.33.

The in coming ^{14}Be beam particles have a kinetic energy of 76 MeV/u with a 2% spread. This kinetic energy is deposited in the target and all the detectors before and after the reaction, and is also carried away by the 2 neutrons emitted in the reaction.

In the case of reactions within the target, the kinetic energy of the beam particle ranges from 76 MeV/u to 72 MeV/u depending on the position of the reaction within the target, as shown on the left side of 4.32.

In the center-of-mass frame of the ^{12}Be + n system, the neutron can be emitted in any direction in the space. Forward decay and backward decay are the two extreme cases in which the neutron is emitted in the same or opposite direction of the center-of-mass velocity, respectively. The right panel of figure 4.32 shows the example for a decay energy of 0.5 MeV in the middle of the target. A forward decay neutron gets the maximum lab frame kinetic energy of around 90 MeV, while a backward decay neutron gets the minimum of 60 MeV. This $\pm$15 MeV or $\pm$20% difference in the neutron kinetic energy due to decay is much larger than the effect of different reaction positions in the target. This spread of neutron energies is also shown in the 2-D kinematic plot of the simulation shown on the right side of Figure 4.31.

In the case of reactions in the CsI detector, where the beam stops, the beam energy at the front face of the CsI detector is 67 MeV/u. The reaction can happen at any beam energy

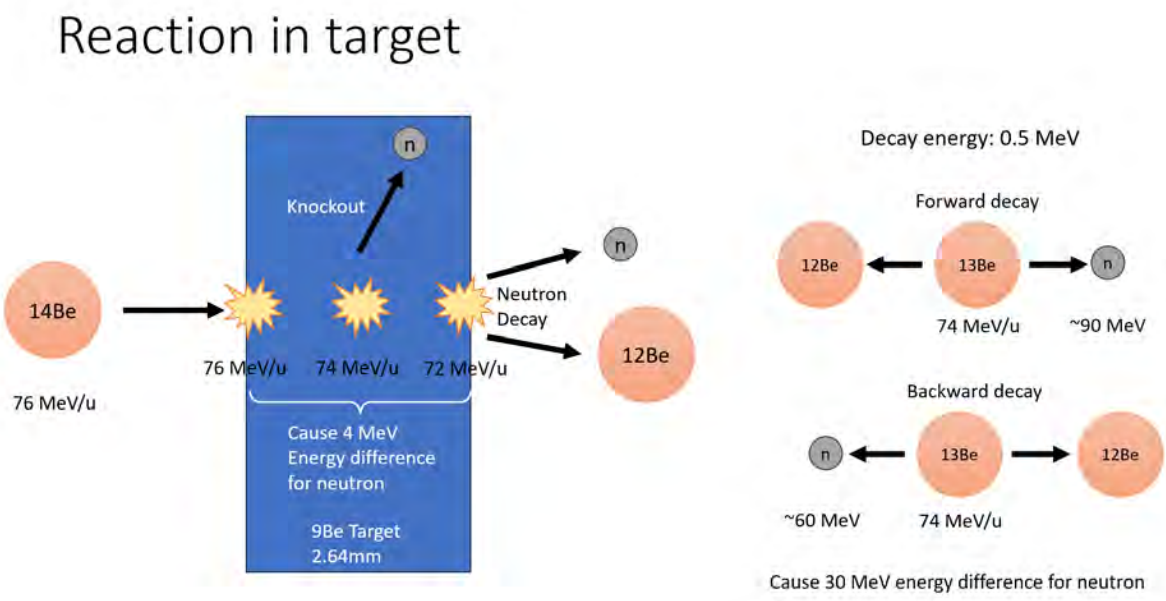

Figure 4.32: Schematic of a reaction in the target.

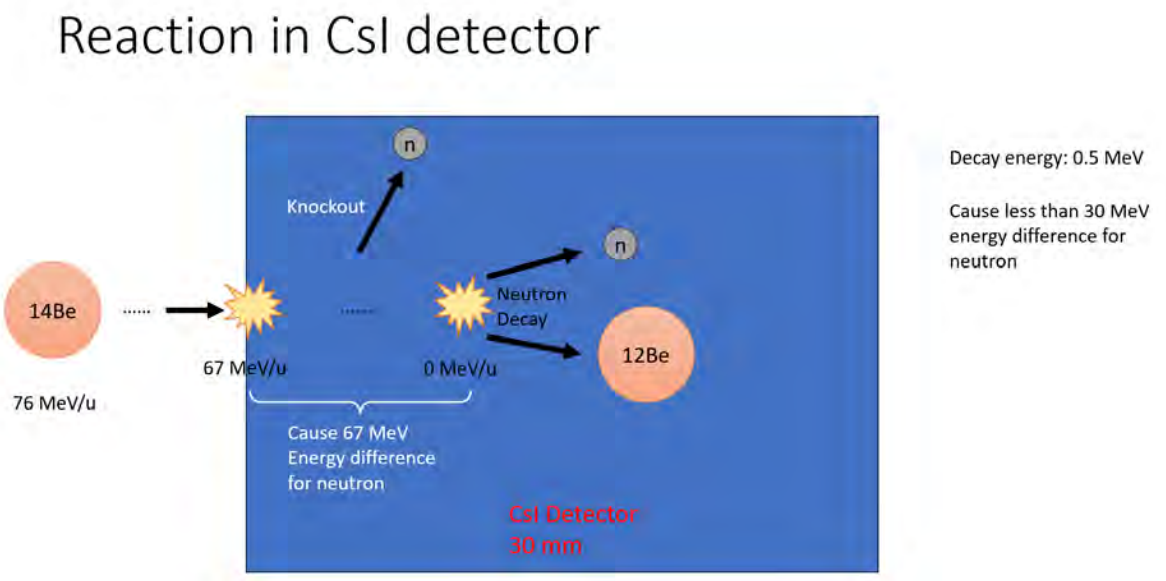

Figure 4.33: Schematic of a reaction in the CsI detector.

from 67 MeV/u all the way to 0 as shown in figure 4.33. The energy difference between the forward and backward decay neutrons is less than 27 MeV/u, decreasing with decreasing energies in the reaction. So, the reaction position or the beam energy in reaction is the dominant influence factor of the outgoing kinetic energy of the neutron and fragment.

If the reaction occurs in the CsI detector the measured energy includes not only the fragment kinetic energy, but also the energy deposited by the beam particle before the reaction. In other words, the energy deposited in the CsI detector is the total kinetic energy of the ^{14}Be beam particle minus the kinetic energy carried away by the removed and emitted neutrons. Each of these two neutrons carry away approximately the same amount of kinetic energy corresponding to the beam velocity at the reaction. So, the energy deposited in the CsI detector plus twice the detected neutron kinetic energy is a constant. This explains the negative slope in the 2D plot of the neutron energy versus the sum of the CsI plus one neutron shown in Figure 4.31.

Figure 4.34 shows the neutron kinetic energy versus the sum of the CsI energy plus twice the neutron energy. The top row shows the results of simulations for reactions in the target and the CsI on the left and right, respectively. The sum of the two simulations (bottom left) resembles the experimental data (bottom right). This qualitatively demonstrates that the experimental data contain both reactions in the target as well as in the CsI. The neutron kinetic energy of reactions in the target and CsI have a large overlap from 60 to 80 MeV. So, it is hard to clearly separate the two reaction locations.

4.5.3 Reactions in CsI

For reactions in the CsI, the energy deposited in the detector does not represent the fragment kinetic energy as mentioned in the previous section. So, the standard method described in

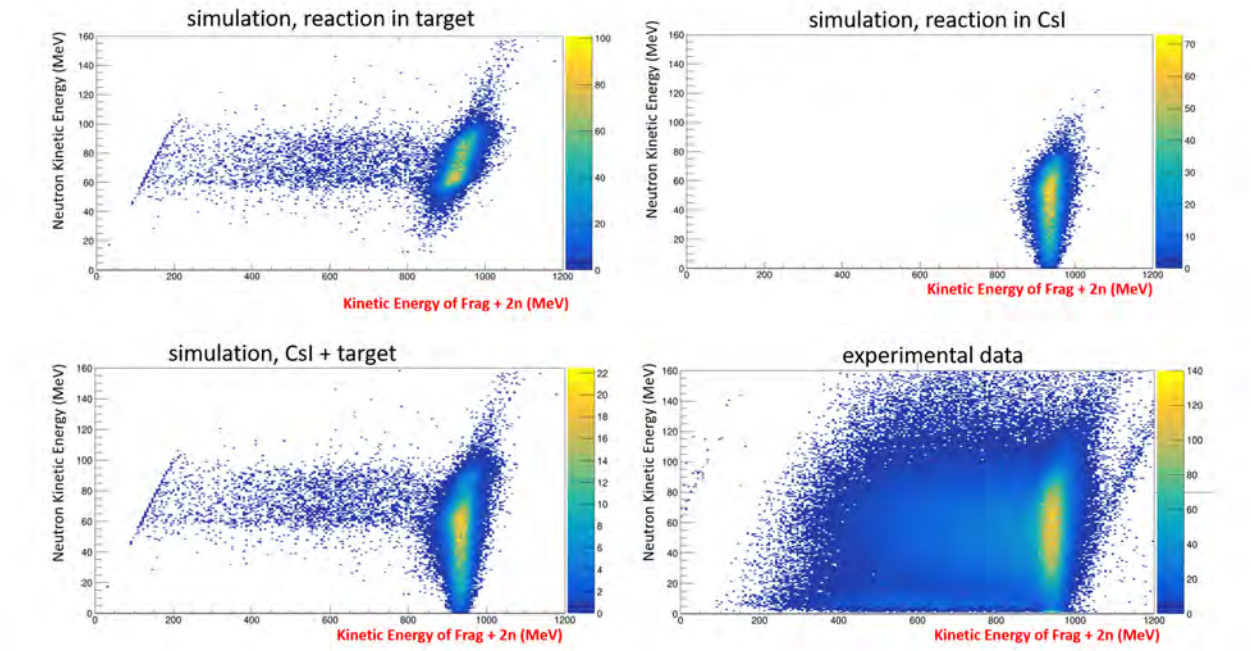

Figure 4.34: Neutron kinetic energy versus the sum of the CsI energy plus twice the neutron energy. The top row shows the results of simulations for reactions in the target and the CsI on the left and right, respectively. In the bottom row the sum of the two simulations (left) are compared to the experimental data (right).

Section 4.5.1 is not applicable.

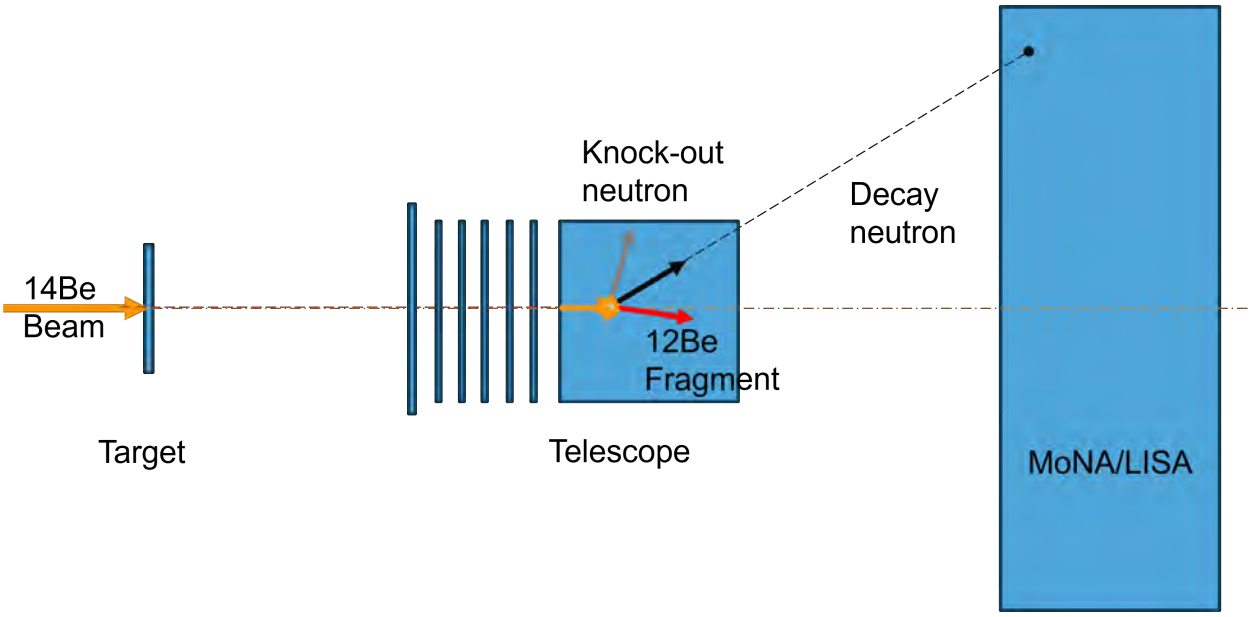

Figure 4.35: Reconstruction for reactions in the CsI.

However, it is still possible to approximate the fragment energy as well as the neutron velocity which are necessary to reconstruct the decay energy (see Section 1.5.1). According to section 4.5.2, the unreacted beam enters the CsI detector at 67 MeV/u and its total kinetic energy is deposited in the detector or carried away by the 2 neutrons. With the assumptions described in the previous section, the ratio between the energy carried away by the neutrons and the fragment energy corresponds approximately to the ratio of their mass. Thus, the fragment kinetic energy can be expressed as

$$E_{kin,frag} = \frac{m_{12Be}}{m_{14Be} - m_{12Be}} \cdot (E_{CsI,14Be} - E_{CsI}) \tag{4.12}$$

The drawback of this model is that the approximation of fragment velocity equals to beam velocity is assuming that the decay energy is zero, which means that this model has no sensitivity to the decay energy on the fragment side. However, this introduces only a small uncertainty, as the decay energy is mostly carried away by the neutron.

The calculation of the neutron velocity is also slightly different. The starting point of the displacement should be moved to the CsI detector. The thickness of CsI is 3 cm, and the beam stops at a depth of about 1.3 cm. The starting point is chosen at the stop point of the beam.

The start point of the neutron time-of-flight also needs to be moved to the CsI detector. The time-of-flight of the ^{14}Be beam from the target to the CsI detector (about 12 ns) needs to be subtracted from the measured neutron time-of-flight:

$$\mathbf{v}_{neut} = \frac{\mathbf{d}_{CsI,MoNA}}{t_{target,MoNA} - t_{target,CsI}} \tag{4.13}$$

Reconstruction for reaction in silicon detectors is similar to the one for reaction in the beryllium target, because they are both in-flight reactions.

4.5.4 Reaction type

In case there are reaction types other than one neutron knockout followed by one neutron decay, simulations for different reaction types are performed and compared to the experimental data. The other possible reaction types are two-neutron decay and dineutron decay.

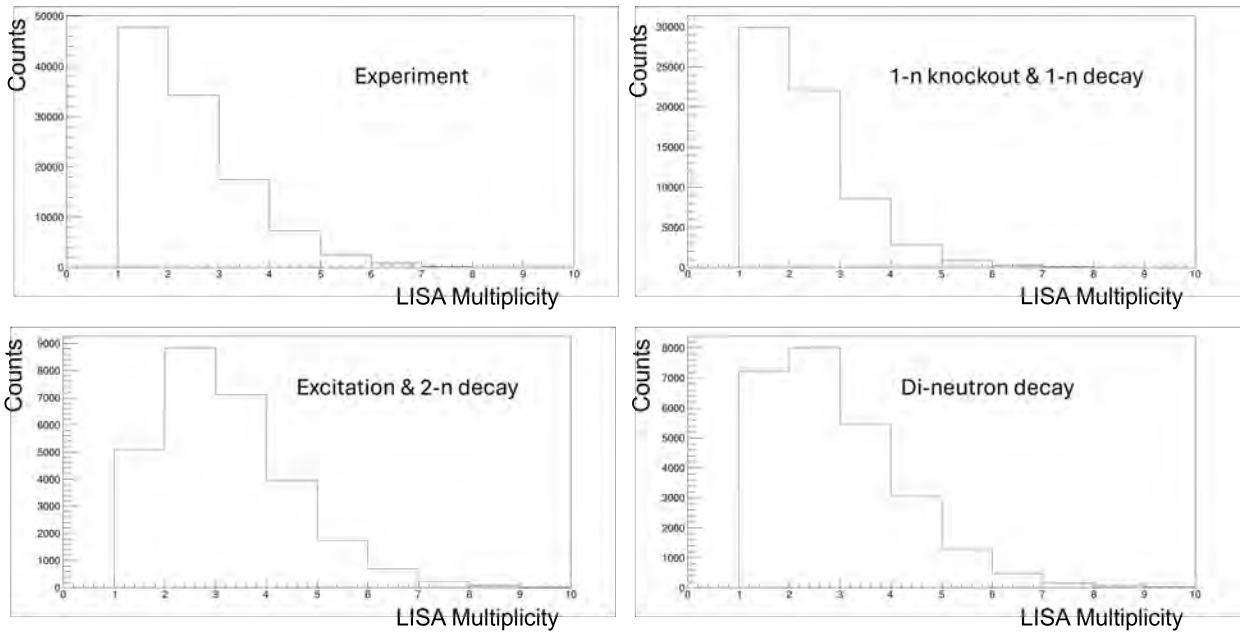

Figure 4.36: Neutron multiplicity plots for the experimental data (top left), one-neutron knockout and one-neutron decay (top right), Excitation and two-neutron decay (bottom left), di-neutron decay (bottom right).

Figure 4.36 shows the neutron multiplicity plots of different reaction types. The neutron multiplicity distribution shows that the one-neutron decay reaction is the dominant one, since its distribution looks almost identical to the experimental distribution, and they both peak at 1, while the other 2 reaction types peak at 2. The proportions of other reaction types are negligible. So, they will not be considered in further data analysis.

4.6 CAESAR spectra analysis

The detection of γ rays in coincidence with the fragments is an essential part of the experiment. The γ ray spectra from the CAESAR array in coincidence with the 0.5 MeV p-wave neutron decay is key to determining which state in ^{12}Be is the final state of the neutron decay. As discussed in section 1.5.3, the signatures of populating the 0_2^+ isomeric state are 511 keV and 2.1 MeV γ rays.

Due to the relatively long lifetime (331 ns mean lifetime) of the isomeric state, the emission rate of these γ depends on the time after the population of the state and should be distinguishable from prompt γ. Thus, the timing properties of the γ rays detected in CAESAR are studied as well as the energy.

The 511 keV γ rays are emitted in pairs from the annihilation of the positron from the E_0 decay of the ^{12}Be isomeric state. These two 511 keV photons are emitted at the same time and in the opposite direction. The detection of two correlated 511 keV γ rays in opposite detectors is a useful signature to identify this decay.

For γ-rays above about 1 MeV Compton scattering becomes a dominant process for their interaction with matter. In the Compton scattering process, a photon deposits only a fraction which depends on the scattering angle. Thus, one γ-ray can interact multiple times. If these interactions occur in different detectors of CAESAR an algorithm called "CAESAR addback" can identify such events and recover the full energy of the γ ray. This algorithm is helpful in extracting the signature of the 2.1 MeV γ ray.

4.6.1 CAESAR energy and time

Figure 4.37 shows the 2-D plot of CAESAR time versus CAESAR energy. The CAESAR corresponds to the time difference between an interaction CAESAR and the A1900 extended focal plane scintillator. Promptly emitted γ rays appear at approximately 410 ns and delayed γ rays should appear at greater CAESAR time. Some energy peaks can be seen around 50 keV, 200 keV, 400 keV, 511 keV, and 600 keV. There is no apparent peak at about 2100 keV.

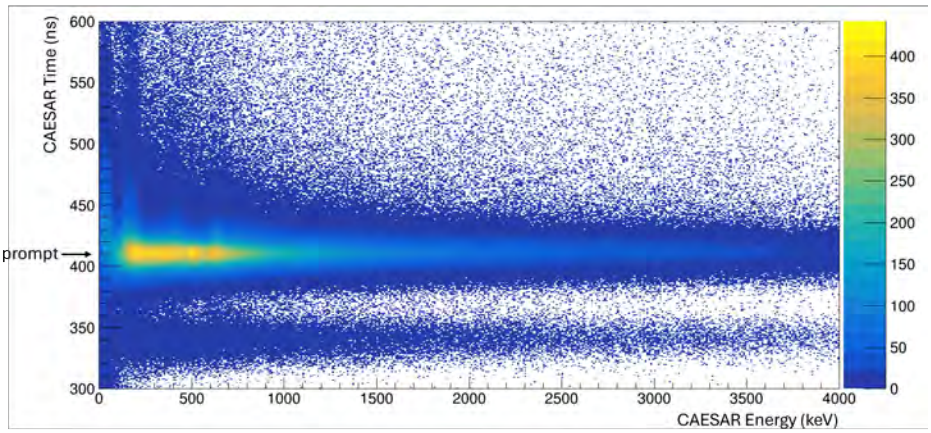

Figure 4.37: CAESAR time versus gamma ray energy.

If there is a delayed γ ray signal, there should be a long upward tail at its energy, which means that the decay time of the peak is longer. To look more closely at the decay time, projections on time using slices around the energy peaks can be useful.

Figure 4.38 shows the CAESAR time spectra of energy slices around the peaks and also around 2.1 MeV because that is where the signature is expected. Only the peak below 100 keV has a relatively longer decay time. The other energy slices have roughly the same decay time and are likely to be prompt γ rays.

Although there is no obvious evidence for delayed γ rays, a more detailed analysis is

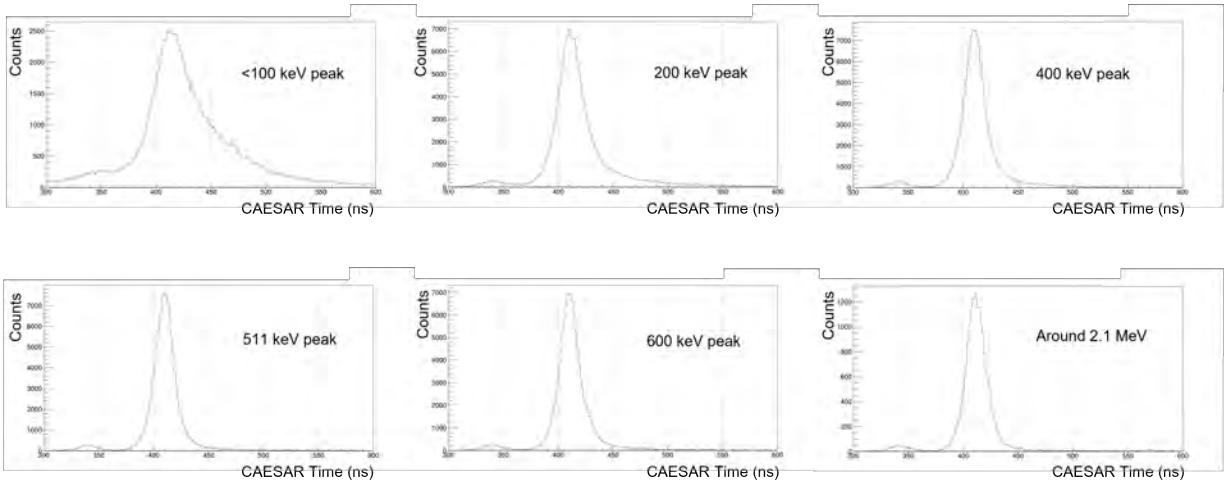

Figure 4.38: CAESAR time plots around the peaks in the energy spectrum.

necessary to rule out the population of the isomeric state.

4.6.2 CAESAR geometric correlations

The subset of the CAESAR array utilized in this experiment has 6 rings from c to h (2 to 7), and each ring has 24 detectors, from 0 to 23. As shown in figure 4.39, if interactions in ring m_1 and ring m_2 satisfy

$$m_1 + m_2 = 9 \tag{4.14}$$

they occur in opposite rings. If in addition the interactions trigger in detectors n_1 and n_2 which satisfy

$$n_1 - n_2 \equiv 12 \pmod{24} \tag{4.15}$$

they occurred in opposite directions in the CAESAR array.

The correlations between two γ rays can be seen in a 2-D plot of their energies, as shown on the left side of Figure 4.40. The data on the top are gated on γ rays emitted in opposite directions, where a peak at 511 keV is visible (signal plot). The plot is symmetric with

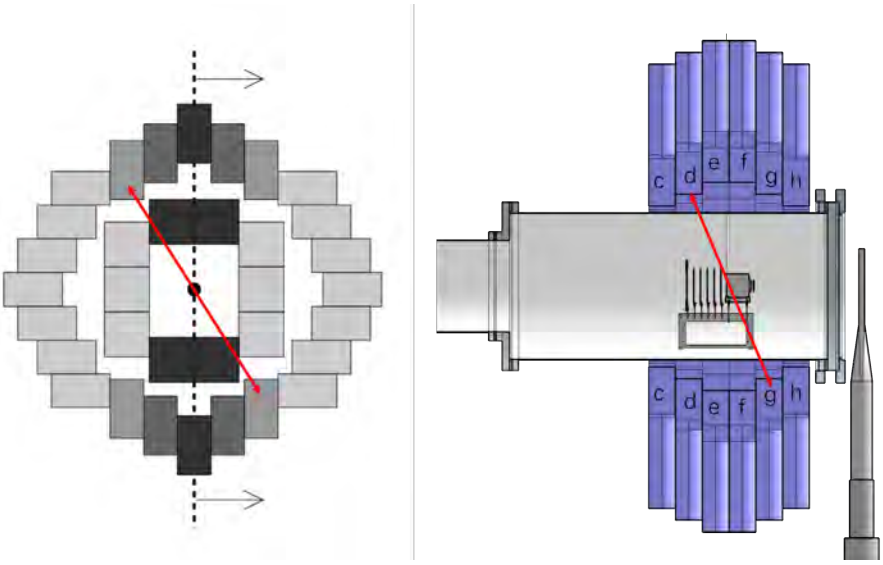

Figure 4.39: Schematic of CAESAR geometry. The red arrows indicate γ rays interacting in opposite detectors.

respect to the diagonal because each opposite detector pair or hit pair was counted twice, with the x and y values swapped.

In order to enhance true coincidences and to eliminate background events, events where two gγ rays were emitted perpendicular to each other were selected. For a photon in detector of ring m_1 and detector n_1, its "90-degree" detector is defined as the detector of ring m_2 and detector n_2 that satisfies

$$\begin{aligned} |m_1 - m_2| &= 3 \\ n_1 - n_2 &\equiv 6 \pmod{24} \end{aligned} \tag{4.16}$$

The energy correlation gate by the "90-degree" events (background plot) is shown on the middle panel on the left side of Figure 4.40. The background plot was normalized to the signal plot and subtracted from it. The plot after subtraction is shown on the bottom left. The (511 keV, 511 keV) peak is the only pronounced peak in the 0 to 1000 keV range, clearly indicating the decay of a 511 keV γ ray pair.

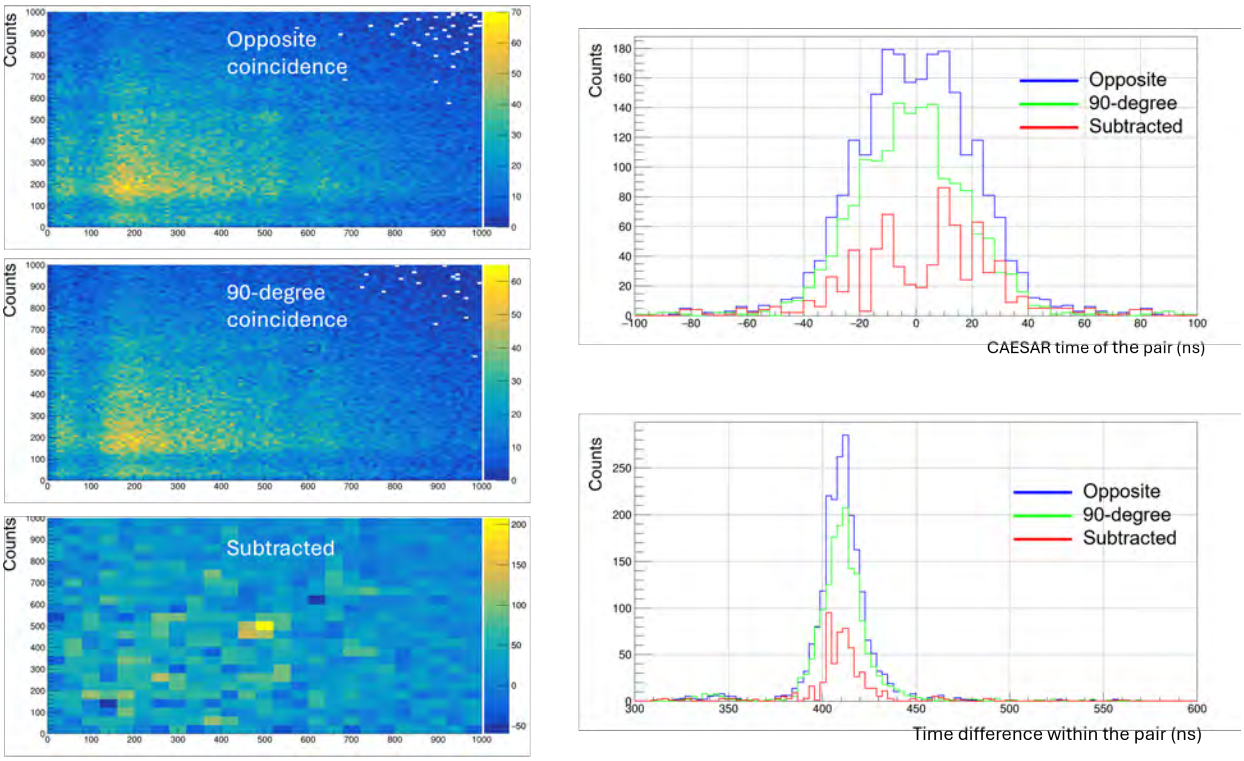

Figure 4.40: Left panels: Energy correlation plots of two coincident γ-rays detected in CAESAR. The top panel is gated on γ rays emitted in opposite directions, the middle panel is gated on γ rays emitted perpendicular to each other, and the bottom panel shows the difference spectrum. Right panels: The time difference (top) and the time (bottom) of the corresponding events from the left panel.

The two plots on the right side of 4.40 show the timing properties of the 511 keV γ ray pair. The signal, background, and the subtracted data are shown in blue, green, and red, respectively. The time difference within the pair has a distribution around 0 ns with a FWHM of about 20 ns as shown on the top. This corresponds to the time resolution of CAESAR and thus are emitted at the same time. The CAESAR time of one of the two photons shown on the bottom displays a narrow peak around 410 ns corresponding to the prompt γ rays. If the pair would have been submitted from the isomeric state in ^{12}Be, the timing distribution exhibit a long tail on the right side of the distribution.

In summary, the analysis of the 511 keV gamma ray on CAESAR data alone shows no evidence of delayed emission. Correlation with the neutron dacay measurement and further

gating is needed to draw a conclusion (see Section 5.2).

4.6.3 CAESAR Addback

In order to improve the search for the 2.1 MeV γ ray, a new CAESAR addback algorithm was developed which recovers Compton scattering events where not the full γ ray energy was deposited in one detector.

While an addback routine is included in the original CAESAR analysis code it can only handle events with 4 hits or less. In the present experiment, the event building time window is as long as 3 μs, resulting in a significant number of events with more than 4 hits, as shown in Figure 4.41.

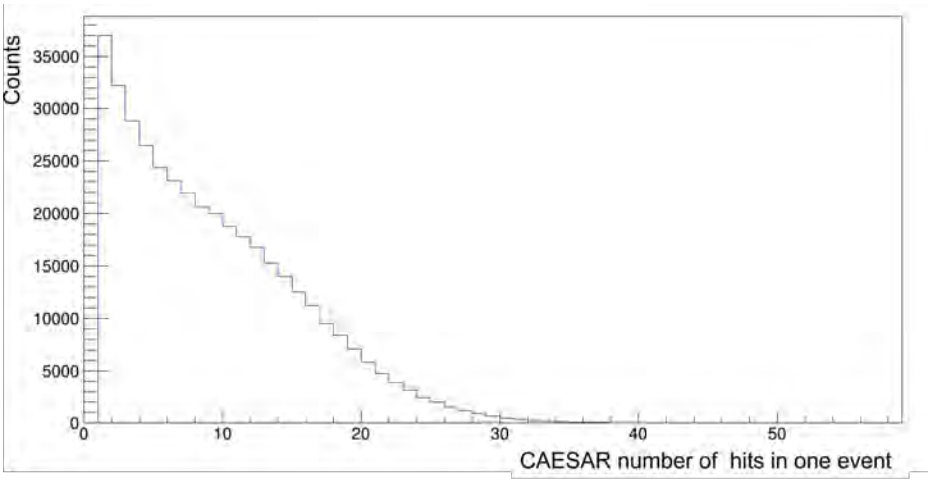

Figure 4.41: Number of CAESAR detectors triggered in a single event.

The new CAESAR addback algorithm defines clusters of hits. If two hits are in neighboring detectors and their time difference is smaller than a certain value (50 ns), then they are combined into a cluster.

Figure 4.42 is a map of the CAESAR detectors. The eight detectors around a detector on the map are defined as its neighboring detectors. It should be noted that because the

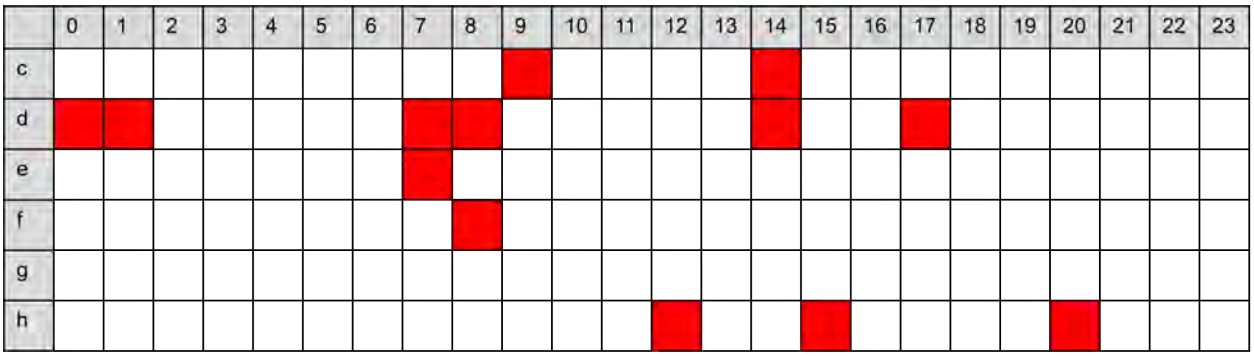

Figure 4.42: Map of rings and detectors of CAESAR. The red squares show the detectors triggered in a sample event.

detectors are arranged in rings, detectors in column 0 have neighbors in column 23, and vice versa. The red filled cells mark the hits in a sample event. The 13 hits in this event are combined into 7 clusters.

There can be more than one hit on the same detector in one event. Recording no more than one hit on one detector will only lose about 1% of hits, but will significantly simplify the analysis process. So, in the actual data analysis, no more than one hit is kept in each detector for each event.

Each cluster is reconstructed as one γ ray, its energy is defined as the sum of energy of all hits in the cluster, and the time and position (which detector) are defined to be the same as the hit with the highest energy in the cluster.

Figure 4.43 is the histogram of the number of CAESAR hits in one cluster. More than 95% of the clusters have no more than 3 hits. Clusters of too many hits are not trustworthy. In further analysis on the CAESAR spectrum, gates can be applied to accept only clusters with no more than 3 or 2 hits.

The effect of the addback is shown in Figure 4.44 for data taken with a ^{88}Y source. The blue and red curves correspond to the data before and after addback, respectively. The 898 keV and 1836 keV peaks from the decay of ^{88} Y and the 1460 keV background peak from

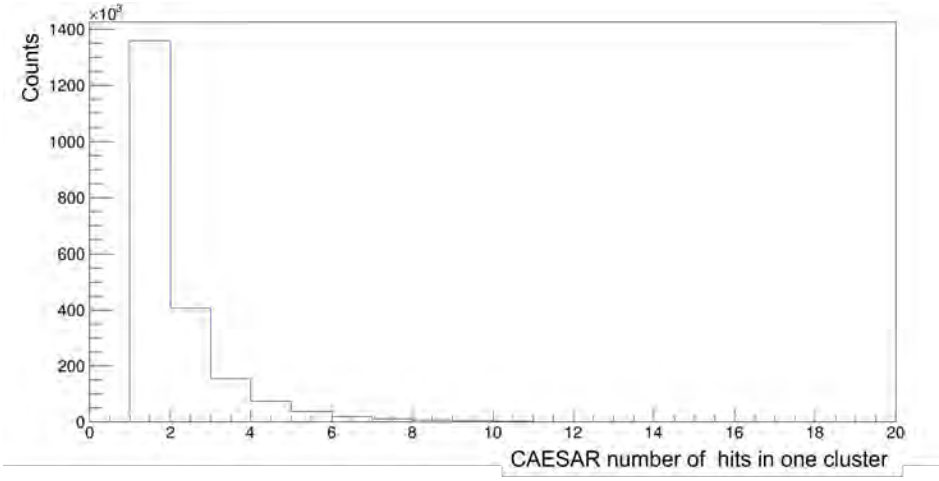

Figure 4.43: Number of CAESAR hits in one cluster.

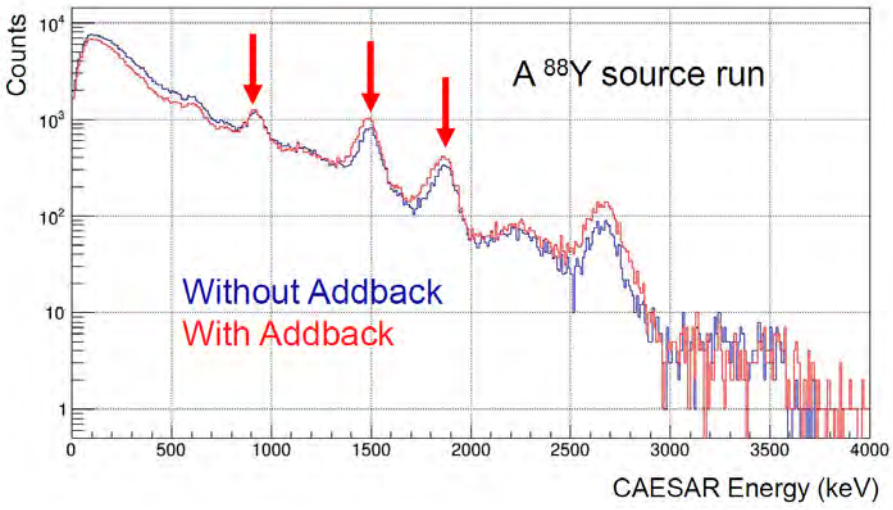

Figure 4.44: CAESAR spectrum from a ^{88}Y source, before (blue) and after addback (red).

^{40}K are used for CAESAR calibration, and the 2734 keV peak from ^{88}Y is also visible in the spectrum. The three higher energy peaks are enhanced after the addback is applied, and the 898 keV peak does not change. This is reasonable because Compton scattering is not that preferable for a γ ray with an energy of less than 1 MeV.

Figure 4.45 shows the addback effect on the experimental data. After addback, the lower energy part ($<$ 1.5 MeV) is diminished and the higher energy part enhanced, however, no specific peaks become apparent. Further gating (for example on the decay energy) is needed

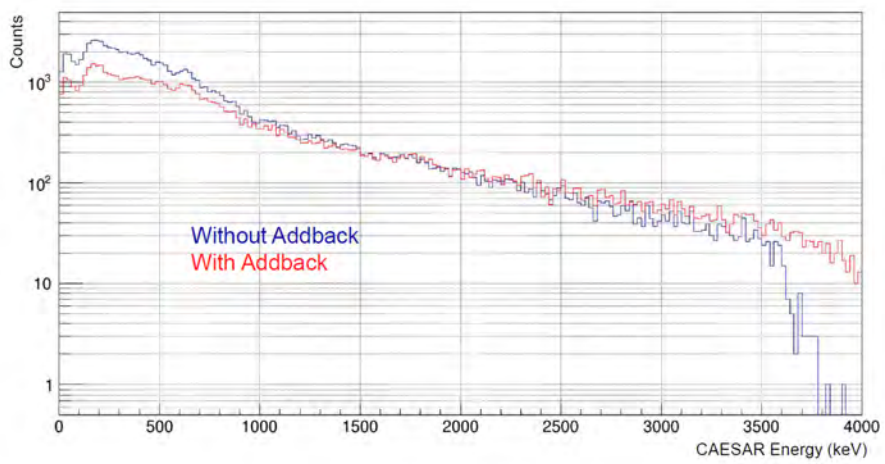

Figure 4.45: The CAESAR spectrum of experimental data (production run), before (blue) and after addback (red).

to search for the 2.1 MeV γ ray (see Section 5.2).

4.7 Simulations

Monte Carlo simulation plays an important role in data analysis. In the previous sections simulations have been used to interpret some of the observables measured in the reaction. To extract the relative contributions of reactions in the target and the CsI detector as well as the cross-section of each resonance, especially the p-wave resonance, simulations are used to fit the experimental data.

Simulations of different parts of the experimental setup are performed separately. The reaction process is simulated using ST_MoNA, an in-house C++ based simulation package. The outgoing neutron information is sent to N2_GEANT, a simulation based on GEANT4 dedicated to neutron interactions in the LISA array. The fragment information from ST_MoNA is sent to a stand-alone GEANT4 simulation for the interactions in the charged particle telescope. Different reaction locations are also simulated with variants of these simulation

components. This section will focus on the details of the simulations.

4.7.1 ST_MoNA and N2_GEANT

ST_MoNA models the beam, the reaction target, and the interaction of the beam within the target. N2_GEANT models the interaction of neutrons with the LISA array. The performance of these simulation codes has been bench marked in previous studies.

The incoming beam profile is modeled by Gaussian distributions for the x and y positions and angles. The kinetic energy of the beam is modeled by a uniform distribution with a centroid and a width. The target is parameterized by its Z, A, and thickness.

Table 4.1 shows the beam and target parameters used in the ST_MoNA simulation.

Table 4.1: Beam and target parameters

Parameter	Value	Description
eBeam	76.5	Beam energy (MeV/u)
dEbeam	1.4%	Half width of energy distribution (relative)
beamA	14	Beam A
beamZ	4	Beam Z
targA	9	Target A
targZ	4	Target Z
dTarget	486	Target thickness (mg/cm^2)
monaDist	454.65	Distance from target to MoNA (middle of the first layer)
bSpotCx	0	Beam spot x centroid (m)
bSpotCtx	0	Beam spot θ_x centroid (rad)
bSpotCy	0	Beam spot y centroid (m)
bSpotCty	0	Beam spot θ_y centroid (rad)
bSpotDx	0.0023	Beam spot x width (σ) (m)
bSpotDtx	0.014	Beam spot θ_x width (σ) (rad)
bSpotDy	0.0020	Beam spot y width (σ) (m)
bSpotDty	0.010	Beam spot θ_y width (σ) (rad)

As the beam or fragment (after the reaction) propagates through the target, the energy loss and straggling are taken into account. The reaction position along the thickness of the target is randomly chosen with a uniform distribution. The dynamics of the one-neutron knockout of ^{14}Be is modeled in the Glauber formalism, one neutron is removed, and a

momentum kick is applied to the remaining ^{13}Be. The subsequent one-neutron decay is modeled by the resonant line-shape.

The output ROOT file of ST_MoNA includes the momentum information of the outgoing fragment and neutron from the target. The neutron information of every event is listed in a file and sent into N2_GEANT, which simulates the neutron interaction in LISA. The neutron interactions with hydrogen and carbon nuclei that make up the LISA scintillator bars are modeled using the MENATE_R database. This simulation is able to reproduce the efficiency and timing and position resolution of the LISA detectors.

The fragment information is sent to a standalone GEANT4 simulation for the telescope.

4.7.2 Standalone GEANT4 simulation for the telescope

A stand-alone Geant4 simulation reads the momentum information of the outgoing charged fragments from the target and uses it as the "beam". This simulation includes the TLPSD2, five siPINs, and the CsI detector. The electromagnetic and hadron physics lists used for the interactions in the detectors.

The measured values (energy loss in each siPIN and in CsI) are written in a text file. Those information, as well as the response of the LISA array generated by N2_GEANT, will be merged into the root tree created by ST_Mona. The physics reconstruction will then be done in the same manner as the reconstruction for the experimental data.

4.7.3 Reaction parameters

For the neutron decay, the decay energies and widths of the expected resonances as listed in Table 4.2 were taken from reference [44, 58].

These parameters were fixed because of the low resolution of the experiment so that the only free parameters were the cross-sections of these resonances.

Table 4.2: Angular momenta, energies E (MeV), and widths Γ (MeV) of the simulated resonances.

Angular momentum	Energy E (MeV)	Width Γ (MeV)
l=0 (s)	0.81	2.1
l=1 (p)	0.45	0.45
l=2 (d)	2.0	2.0

4.7.4 Simulation for different reaction locations

In addition to reactions in the target, simulations were also performed for reactions in the CsI and silicon detectors, as it was not possible to clearly separate them in the data. By fitting the different contributions to the data, the cross-section of the p-wave neutron decay can be determined.

For reactions in the CsI the beam and target parameters in ST_MoNA are modified. The CsI detector is regarded as the "target" and the unreacted beam at the entrance of the CsI detector is the "beam". Table 4.3 shows the modified parameters.

The ^{12}Be fragment stops in the CsI detector, so there is no outgoing fragment information that can be sent into a standalone simulation. The outgoing neutron momentum information is sent to N2_GEANT. The output files of N2_GEANT and ST_MoNA are then merged and reconstructed into physical quantities such as the decay energy.

Table 4.3: Beam and target parameters for reactions in CsI detectors

Parameter	Value	Description
eBeam	66.7	Beam energy at entrance of CsI (MeV/u)
dEbeam	1.58%	Half width of energy distribution (relative)
beamA	14	Beam A
beamZ	4	Beam Z
targA	130	Effective A of CsI
targZ	54	Effective Z of CsI
dTarget	13530	Thickness of CsI (mg/cm^2)
monaDist	314.72	Distance from target to MoNA (middle of the first layer)
bSpotCx	0	Beam spot x centroid (m)
bSpotCtx	0	Beam spot θ_x centroid (rad)
bSpotCy	0	Beam spot y centroid (m)
bSpotCty	0	Beam spot θ_y centroid (rad)
bSpotDx	0.0034	Beam spot x width (σ) (m)
bSpotDtx	0.017	Beam spot θ_x width (σ) (rad)
bSpotDy	0.0025	Beam spot y width (σ) (m)
bSpotDty	0.013	Beam spot θ_y width (σ) (rad)

For the simulation of reactions in silicon detectors, the process is similar to that in the standard target case. The TLPSD2 and the five silicon PIN detectors are simplified as a single silicon target, and the beam and target parameters are modified accordingly. A stand-alone GEANT4 simulation is needed to handle the reactions of the outgoing fragment in the

CsI detector. Table 4.4 shows the beam and target parameters for reactions in the silicon detectors.

Table 4.4: Beam and target parameters for reactions in silicon detectors

Parameter	Value	Description
eBeam	72.0	Beam energy at entrance of TLPSD2 (MeV/u)
dEbeam	1.4%	Half width of energy distribution (relative)
beamA	14	Beam A
beamZ	4	Beam Z
targA	28	A of Silicon
targZ	14	Z of Silicon
dTarget	615	Thickness of silicon detectors added up (mg/cm^2)
monaDist	321.95	Distance from TLPSD2 to MoNA (middle of the first layer)
bSpotCx	0	Beam spot x centroid (m)
bSpotCtx	0	Beam spot θ_x centroid (rad)
bSpotCy	0	Beam spot y centroid (m)
bSpotCty	0	Beam spot θ_y centroid (rad)
bSpotDx	0.0023	Beam spot x width (σ) (m)
bSpotDtx	0.014	Beam spot θ_x width (σ) (rad)
bSpotDy	0.0020	Beam spot y width (σ) (m)
bSpotDty	0.010	Beam spot θ_y width (σ) (rad)

4.7.5 Fitting of the experimental data

The purpose of fitting the experimental data is to extract the contribution of the p-wave neutron decay of ^{13}Be. Based on the extracted number of counts of the p-wave decay, the expected γ-ray counts assuming a population of the isomeric state can be estimated. Comparing these counts with the measured γ-ray counts is possible to determine if the p-wave neutron decays to the isomeric state of ^{12}Be.

As described in Subsection 4.7.3, the experimental data is fit with three resonances. In addition, an uncorrelated background, which is a flat distribution of decay energy from 0 to 20 MeV is included in the simulation. Simulations for each of these four components is performed for the three different reaction locations: target, silicon detectors, and the CsI detector. The results of these twelve simulations were used to fit the ^{12}Be + n decay energy spectrum and the relative velocity spectrum (difference of the velocity scalars) of the ^{12}Be fragment and neutron.

The same reconstruction method and event selection gates were applied to the simulations and the data. The reconstruction method for reaction in the beryllium target is used for extracting the decay energy because it is the designed reaction location of the experiment and has the best resolution of the decay energy.

The final kinematic 2-D gate is shown in the overlap with the experimental data in Figure 4.46, and in the overlap with the fitting components in figure 4.47. The 2-D kinematic gate includes almost all valid events in the experimental data and also covers a major part of all the fitting components.

The fitting is carried out using a code developed by Thomas Redpath. The code uses a χ^2 minimizing algorithm. The decay energy and decay width of the resonances are fixed

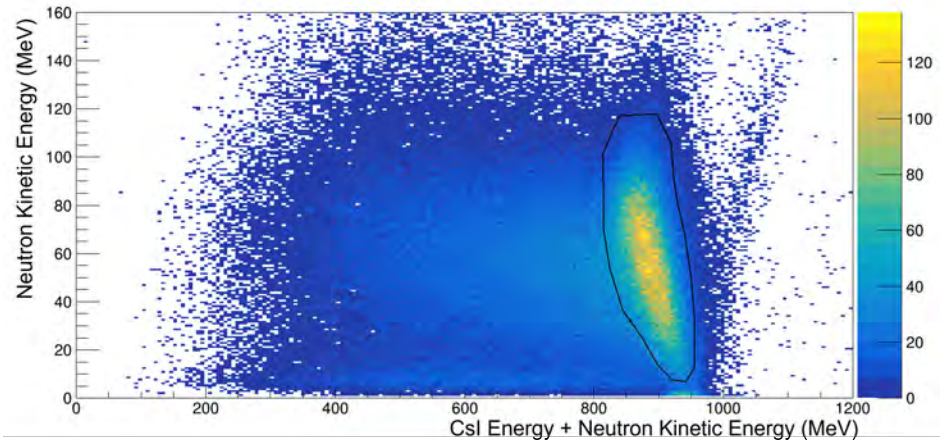

Figure 4.46: The final 2-D gate (marked in black).

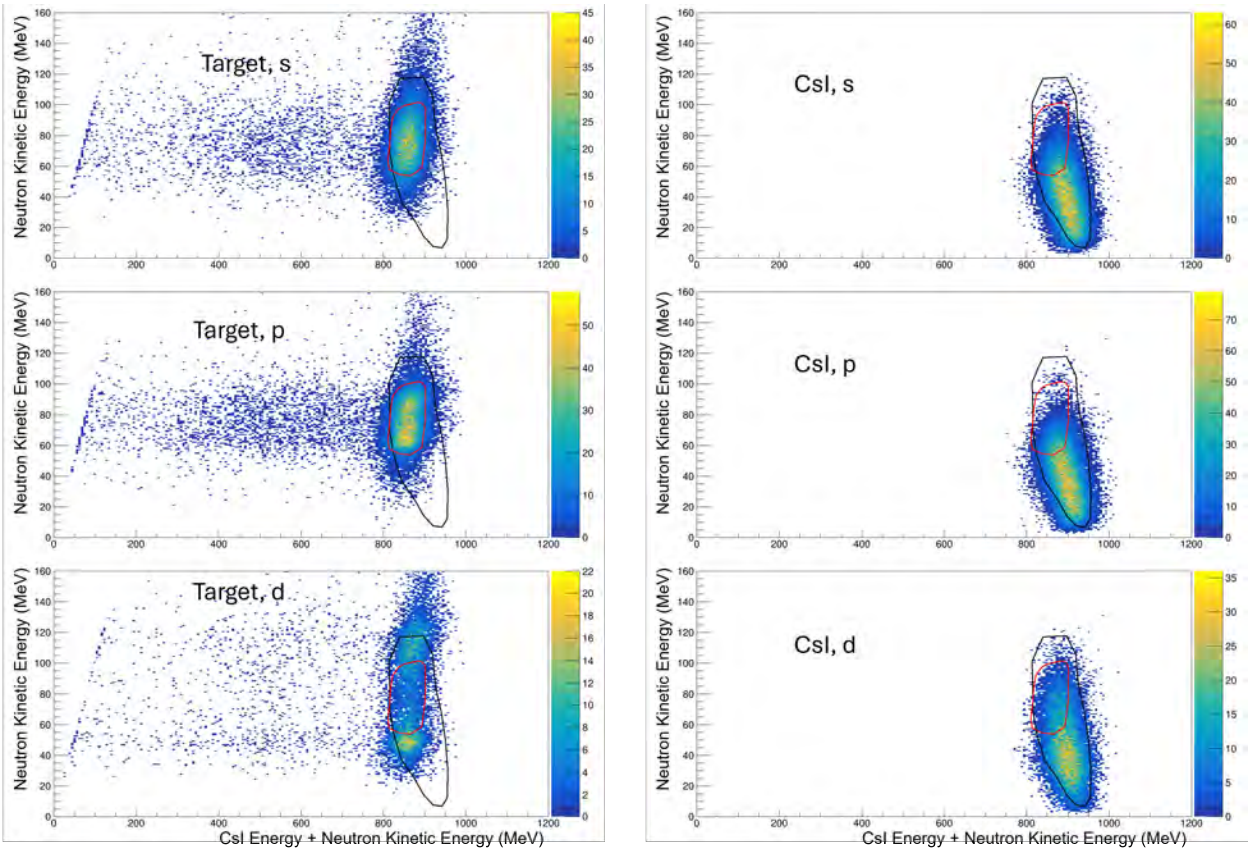

Figure 4.47: Comparing the final 2D gate (marked in black) and the target p-wave gate (marked in red) with the simulations.

values obtained from existing experiments. The free parameters in the fit are just the cross-sections of each resonance at each reaction location. The ratio between the cross-sections of the beryllium target and the silicon detectors is fixed according to theory calculations, because (1) reactions in the target and silicon detectors are both in-flight reactions in a thin target, and the rates can be calculated based on theoretical cross-sections, (2) fixing the ratio can reduce the amount of fitting parameters from 12 to 8 and simplify the fitting process.

The total simulation S_{total} can be expressed as

$$\begin{aligned} S_{total} =& P_1(S_{s,target} + C_1 \cdot S_{s,Si}) \\ &+ P_2(S_{p,target} + C_2 \cdot S_{p,Si}) \\ &+ P_3(S_{d,target} + C_3 \cdot S_{d,Si}) \\ &+ P_4(S_{flat,target} + C_4 \cdot S_{flat,Si}) \\ &+ P_5 \cdot S_{s,CsI} \\ &+ P_6 \cdot S_{p,CsI} \\ &+ P_7 \cdot S_{d,CsI} \\ &+ P_8 \cdot S_{flat,CsI}, \end{aligned} \tag{4.17}$$

where $P_1 ... P_8$ are the fitting parameters, $S_{s,target}$ is the simulation of s-wave decay that occurs in the beryllium target, other simulation components are expressed in the same logic, and "flat" represents a flat distribution that simulates the uncorrelated background, $C_1 ... C4$ are constant coefficients that fix the ratio between reactions in the target and silicon detectors. The result of $C_1 ... C_4$ is shown in Section 5.1.

4.8 Efficiency and resolution

To extract cross-section information from the decay energy spectrum, the efficiency and resolution of the measured decay energy were attained using the simulation packages discussed in Section 4.7.

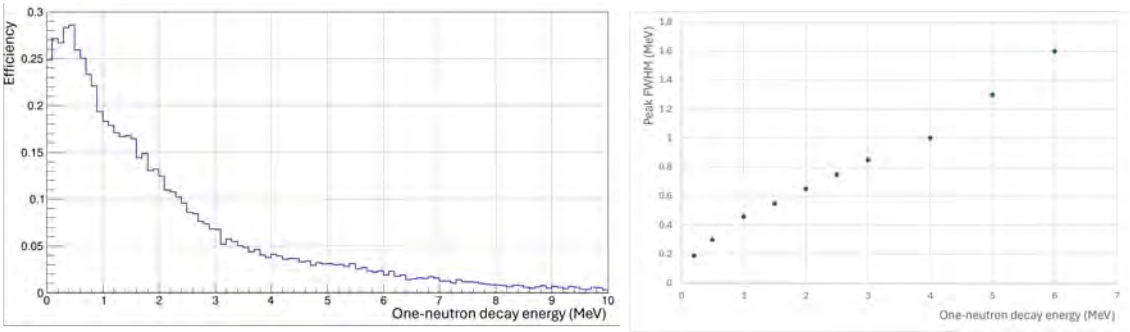

Figure 4.48: Efficiency (left panel) and decay energy resolution (right panel) for reactions in the target as a function of decay energy.

The efficiency was determined by the geometric acceptance and detection efficiency of the telescope and the LISA array. A simulation of a uniform decay energy distribution propagated through the experimental setup was reconstructed to obtain the overall efficiency of the decay energy measurement. The left panel of Figure 4.48 shows the efficiency as a function of decay energy.

The resolution was estimated by simulations of a series of delta-function-like decay energy distributions. The events were fed into the experimental setup, where the resolution effects of each detector were included. The FWHM was extracted from the reconstructed decay energy distributions. The right panel of Figure 4.48 shows the resolution as a function of decay energy.

Chapter 5. Results

5.1 Decay Energy

The final measured decay energy spectrum of ^{13}Be is compared to simulations in the left side of Figure 5.1. The right side of the figure displays the relative velocity (v_{rel}, see Section 4.5.1.2).

The following gates were applied to the experimental data of the decay energy and the relative velocity: (1) ^{14}Be beam gate (Section 4.4.1), (2) neutron gates (Section4.4.2), (3) 2D gates on siPIN1 vs siPIN2 and siPIN4 vs siPIN5 (Section 4.4.3), and (4) 2D kinematic gates (Section 4.7.5).

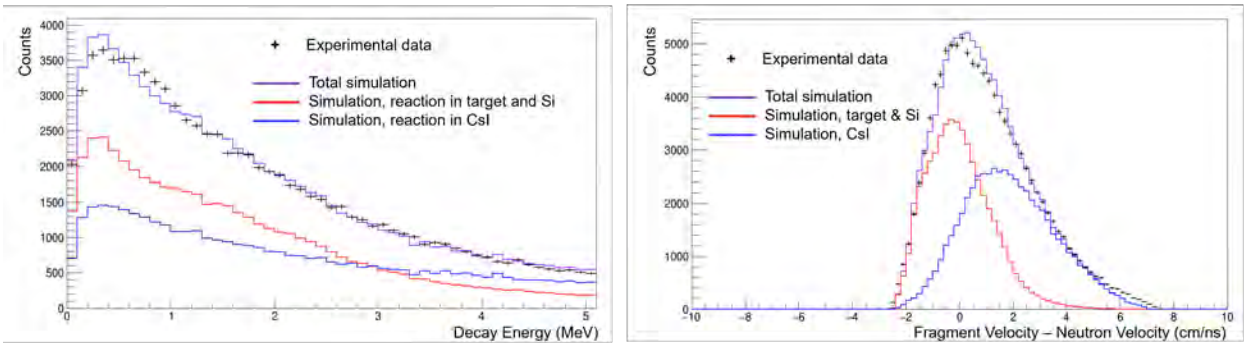

Figure 5.1: Decay energy (left) and relative velocity (right).

As discussed in Subsection 4.7.5 the simulations were combined into two groups: (1) reactions in target or silicon detectors, (2) reactions in the CsI detector and fit simultaneously to the decay energy and the relative velocity data. The relative contributions of the target and the silicon detectors were calculated from the theoretical one-neutron removal cross sections based on the eikonal model (see Section 2.2.1) and are listed in Table 5.1.

The constant coefficients from Equation 4.17 can then be calculated from the cross section and the target thickness ratio:

Table 5.1: Results of eikonal calculations for beryllium and silicon targets of the first three levels in ^{13}Be populated from ^{14}Be. The table lists the spectroscopic factors (C^2S), the single-particle cross sections (σ_{sp}), the theoretical cross sections (σ_{th}), and the ratio of the single-particle cross sections σ_{Si}/σ_{Be}. The cross sections are given in mb.

^{13}Be level	C^2S	σ_{sp_Be}	σ_{th_Be}	σ_{sp_Si}	σ_{th_Si}	σ_{Si}/σ_{Be}
p	0.8276	55.532	52.185	70.729	66.465	1.27
s	0.7167	85.210	70.827	112.951	87.179	1.23
d	1.8307	37.392	79.391	44.060	86.865	1.09

$$C = \sigma_{Si}/\sigma_{Be} \cdot N_{Si}/N_{Be} \tag{5.1}$$

where N_{Be} and N_{Si} correspond to the number of atoms per unit area in the beryllium target and the silicon detectors, respectively. The 486 mg/cm^2 thick beryllium target corresponds to $3.25 \times 10^{22}/cm^2$. The silicon detectors (TLPSD2 and 5 silicon PINs) totaling 2650 μm corresponding to $1.32 \times 10^{22}/cm^2$. Thus the ratio N_{Be}/N_{Si} is 0.41.

The specific coefficients C_1, C_2, and C_3 for the p, s, and d wave contributions are then 0.52, 0.50, and 0.45, respectively. C_4 for the background distribution was set at the average of value of 0.49.

The results of the reactions in the target and silicon detectors, the reactions in the CsI, and the sum is shown in Figure 5.1 by the red, blue, and purple histograms. Details of the fitting algorithm, fitting components, and parameters can be found in 4.7.The decay energy distribution for reactions in the CsI appear distorted due to the incorrect reconstruction of the kinematic parameters.

The relative velocity has some sensitivity to the reactions in the target versus the reaction in the CsI. While the relative velocity of reactions in the target (and the Si detectors) is centered around zero, the apparent fragment velocity for reactions in the CsI is larger than the velocity of the neutrons, as calculated from the beam velocity before reacting in the CsI.

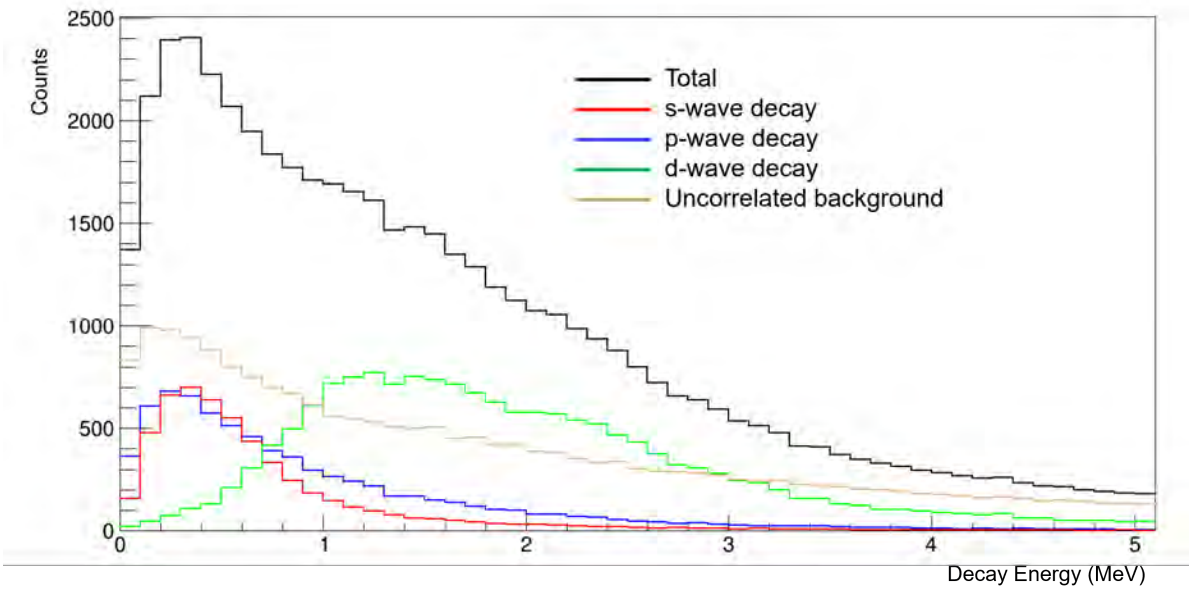

Figure 5.2: Decay energy of reactions in the target and silicon detectors (black). The colored histograms correspond to the four contributions indicated in the figure.

Figure 5.2 shows the fitting components (s-, p-, d-wave decay and uncorrelated background) of the in-flight (target and Si detectors) reactions. The integral number of counts attributed to the p-wave decay in this fit is $5.4(12) \times 10^3$, in which $2.5(5) \times 10^3$ are in the target and $2.9(7) \times 10^3$ in the silicon detectors.

The relative contributions of the p-wave events in the target/silicon detectors and the CsI detector are shown in Figure 5.3. The integrated number of counts with the decay energy less than 1 MeV gate is $5.9(13) \times 10^3$ with the majority of the events coming from the target and the silicon detectors. Correcting for the CAESAR time gate (for the decay lifetime of 331 ns, the gate removing the first 40 ns cuts out about 11% of the total decay events), leaving 5230 events to be used for estimating the expected number of counts of γ rays.

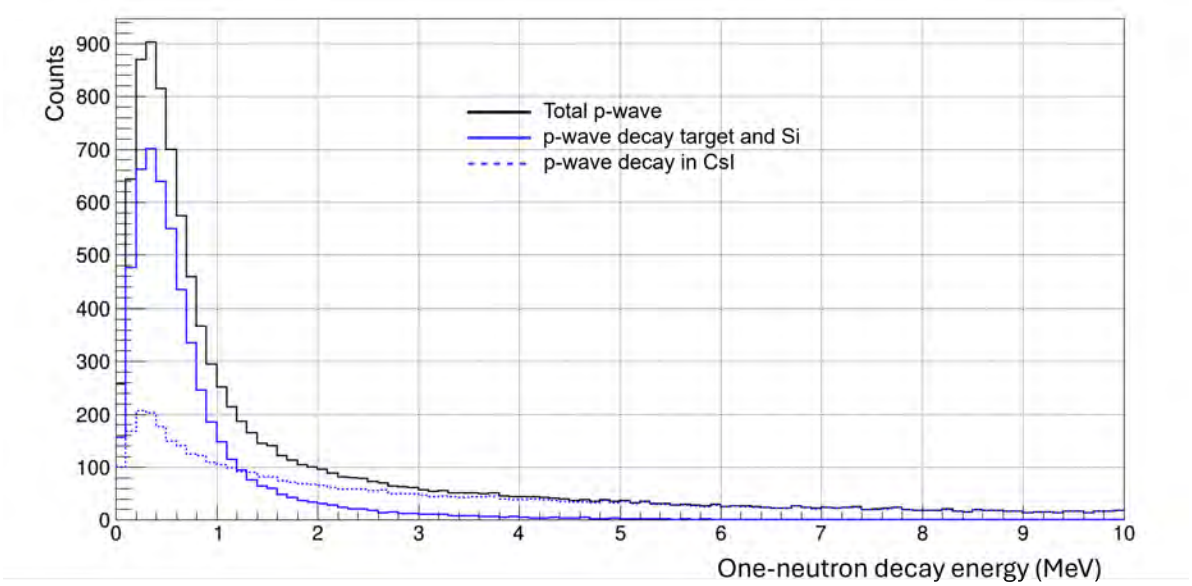

Figure 5.3: p-wave decay in different reaction locations

5.2 CAESAR spectra

The primary purpose of the experiment was to search for delayed 511 keV and 2.1 MeV gamma-rays in the decay of ^{12}Be following the neutron emission of ^{13}Be. This would firmly locate the first $1/2^-$ state of ^{13}Be at 2.7 MeV and not at 0.5 MeV (see Figure 1.4).

The expected counts of γ-ray signatures has to be calculated based on the total measured counts of the p-wave decay, no matter where the reaction occurs. Because for each reaction location, the ^{12}Be fragment will finally stop in the CsI detector and have enough time to emit the delayed γ ray if it is in the isomeric state.

The γ-ray spectrum recorded with CAESAR in coincidence with ^{12}Be fragments and neutrons were analyzed to search for the delayed γ-ray signatures. Two additional gates were applied to enhance delayed p-wave events over the background: (1) a gate limiting decay energies to less than 1 MeV which preferentially selects p-wave emission over the other resonances, and (2) a gate on the CAESAR time (>450 ns, the prompt peak is located at

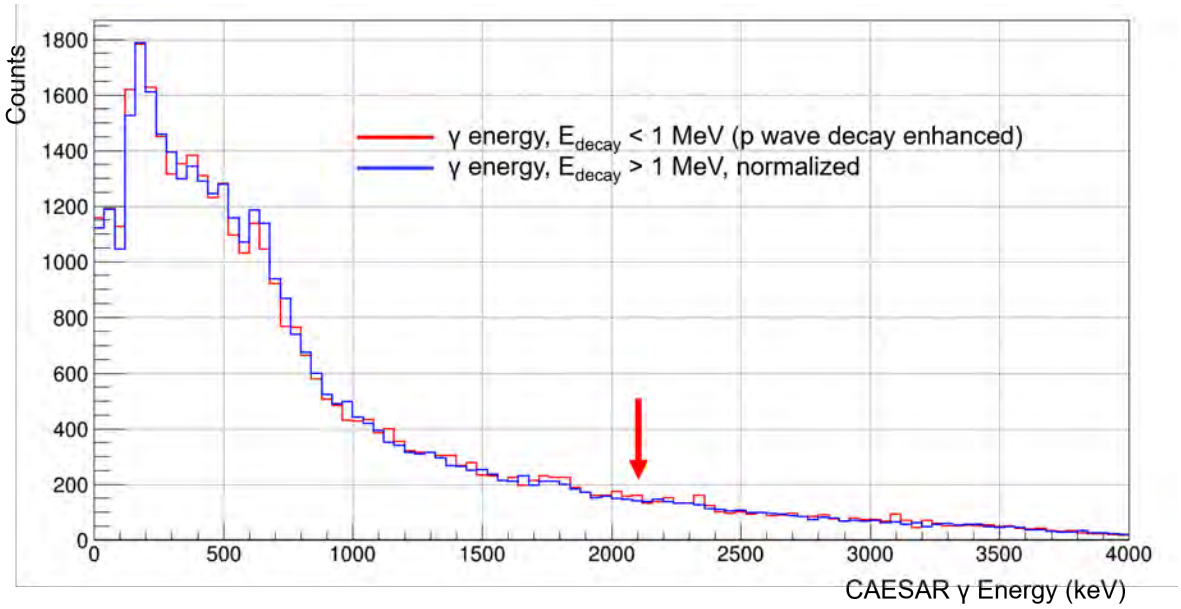

Figure 5.4: CAESAR γ-ray spectra gated on decay energies smaller (red) and larger (blue) than 1 MeV. The red arrow indicates the position of the expected 2.1 MeV peak.

410 ns with a 20 ns FWHM) eliminating prompt γ-rays and,

5.2.1 2.1 MeV γ ray

The effect of the first gate on the 2.1 MeV γ ray is shown in Figure 5.4. It compares the CAESAR γ-ray spectra gated on decay energies $<$ 1 MeV (p-wave decay enhanced) and $>$ 1 MeV in red and blue, respectively. The $>$ 1 MeV histogram serves as background and is normalized to match the integral with the other histogram. There is no indication of any additional events above background in the region of the expected 2.1 MeV peak (indicated by the red arrow).

Figure 5.5 shows the same comparison but with the additional CAESAR time gate larger (red points) and smaller (blue histogram) than 450 ns. The figure zooms in on energies between 1 and 3 MeV. Again, there is no evidence for a delayed γ-ray peak around 2.1 MeV as indicated by the red arrow.

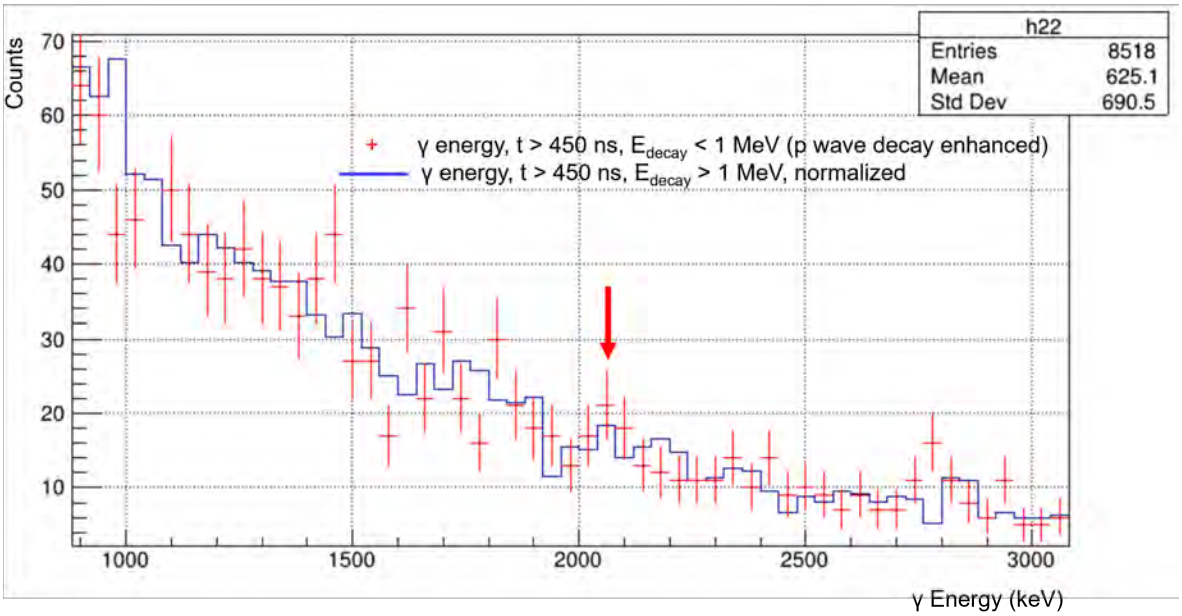

Figure 5.5: CAESAR γ-ray spectra gated on times larger (red points) and smaller (blue histogram) than 450 ns in addition to the decay energy gates from Figure 5.4. The red arrow indicates the position of the expected 2.1 MeV peak.

From the number of counts of the p-wave in the decay energy spectrum it is possible to calculate the number of counts expected for the 2.1 MeV peak assuming that it proceeds through the isomeric state in ^{12}Be.

As discussed in Section 1.5, the branching ratios for the 2107 keV γ-ray decay is 17.7%. The efficiency at 2.1 MeV is 9.6% according to the CAESAR simulation in Section 4.3.3. Thus, the expected counts in the 2.1 MeV peak can be calculated as

$$N_{2107,\text{expected}} = 5.23 \times 10^3 \cdot 17.7\% \cdot 9.6\% = 89(19). \tag{5.2}$$

Figure 5.6 shows simulations with (solid blue) and without (dashed blue) the possible 2.1 MeV peak compared to the data (red). The experimental data do not show a clear peak at 2.1 MeV, and approximately coincides with 15% of the expected counts.

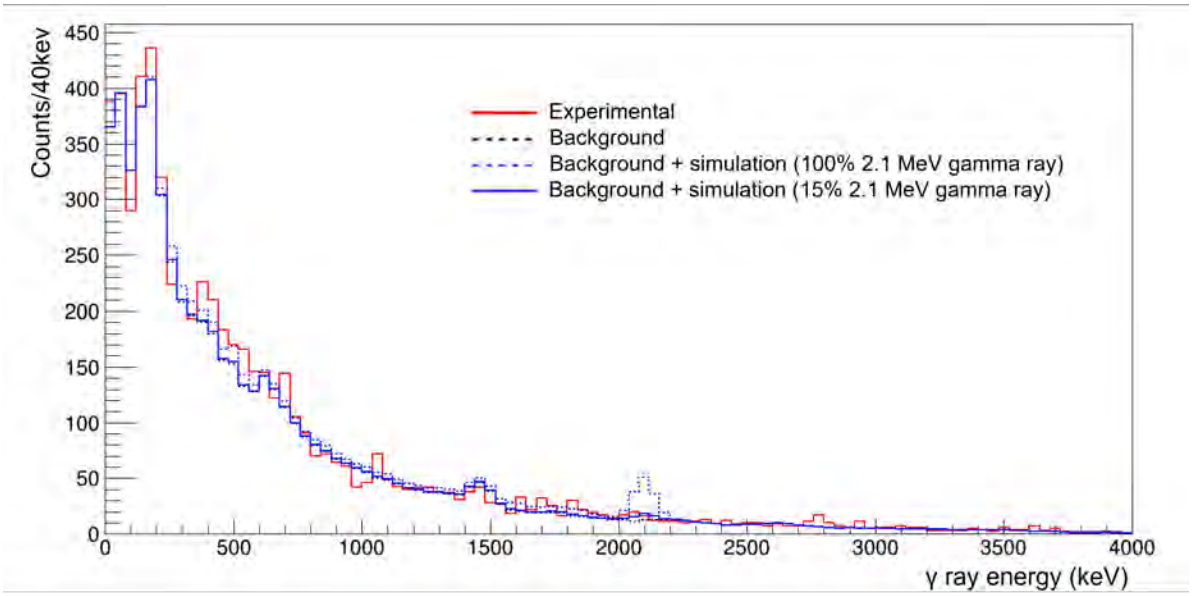

Figure 5.6: CAESAR γ-ray spectrum comparing the data (red) with simulation results with (solid blue) and without (dashed blue) a 2.1 MeV state.

5.2.2 511 keV γ rays

The second possible signature for the population of the isomeric state in ^{12}Be is the direct decay of this 0^+ state to the ground state via internal pair transition and the emission of two 511 γ-rays.

As can be seen Figures 5.4 and 5.6, there is no clear evidence for a peak around 500 keV above a relatively large background.

The two 511 keV γ-rays of the internal pair transition are emitted back-to-back so that such a coincidence condition applied might expose this decay.

The number of expected events can again be calculated from the number of p-wave events in the decay energy spectrum. According to the CAESAR simulation in Section 4.3.3, the efficiency to detect both 511 keV γ rays of the pair emission is 3.9%. As discussed in Section 1.5, the branching ratios for the internal pair transition is 82.3% so that the expected counts

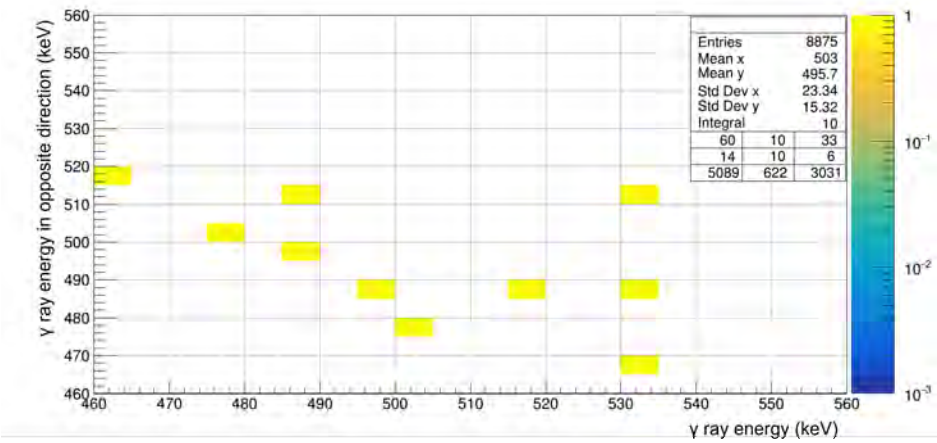

Figure 5.7: Energy correlations of two opposite CAESAR detectors with gates applied as described in the text.

of the gamma ray signatures can be calculated as

$$N_{511,\text{expected}} = 5.23 \times 10^3 \cdot 82.3\% \cdot 3.9\% = 168(36), \tag{5.3}$$

The analysis to search for back-to-back emission of two 511 keV γ-rays was presented in Section 4.6.2. Figure 5.2.2 shows the CAESAR 2-D correlation plot of all possible pairs of opposite detectors, with decay energy and CAESAR time gates. The events with both opposite detectors firing and the gamma ray energy falling in the range of 460 keV to 560 keV are recorded in the plot. 8 counts were found. (There are 2 pairs of events that are symmetrical to the $y = x$ line, so they are actually 2 events that are counted twice instead of 4 individual events.)

The coincidence condition was somewhat relaxed by also including the eight neighbors of the opposite detectors as demonstrated in Figure 5.8. The condition for the "90-degree" background events was similarly relaxed. Table 5.2 lists the number of events for the opposite and the 90-degree events for the nine different coincidence conditions.

The difference between the opposite and the 90-degrees events (including neighbors)

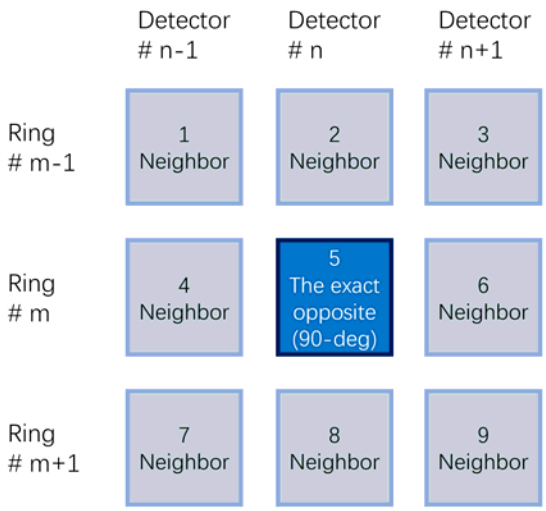

Figure 5.8: Definition of the relaxed coincidence condition including the neighbors of the opposite detectors.

Table 5.2: Number of counts for opposite and 90-degree events for the nine coincidence conditions defined in Figure 5.8

Correlation conditions	1	2	3	4	5	6	7	8	9	total
Counts (opposite)	1	2	0	3	8	3	1	3	3	24
Counts (90-degree)	1	1	0	1	1	2	5	2	3	16

correspond to the number of real 511 kev γ-ray pairs observed above background, which is 8(6) counts. This number has to be compared to the 168(36) expected events from the decay energy spectrum.

Even if all observed opposite events would correspond to real pairs, the number would still be a factor of 20 smaller than the expected events. Considering the uncertainty of the expected counts and the measured counts, it gives an upper limit of 13%.

This analysis is consistent with the non-observation of delayed 2.1 MeV γ-rays and confirms that the p-wave is not located at 2.7 MeV but at 0.5 MeV.

5.3 Cross sections

The cross-section can be expressed as

$$\sigma = \frac{N_{react}}{N_{incident} \cdot \eta \cdot N_{target}}, \tag{5.4}$$

where N_{react} is the number of observed events, $N_{incident}$ the number of incident beam particles, η the efficiency, and N_{target} the number of atoms per unit area in the target. The value for N_{target} ($3.25 \times 10^{22} cm^{-2}$) was already quoted in Section 5.1 and $N_{incident}$ was 1.07×10^{7}. As shown in Section 4.8 the efficiency depends in the decay energy, so N_{react}/η was calculated as $\Sigma N_{react}(E_{decay})/\eta(E_{decay})$. Figure 5.9 shows the decay energy spectra for the corrected for the efficiency for reactions in the beryllium target for the s-, p-, d-wave resonances in red, blue, and green, respectively.

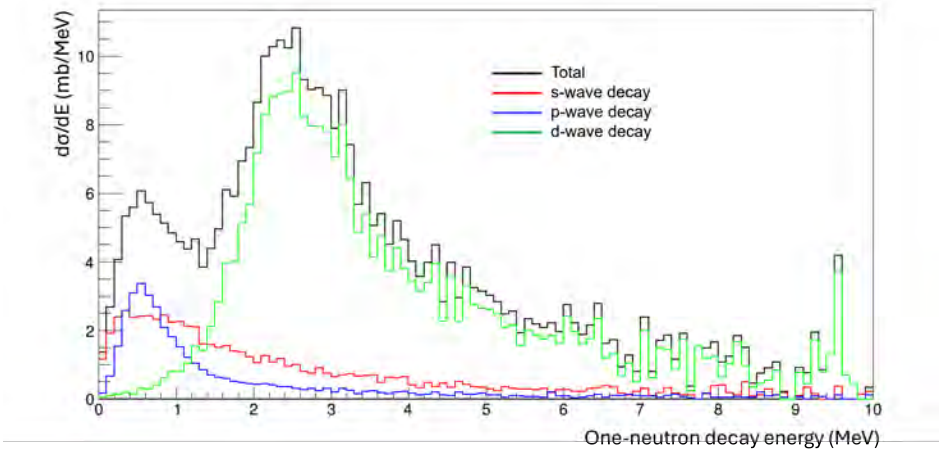

Figure 5.9: Decay energy spectra corrected for the efficiency.

The resulting experimental cross sections for the p, s, and d wave resonances are 39(7) mb, 69(15) mb, and 262(10) mb, respectively.

Theoretical cross sections can be calculated from the eikonal reaction model based on

the shell model spectroscopic factors (Section 2.2.1). The spectroscopic factors for the one-neutron removal from ^{14}Be populating the lowest three states of interest in ^{13}Be (p, s, and d) are listed in Table 5.1.

Table 5.3 compares the theoretical with the experimental cross sections. While the cross-sections for the p- and s-wave are well reproduced, the experimental values for the d-wave are significantly larger.

Table 5.3: Angular momenta, energies E, widths Γ of the simulated resonances, and the experimental (σ_{exp}) and theoretical (σ_{th}) cross sections.

Angular momentum	Energy E (MeV)	Width Γ (MeV)	σ_{exp} (mb)	σ_{th} (mb)
l=0 (s)	0.81	2.1	69(15)	71
l=1 (p)	0.45	0.45	39(7)	52
l=2 (d)	2.0	2.0	262(10)	79

This can also be seen in Figure 5.10 where the efficiency corrected decay energy spectra are shown for the experimental data (solid lines) and the theoretical calculations (dashed lines).

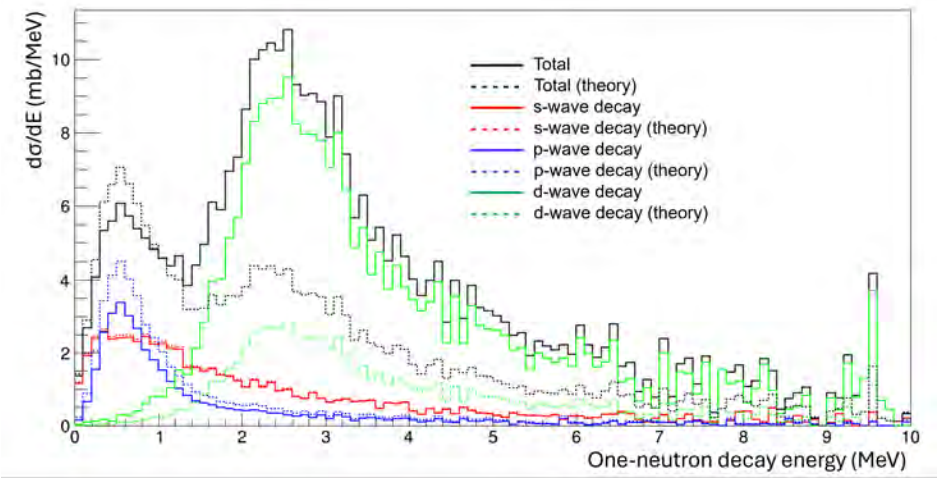

Figure 5.10: Efficiency corrected decay energy spectra for the experimental data and theoretical calculations.

Chapter 6. Conclusion

The decay energy spectrum of the neutron-unbound ^{13}Be was reconstructed using the invariant mass method by detecting neutrons in coincidence with ^{12}Be fragments. The neutrons were detected with 96 scintillation detectors of the LISA array and the fragments were stopped and identified with a newly constructed charged particle telescope. In contrast to previous MoNA-LISA experiments the fragments were directly detected at 0° and not deflected by the Sweeper magnet.

The charged particle telescope located 140 cm behind the target was surrounded by the CAESium-iodide scintillator ARray CAESAR to detect delayed γ-rays. The two decay branches of the isomeric second 0_2^+ state in ^{12}Be were investigated: (1) the $0_2^+ \rightarrow 2^+ \rightarrow 0_1^+ \gamma$-ray cascade via the 2107 keV γ ray from the 2^+ state and (2) the $0_2^+ \rightarrow 0_1^+$ internal transition via the two annihilation 511 keV γ rays.

No evidence for either branch was observed above the background. An upper limit of 10% contribution of the p-wave decay via the ^{12}Be isomeric state was given by the coincidence of the two 511 keV γ rays.

The decay energy and the delayed γ-ray spectra were compared to detailed simulations based on shell model calculations including the population of the $1/2^+$-, $1/2^-$, and $5/2^+$-states in ^{13}Be. The simulations also included the acceptances and efficiencies of the detectors. If the $1/2^-$-state populated the isomeric 2^+ state in ^{12}Be, the expected number of γ-ray events for either decay branch exceeded the background level by a factor of seven. Thus, the results of the previous experiments which place the $1/2^-$-state at about 450 keV above the ground state of ^{12}Be are confirmed.

The proposed decay branch of a second $5/2^+$ state in ^{13}Be to the isomeric 0_2^+ in ^{12}Be

cannot be ruled out by the present experiment. This state is not expected to be populated by neutron removal from ^{14}Be as the spectroscopic factor is only about 1% of the spectroscopic factor for the $1/2^-$ state which is below the sensitivity level for detecting delayed γ rays with the present setup.

BIBLIOGRAPHY

[1] National Nuclear Data Center, https://www.nndc.bnl.gov.

[2] B. A. Brown, *Lecture Notes in Nuclear Structure Physics*. Michigan State University, 2021.

[3] D. J. Morrissey, B. M. Sherrill, M. Steiner, A. Stolz, and I. Wiedenhoever, "Commissioning the A1900 projectile fragment separator," *Nuclear Instruments and Methods in Physics Research Section B*, vol. 204, pp. 90–96, 2003.

[4] H. Becquerel, "Sur les radiations émises par phosphorescence," *Comptes rendus de 1'Academie des Sciences, Paris*, vol. 122, pp. 420–421, 1896.

[5] H. Becquerel, "Sur les radiations invisible emises par les corps phosphorescents," *Comptes rendus de 1'Academie des Sciences, Paris*, vol. 122, pp. 501–503, 1896.

[6] A. H. Becquerel, "Sur quelques propriétés nouvelles des radiations invisibles émises par divers corps phosphorescents," *Comptes rendus de 1'Academie des Sciences, Paris*, vol. 122, p. 559, 1896.

[7] A. Becquerel, "Sur les radiations invisibles émises par les sels d'uranium," *Comptes rendus de 1'Academie des Sciences, Paris*, vol. 122, pp. 689–694, 1896.

[8] A. H. Becquerel, "Sur les propriétés différentes des radiations invisibles émises par les sels d'uranium, et du rayonnement de la paroi anticathodique d'un tube de crookes," *Comptes rendus de 1'Academie des Sciences, Paris*, vol. 122, p. 762, 1896.

[9] H. Becquerel, "Émission de radiation nouvelles par l'uranium métallique," *Comptes rendus de 1'Academie des Sciences, Paris*, vol. 122, p. 1086, 1986.

[10] H. Becquerel, *Sur diverses propriétés des rayons uraniques*. Gauthier-Villars, 1896.

[11] E. Rutherford, "LXXIX. the scattering of α and β particles by matter and the structure of the atom," *The London, Edinburgh, and Dublin Philosophical Magazine and Journal of Science*, vol. 21, no. 125, pp. 669–688, 1911.

[12] J. Chadwick, "The existence of a neutron," *Proceedings of the Royal Society of London. Series A*, vol. 136, no. 830, pp. 692–708, 1932.

[13] E. O. Lawrence and M. S. Livingston, "The production of high speed light ions without the use of high voltages," *Physical Review*, vol. 40, no. 1, p. 19, 1932.

[14] J. D. Cockcroft and E. T. Walton, "Artificial production of fast protons," *Nature*, vol. 129, no. 3250, pp. 242–242, 1932.

[15] M. Thoennessen, *The Discovery of Isotopes: A Complete Compilation*. Springer, 2016.

[16] J. M. Lattimer and M. Prakash, "The physics of neutron stars," *Science*, vol. 304, no. 5670, pp. 536–542, 2004.

[17] M. Thoennessen, "Reaching the limits of nuclear stability," *Reports on Progress in Physics*, vol. 67, no. 7, p. 1187, 2004.

[18] S. Beane, W. Detmold, K. Orginos, and M. Savage, "Nuclear physics from lattice QCD," *Progress in Particle and Nuclear Physics*, vol. 66, no. 1, pp. 1–40, 2011.

[19] S. A. Giuliani, Z. Matheson, W. Nazarewicz, E. Olsen, P.-G. Reinhard, J. Sadhukhan, B. Schuetrumpf, N. Schunck, and P. Schwerdtfeger, "Colloquium: Superheavy elements: Oganesson and beyond," *Reviews of Modern Physics*, vol. 91, no. 1, p. 011001, 2019.

[20] A. Afanasjev, S. Agbemava, and A. Gyawali, "Hyperheavy nuclei: Existence and stability," *Physics Letters B*, vol. 782, pp. 533–540, 2018.

[21] M. G. Mayer, "On closed shells in nuclei," *Physical Review*, vol. 74, no. 3, p. 235, 1948.

[22] M. G. Mayer, "On closed shells in nuclei. II," *Physical Review*, vol. 75, no. 12, p. 1969, 1949.

[23] M. G. Mayer, "Nuclear configurations in the spin-orbit coupling model. i. empirical evidence," *Physical Review*, vol. 78, no. 1, p. 16, 1950.

[24] M. G. Mayer, "Nuclear configurations in the spin-orbit coupling model. ii. theoretical considerations," *Physical Review*, vol. 78, no. 1, p. 22, 1950.

[25] O. Haxel, J. H. D. Jensen, and H. E. Suess, "On the "magic numbers" in nuclear structure," *Physical Review*, vol. 75, no. 11, p. 1766, 1949.

[26] K. Jones, J. Kovoor, and R. Kanungo, "Status of experimental knowledge on the unbound nucleus ^{13}Be," *Frontiers in Physics*, vol. 11, p. 1242668, 2023.

[27] D. Tilley, J. Kelley, J. Godwin, D. Millener, J. Purcell, C. Sheu, and H. Weller, "Energy levels of light nuclei A=8,9,10," *Nuclear Physics A*, vol. 745, no. 3, pp. 155–362, 2004.

[28] W. Von Oertzen, "Two-center molecular states in ^{9}B, ^{9}Be, ^{10}Be, and ^{10}B," *Zeitschrift für Physik A*, vol. 354, pp. 37–43, 1996.

[29] W. Von Oertzen, "Dimers based on the α+α potential and chain states of carbon isotopes," *Zeitschrift für Physik A*, vol. 357, pp. 355–365, 1997.

[30] M. Seya, M. Kohno, and S. Nagata, "Nuclear binding mechanism and structure of neutron-rich Be and B isotopes by molecular-orbital model," *Progress of Theoretical Physics*, vol. 65, no. 1, pp. 204–223, 1981.

[31] Y. Parfenova and C. Leclercq-Willain, "Hyperfine anomaly in be isotopes in the cluster model and the neutron spatial distribution," *Physical Review C*, vol. 72, no. 2, p. 024312, 2005.

[32] W. Nörtershäuser, D. Tiedemann, M. Žáková, Z. Andjelkovic, K. Blaum, M. L. Bissell, R. Cazan, G. Drake, C. Geppert, M. Kowalska, *et al.*, "Nuclear charge radii of ^{7,9,10}Be and the one-neutron halo nucleus ^{11}Be," *Physical Review Letters*, vol. 102, no. 6, p. 062503, 2009.

[33] A. Krieger, K. Blaum, M. L. Bissell, N. Frömmgen, C. Geppert, M. Hammen, K. Kreim, M. Kowalska, J. Krämer, T. Neff, *et al.*, "Nuclear charge radius of ^{12}Be," *Physical Review Letters*, vol. 108, no. 14, p. 142501, 2012.

[34] S. Fortier, S. Pita, J. Winfield, W. Catford, N. Orr, J. Van de Wiele, Y. Blumenfeld, R. Chapman, S. Chappell, N. Clarke, N. Curtis, M. Freer, S. Gals, K. Jones, H. Langevin-Joliot, H. Laurent, I. Lhenry, J. Maison, P. Roussel-Chomaz, M. Shawcross, M. Smith, K. Spohr, T. Suomijarvi, and A. de Vismes, "Core excitation in ^{11}Be$_{gs}$ via the p(^{11}Be,^{10}Be)d reaction," *Physics Letters B*, vol. 461, no. 1, pp. 22–27, 1999.

[35] A. Navin, D. Anthony, T. Aumann, T. Baumann, D. Bazin, Y. Blumenfeld, B. Brown, T. Glasmacher, P. Hansen, R. Ibbotson, *et al.*, "Direct evidence for the breakdown of the N=8 shell closure in ^{12}Be," *Physical Review Letters*, vol. 85, no. 2, p. 266, 2000.

[36] G. Gori, F. Barranco, E. Vigezzi, and R. A. Broglia, "Parity inversion and breakdown of shell closure in Be isotopes," *Physical Review C*, vol. 69, p. 041302, Apr 2004.

[37] P. Descouvemont, "Halo structure of ^{14}Be in a microscopic ^{12}Be+n+n cluster model," *Physical Review C*, vol. 52, no. 2, p. 704, 1995.

[38] I. Thompson and M. Zhukov, "Structure and reactions of the ^{12,14}Be nuclei," *Physical Review C*, vol. 53, no. 2, p. 708, 1996.

[39] M. Labiche, F. Marqués, O. Sorlin, and N. V. Mau, "Structure of ^{13}Be and ^{14}Be," *Physical Review C*, vol. 60, no. 2, p. 027303, 1999.

[40] A. Spyrou, J. Smith, T. Baumann, B. Brown, J. Brown, G. Christian, P. A. DeYoung, N. Frank, S. Mosby, W. Peters, *et al.*, "Search for the ^{15}Be ground state," *Physical Review C*, vol. 84, no. 4, p. 044309, 2011.

[41] A. Spyrou, Z. Kohley, T. Baumann, D. Bazin, B. Brown, G. Christian, P. A. DeYoung, J. Finck, N. Frank, E. Lunderberg, *et al.*, "First observation of ground state dineutron decay: ^{16}Be," *Physical Review Letters*, vol. 108, no. 10, p. 102501, 2012.

[42] S. Shimoura, S. Ota, K. Demichi, N. Aoi, H. Baba, Z. Elekes, T. Fukuchi, T. Gomi, K. Hasegawa, E. Ideguchi, M. Ishihara, N. Iwasa, H. Iwasaki, S. Kanno, S. Kubono, K. Kurita, M. Kurokawa, Y. Matsuyama, S. Michimasa, K. Miller, T. Minemura, T. Motobayashi, T. Murakami, M. Notani, A. Odahara, A. Saito, H. Sakurai, E. Takeshita, S. Takeuchi, M. Tamaki, T. Teranishi, K. Yamada, Y. Yanagisawa, and I. Hamamoto, "Lifetime of the isomeric 0_2^+ state in ^{12}Be," *Physics Letters B*, vol. 654, no. 3, pp. 87–91, 2007.

[43] J. G. Johansen, V. Bildstein, M. J. G. Borge, M. Cubero, J. Diriken, J. Elseviers, L. M. Fraile, H. O. U. Fynbo, L. P. Gaffney, R. Gernhäuser, B. Jonson, G. T. Koldste, J. Konki, T. Kröll, R. Krücken, D. Mücher, T. Nilsson, K. Nowak, J. Pakarinen, V. Pesudo, R. Raabe, K. Riisager, M. Seidlitz, O. Tengblad, H. Törnqvist, D. Voulot, N. Warr, F. Wenander, K. Wimmer, and H. De Witte, "Experimental study of bound states in ^{12}Be through low-energy ^{11}Be(d,p)-transfer reactions," *Physical Review C*, vol. 88, p. 044619, Oct 2013.

[44] Y. Kondo, T. Nakamura, Y. Satou, T. Matsumoto, N. Aoi, N. Endo, N. Fukuda, T. Gomi, Y. Hashimoto, M. Ishihara, *et al.*, "Low-lying intruder state of the unbound nucleus ^{13}Be," *Physics Letters B*, vol. 690, no. 3, pp. 245–249, 2010.

[45] H. T. Fortune and R. Sherr, "Neutron decays of ^{13}Be* to the 0_2^+ state of ^{12}Be," *Physical Review C*, vol. 82, p. 064302, Dec 2010.

[46] The MoNA Collaboration. `http://monacollaboration.org`.

[47] The National Superconducting Cyclotron Laboratory. `https://nscl.msu.edu`.

[48] B. Luther, T. Baumann, M. Thoennessen, J. Brown, P. DeYoung, J. Finck, J. Hinnefeld, R. Howes, K. Kemper, P. Pancella, G. Peaslee, W. Rogers, and S. Tabor, "MoNA-The Modular Neutron Array," *Nuclear Instruments and Methods in Physics Research Section A: Accelerators, Spectrometers, Detectors and Associated Equipment*, vol. 505, no. 1, pp. 33–35, 2003. Proceedings of the 10^{th} Symposium on Radiation Measurements and Applications.

[49] D. Weisshaar, A. Gade, T. Glasmacher, G. Grinyer, D. Bazin, P. Adrich, T. Baugher, J. Cook, C. Diget, S. McDaniel, A. Ratkiewicz, K. Siwek, and K. Walsh, "CAESAR-A high-efficiency CsI(Na) scintillator array for in-beam γray spectroscopy with fast rare-isotope beams," *Nuclear Instruments and Methods in Physics Research Section A: Accelerators, Spectrometers, Detectors and Associated Equipment*, vol. 624, no. 3, pp. 615–623, 2010.

[50] D. Aleksandrov, E. Ganza, and Y. A. Glukhov, "Observation of the isotope ^{13}Be in the reaction ^{14}C(^{7}Li,^{8}B)," *Soviet Journal of Nuclear Physics*, vol. 37, no. 3, pp. 474–475, 1983.

[51] A. Ostrowski, H. Bohlen, A. Demyanova, B. Gebauer, R. Kalpakchieva, C. Langner, H. Lenske, M. von Lucke-Petsch, W. von Oertzen, A. Ogloblin, *et al.*, "Mass spectroscopy of ^{13}Be," *Zeitschrift für Physik A*, vol. 343, pp. 489–490, 1992.

[52] A. Korsheninnikov, E. Y. Nikolskii, T. Kobayashi, D. Aleksandrov, M. Fujimaki, H. Kumagai, A. Ogloblin, A. Ozawa, I. Tanihata, Y. Watanabe, *et al.*, "Spectroscopy of ^{12}Be and ^{13}Be using a ^{12}Be radioactive beam," *Physics Letters B*, vol. 343, no. 1-4, pp. 53–58, 1995.

[53] W. v. Oertzen, H. Bohlen, B. Gebauer, M. v. Lucke-Petsch, A. Ostrowski, C. Seyfert, T. Stolla, M. Wilpert, T. Wilpert, D. Alexandrov, *et al.*, "Nuclear structure studies of very neutron-rich isotopes of $^{7-10}$He, $^{9-11}$Li and $^{12-14}$Be via two-body reactions," *Nuclear Physics. A*, vol. 588, no. 1, pp. 129C–134C, 1995.

[54] A. Belozyorov, R. Kalpakchieva, Y. E. Penionzhkevich, Z. Dlouhỳ, S. Piskor, J. Vincour, H. Bohlen, M. von Lucke-Petsch, A. Ostrowski, D. Alexandrov, *et al.*, "Spectroscopy of ^{13}Be," *Nuclear Physics A*, vol. 636, no. 4, pp. 419–426, 1998.

[55] M. Thoennessen, S. Yokoyama, and P. Hansen, "First evidence for low lying s-wave strength in ^{13}Be," *Physical Review C*, vol. 63, no. 1, p. 014308, 2000.

[56] J. Lecouey, "Experimental studies of unbound neutron-rich nuclei," *Few-Body Systems*, vol. 34, no. 1, pp. 21–26, 2004.

[57] H. Simon, M. Meister, T. Aumann, M. Borge, L. Chulkov, U. D. Pramanik, T. W. Elze, H. Emling, C. Forssén, H. Geissel, *et al.*, "Systematic investigation of the drip-line nuclei ^{11}Li and ^{14}Be and their unbound subsystems ^{10}Li and ^{13}Be," *Nuclear Physics A*, vol. 791, no. 3-4, pp. 267–302, 2007.

[58] Y. Aksyutina, T. Aumann, K. Boretzky, M. Borge, C. Caesar, A. Chatillon, L. Chulkov, D. Cortina-Gil, U. Datta Pramanik, H. Emling, *et al.*, "Structure of the unbound nucleus ^{13}Be: One-neutron knockout reaction data from ^{14}Be analyzed in a holistic approach," *Physical Review C*, vol. 87, no. 6, p. 064316, 2013.

[59] G. Randisi, A. Leprince, H. Al Falou, N. Orr, F. M. Marqués, N. Achouri, J.-C. Angélique, N. Ashwood, B. Bastin, T. Bloxham, *et al.*, "Structure of ^{13}Be probed via secondary-beam reactions," *Physical Review C*, vol. 89, no. 3, p. 034320, 2014.

[60] B. Marks, P. A. DeYoung, J. Smith, T. Baumann, J. Brown, N. Frank, J. Hinnefeld, M. Hoffman, M. Jones, Z. Kohley, *et al.*, "Population of ^{13}Be in a nucleon exchange reaction," *Physical Review C*, vol. 92, no. 5, p. 054320, 2015.

[61] G. Ribeiro, E. Nácher, O. Tengblad, P. Díaz Fernández, Y. Aksyutina, H. Alvarez-Pol, L. Atar, T. Aumann, V. Avdeichikov, S. Beceiro-Novo, *et al.*, "Structure of ^{13}Be studied in proton knockout from ^{14}B," *Physical Review C*, vol. 98, no. 2, p. 024603, 2018.

[62] A. Corsi, Y. Kubota, J. Casal, M. Gómez-Ramos, A. Moro, G. Authelet, H. Baba, C. Caesar, D. Calvet, A. Delbart, *et al.*, "Structure of ^{13}Be probed via quasi-free scattering," *Physics Letters B*, vol. 797, p. 134843, 2019.

[63] J. Kovoor, K. Jones, J. Hooker, M. Vostinar, R. Kanungo, S. Pain, M. Alcorta, J. Allen, C. Andreoiu, L. Atar, *et al.*, "Structure studies of ^{13}Be from the ^{12}Be(d,p) reaction in inverse kinematics on a solid deuteron target," *Physical Review C*, vol. 108, no. 3, p. 034601, 2023.

[64] C. Hunt, S. Ahn, J. Bishop, E. Koshchiy, E. Aboud, M. Alcorta, A. Bosh, K. Hahn, S. Han, C. Parker, *et al.*, "Spectroscopy of ^{13}Be through isobaric analog states in ^{13}B," *Physical Review C*, vol. 108, no. 5, p. L051606, 2023.

[65] B. Brown and W. Rae, "The shell-model code nushellx@MSU," *Nuclear Data Sheets*, vol. 120, pp. 115–118, 2014.

[66] Y. Utsuno and S. Chiba, "Multiparticle-multihole states around ^{16}O and correlation-energy effect on the shell gap," *Physical Review C*, vol. 83, no. 2, p. 021301, 2011.

[67] R. Meharchand, R. G. T. Zegers, B. A. Brown, S. M. Austin, T. Baugher, D. Bazin, J. Deaven, A. Gade, G. F. Grinyer, C. J. Guess, M. E. Howard, H. Iwasaki, S. McDaniel, K. Meierbachtol, G. Perdikakis, J. Pereira, A. M. Prinke, A. Ratkiewicz, A. Signoracci, S. Stroberg, L. Valdez, P. Voss, K. A. Walsh, D. Weisshaar, and R. Winkler, "Probing configuration mixing in ^{12}Be with gamow-teller transition strengths," *Physical Review Letters*, vol. 108, p. 122501, Mar 2012.

[68] P. Hansen and J. Tostevin, "Direct reactions with exotic nuclei," *Annual Review of Nuclear and Particle Science*, vol. 53, no. 1, pp. 219–261, 2003.

[69] J. Tostevin, "Single-nucleon knockout reactions at fragmentation beam energies," *Nuclear Physics A*, vol. 682, no. 1-4, pp. 320c–331c, 2001.

[70] J. Tostevin and A. Gade, "Systematics of intermediate-energy single-nucleon removal cross sections," *Physical Review C*, vol. 90, no. 5, p. 057602, 2014.

[71] A. Dieperink and T. de Forest Jr, "Center-of-mass effects in single-nucleon knock-out reactions," *Physical Review C*, vol. 10, no. 2, p. 543, 1974.

[72] A. Gade, P. Adrich, D. Bazin, M. Bowen, B. Brown, C. Campbell, J. Cook, T. Glasmacher, P. Hansen, K. Hosier, *et al.*, "Reduction of spectroscopic strength: Weakly-

bound and strongly-bound single-particle states studied using one-nucleon knockout reactions," *Physical Review C*, vol. 77, no. 4, p. 044306, 2008.

[73] G. Breit and E. Wigner, "Capture of slow neutrons," *Physical Review*, vol. 49, no. 7, p. 519, 1936.

[74] A. Lane and R. Thomas, "R-matrix theory of nuclear reactions," *Reviews of Modern Physics*, vol. 30, no. 2, p. 257, 1958.

[75] B. Luther, T. Baumann, M. Thoennessen, J. Brown, P. DeYoung, J. Finck, J. Hinnefeld, R. Howes, K. Kemper, P. Pancella, *et al.*, "MoNA−the Modular Neutron Array," *Nuclear Instruments and Methods in Physics Research Section A*, vol. 505, no. 1-2, pp. 33–35, 2003.

[76] NSCL DAQ Software Documentation. `https://docs.frib.msu.edu/daq/newsite/nscldaq-11.0/index.html`.

[77] SpecTcl Documentation. `https://docs.frib.msu.edu/daq/spectcl/index.htm`.

[78] O. Tarasov and D. Bazin, "Lise++: Radioactive beam production with in-flight separators," *Nuclear Instruments and Methods in Physics Research Section B: Beam Interactions with Materials and Atoms*, vol. 266, no. 19, pp. 4657–4664, 2008. Proceedings of the XVth International Conference on Electromagnetic Isotope Separators and Techniques Related to their Applications.

[79] F. S. Goulding and B. G. Harvey, "Identification of nuclear particles," *Lawrence Berkeley National Laboratory*, 1974. LBNL Report #: LBL-2952. Retrieved from https://escholarship.org/uc/item/334377kw.

[80] M. Livingston and H. Bethe, "The range-energy relation," *Rev. Mod. Phys*, vol. 9, pp. 261–276, 1937.